

GUINIER-PRESTON ZONE EVOLUTION IN 7075 ALUMINUM

by

JOHN THOMAS HEALEY

A DISSERTATION PRESENTED TO THE GRADUATE COUNCIL OF  
THE UNIVERSITY OF FLORIDA IN PARTIAL FULFILLMENT OF THE  
REQUIREMENTS FOR THE DEGREE OF DOCTOR OF PHILOSOPHY

UNIVERSITY OF FLORIDA

1976



UNIVERSITY OF FLORIDA



3 1262 08552 3263

To Connie

## ACKNOWLEDGMENTS

The author wishes to thank his chairman, Professor Robert W. Gould, who devoted much of his time, and gave both many helpful suggestions and encouragement during the course of this study. He is also indebted to other members of his committee, Professors John J. Hren, Robert E. Reed-Hill and Frank Blanchard, as well as Professor Rolf E. Hummel, whose valuable assistance and suggestions have aided in the completion of this work.

The author is grateful to the National Science Foundation for the financial aid of NSF grant # GH 31817.

The author also wishes to thank John M. Horn, William Schulz, John Garrett and Vicki Turner for their assistance provided during this endeavour.

## TABLE OF CONTENTS

	<u>PAGE</u>
ACKNOWLEDGMENTS.....	iii
LIST OF TABLES.....	vi
LIST OF FIGURES.....	vii
ABSTRACT.....	xi
INTRODUCTION.....	1
CHAPTER	
I        REVIEW OF PREVIOUS WORK.....	4
II       THEORY OF SMALL ANGLE X-RAY SCATTERING.....	23
III      EXPERIMENTAL EQUIPMENT AND PROCEDURES.....	48
The Alloy.....	48
Small Angle and Tensile Test Sample Preparation.....	48
Resistometry Sample Preparation.....	49
Solutionizing and Aging.....	50
Wide Angle Diffraction.....	51
Small Angle X-Ray Scattering.....	53
Resistometry Measurements.....	62
Tensile Testing.....	63
IV      EXPERIMENTAL RESULTS.....	64
Resistivity.....	64
Small Angle X-Ray Scattering.....	67
Preliminary Studies of Initial Aging.....	67

	<u>PAGE</u>
Change in Zone Size Parameter.....	68
Relative Integrated Intensity.....	110
Wide Angle Diffraction.....	110
Metallography.....	131
V DISCUSSION OF RESULTS.....	132
Small X-Ray Scattering.....	132
CONCLUSIONS.....	152
APPENDIX.....	155
BIOGRAPHICAL SKETCH.....	177
BIBLIOGRAPHY.....	178

## LIST OF TABLES

<u>Table</u>		<u>Page</u>
1	Equilibrium Phases.....	20
2	Machine Parameters.....	57
3	Summary of Aging Series.....	67
4	Summary of Results of Wide Angle Diffraction..	120
5	List of Variables Used in SAXS Program.....	157
6	Data Input for SAXS Program.....	160

## LIST OF FIGURES

<u>Figure</u>	<u>Page</u>
1	Reciprocal Space of the Aluminum Matrix and Guinier-Preston Zones.....26
2	Direction of Incident and Scattered Beam.....32
3	Moment Distribution of a Particle About the Origin.....33
4	Geometric Relation of a Particle to the Origin.....36
5	Schematic Representation of Guinier De Wolff Camera.....52
6	Schematic of Kratky Camera from Interna- tional Union of Crystallography Commission on Crystallographic Apparatus.....54
7	Schematic of Slits System in Kratky Block.....55
8a	Scattering Curve for Lockheed Pyrolitic Graphite.....59
8b	Porod Region of Lockheed Pyrolitic Graph- ite Scatterer.....61
9	Resistivity Aging Behavior of 7075 Wires.....65
10	Arrhenius Plot of Resistivity Maxima.....66
11	Fixed Angle Scattered Intensity for 7075 Alloy.....69
12	Arrhenius Plot of Time to Reach Scattered Intensity of 1.5 Counts Per Second.....70
13	Preliminary Study of Effect of Deforma- tion-Fixed Angle Scattered Intensity.....71



<u>Figure</u>		<u>Page</u>
14	Typical Small Angle Scattering Curve of Directly Aged Sample.....	73
15	Typical Small Angle Scattering Curve from a Preaged Sample.....	75
16	Evolution of Guinier Radius as Determined from SAXS for A, B, D Series.....	77
17	Evolution of Guinier Radius as Determined from SAXS for E, F, FlH Series.....	78
18	Evolution of Guinier Radius as Determined by SAXS for G and H Series.....	80
19	Evolution of the Guinier Radius as Determined by SAXS for J and K Series.....	82
20	Evolution of Guinier Radius as Determined by SAXS for L Series.....	84
21	Evolution of Guinier Radius as Determined by SAXS for M Series.....	85
22	Porod Radius for A, B, D Series as Determined by SAXS.....	88
23	Porod Radius Evolution for E, F, Flh Series as Determined by SAXS.....	90
24	Porod Radius Evolution for J and K Series as Determined by SAXS.....	91
25	Porod Radius Evolution for L Series as Determined by SAXS.....	93
26	Porod Radius Evolution for M Series as Determined by SAXS.....	94
27	Radius of Maximum Abundance for A, B, D Series as Determined by SAXS.....	95
28	Radius of Maximum Abundance for E, F Series as Determined by SAXS.....	96

<u>Figure</u>		<u>Page</u>
29	Radius of Maximum Abundance for FlH Series as Determined by SAXS.....	97
30	Radius of Maximum Abundance for J and K Series as Determined by SAXS.....	98
31	Radius of Maximum Abundance for L Series as Determined by SAXS.....	99
32	Radius of Maximum Abundance for M Series as Determined by SAXS.....	100
33	Particle Size Distribution Evolution for A Series.....	101
34	Particle Size Distribution Evolution for B Series.....	102
35	Particle Size Distribution Evolution for D Series.....	103
36	Particle Size Distribution Evolution for E Series.....	104
37	Particle Size Distribution Evolution for FlH Series.....	105
38	Particle Size Distribution Evolution for J Series.....	106
39	Particle Size Distribution Evolution for K Series.....	107
40	Particle Size Distribution Evolution for L Series.....	108
41	Particle Size Distribution for M Series.....	109
42	Relative Integrated Intensity for A and B Series.....	111
43	Relative Integrated Intensity for E, F, FlH Series.....	112

<u>Figure</u>		<u>Page</u>
44	Relative Integrated Intensity for G and H Series.....	114
45	Relative Integrated Intensity for J and K Series.....	115
46	Relative Integrated Intensity of L Series.....	117
47	Relative Integrated Intensity for M Series....	118
48	Densitometer Scans of Eseries (125°C Age) Guinier-De Wolff Films.....	119
49	Results of Tensile Tests for A, B, D Series...	122
50	Results of Tensile Tests for E, F Series.....	123
51	Results of Tensile Tests for G, H Series.....	124
52	Results of Tensile Tests for J Series.....	126
53	Results of Tensile Tests for K Series.....	128
54	Results of Tensile Tests for L Series.....	129
55	Results of Tensile Tests for M Series.....	130
56	Schematic Representation of Type B Ser-rated Flow.....	143
57	Interaction of a Dislocation Line With the Coherency Strains Surrounding a Guinier-Preston Zone.....	145
58	Representation of Area Created by Passing of a Dislocation Through a Guinier-Preston Zone, Along with the Applicable Geometry.....	147

Abstract of Dissertation Presented to the  
Graduate Council of the University of Florida in  
Partial Fulfillment of the Requirements for  
the Degree of Doctor of Philosophy

GUINIER-PRESTON ZONE EVOLUTION IN 7075 ALUMINUM

by

John Thomas Healey

June, 1976

Chairman: Dr. Robert W. Gould

Major Department: Materials Science and Engineering

This research has been concerned with the growth of Guinier-Preston zones, their transformations, and the relation of these substructures to the mechanical properties of 7075 aluminum. Thermomechanical treatments, as well as thermal preage treatments, were performed on the alloy. The principle technique of this investigation was X-ray small angle scattering.

Mechanical treatments did not change the aging sequence, but did increase the aging kinetics. Preage treatments produce a narrow stable Guinier-Preston zone size distribution which remains stable upon final elevated aging.

Wide angle scattering indicated that no large misfit existed between the matrix and the Guinier-Preston zones,

and that the zones transformed to an intermediate precipitate  $\eta'$ , than to the equilibrium phase  $\eta$ .

## INTRODUCTION

The phenomenon of age hardening in aluminum alloys was first observed by Wilm in 1905. The discovery was quite accidental. Wilm had been trying to harden an aluminum-4% copper-0.5% silicon-0.5% manganese alloy by quenching from 525°C in a manner analogous to steels. The experiment initially was a failure as the material proved to be quite soft, but several days later, while measuring the hardness, Wilm found it had hardened at room temperature. Wilm could not explain this increase, as optically he could not observe any structural differences between the hard and soft specimens. Wilm did not publish this work until 1911, at which time he merely presented the results without attempting to offer an explanation.

The first explanation of this anomaly was offered by Mercia, Waltenberg and Scott, who concluded that since the solid solubility of copper and silicon is higher at 525°C, the increase in strength must be due to the slow precipitation of some second phase at room temperature. Jeffries and Archer further proposed that these second phases were really submicroscopic particles of the equilibrium phase. The proof of the nature of the hardening

agents had to wait until 1938, when Guinier and Preston first demonstrated that small clusters of solute atoms would produce diffuse x-ray scattering at small angles. This technique provided the means to directly study these coherent clusters, today known as Guinier-Preston zones or merely G.P. zones.

The next major advance in the study of precipitation was the continuing development of the transmission electron microscope and the development of sample preparation techniques. This enables the researcher to actually see the zones, their distribution within the matrix, and to follow their evolution with time. Transmission electron microscopy also offered the ability to observe the relationship of the zones to defects in the matrix, such as dislocations and grain boundaries.

Extensive studies into many of the age hardenable systems have been made, employing a wide variety of techniques; hardness measurements, resistometry, small angle x-ray scattering and, somewhat later, transmission electron microscopy. The basic goal of all these investigations has been to obtain an insight into the complex mechanisms of age hardening, and, thereby, be able to predict alloy mechanical properties by a detailed knowledge of the zonal state.

Polmear and Gerold have done much of the early work on the aluminum-zinc-magnesium system. These researchers have studied the effects of various alloy compositions, and, in conjunction with these, many different aging sequences. The next logical step in the investigation of the age hardening process is to study the complex ternary and quaternary commercial alloys. This is the subject of this dissertation. The present investigation is concerned with characterizing the various zonal states of the commercial 7075 alloy (5.7% Zn-2.6% Mg-1.6% Cu), and their interrelation with mechanical properties. The main technique of the investigation will be x-ray small angle scattering.



## CHAPTER I

### REVIEW OF PREVIOUS WORK

Extensive work has been done on the decomposition of aluminum-zinc alloy systems. Some of the earliest work on this system was done by Guinier,<sup>1</sup> who showed that the clusters which formed homogeneously upon quenching were spherical in shape. The rapid growth of the clusters, or Guinier-Preston zones, has been attributed to enhanced diffusion in a system supersaturated with quenched-in vacancies. Resistometry work of Panseri and Federighi<sup>2</sup> has shown the formation energy for vacancies to be 0.70 eV, the activation diffusion energy to be 0.54 eV, and the binding energy between zinc atoms and vacancies to be on the order of 0.05 eV.

Using small angle x-ray scattering, Gerold<sup>3</sup> has shown that the spherical zones continue to grow and maintain a spherical shape until a Guinier Radius of approximately 35 Å is reached. At this size, growth is arrested and the zones transform to an elliptical shape before growth recommences. This shape change is a result of internal rhombohedral straining whose anisotropy causes the elliptical shape.

Gerold<sup>4</sup> has further shown that the composition of the zones can be determined from the integrated intensity. In this manner, the limits of the metastable miscibility gap have been calculated.

Carpenter and Garwood<sup>5</sup> have shown the aging sequence in Al-Zn alloys to be:

Spherical G.P. zones  $\rightarrow$  Elliptical G.P. zones  $\rightarrow$

Rhombohedral  $\alpha'$   $\rightarrow$  Cubic  $\alpha'$   $\rightarrow$   $\epsilon$  (hexagonal zinc)

The rhombohedral  $\alpha'$  phase is a transition phase resulting from a partial loss of coherency of the zones during growth. The rhombohedral  $\alpha'$  phase retains coherency with the (111) plane of the matrix. Further loss of coherency results in the formation of the cubic transition  $\alpha'$  phase. Both of the  $\alpha'$  transition phases remain homogeneous throughout the matrix as they are both nucleated from the homogeneous Guinier-Preston zones. The final equilibrium phase,  $\epsilon$  (hexagonal zinc), is nucleated heterogeneously on dislocations only during high temperature aging or prolonged aging of the  $\alpha'$  phases.

The commercial usefulness of the aluminum-zinc binary alloys is practically non-existent as these alloys will overage at temperatures below room temperature, thereby eliminating the strengthening effect of the Guinier-Preston zones.

The addition of magnesium to the binary aluminum-zinc system greatly alters the aging process of the system. The most important change in the aging character is the ability to retain the enhanced mechanical properties at room temperature. This feature, combined with the fact that the aluminum-zinc-magnesium system provides the highest strengths attainable of age hardenable aluminum alloys, has lead to a considerable amount of research into their aging behavior.

Polmear<sup>6-11</sup> did much of the early work on the Al-Zn-Mg system. Polmear used hardness measurements to follow the aging sequence. By plotting the incubation time of the hardness curves, that time during which no increase in hardness is observed, versus the reciprocal of the aging temperature, Polmear produced a series of c curves whose intersections indicated the equal probability of the existence of two phases. Using this technique, Polmear constructed the surface of the upper temperature limit of stability for Guinier-Preston zones.<sup>11</sup> For an alloy of 5.7 w/o Zn-2.6 w/o Mg, he shows this upper temperature to be approximately 175°C.<sup>11</sup> Polmear explains the greater stability of Guinier-Preston zones with increasing Mg content as the greater ability of Mg + Zn to retain coherency with the aluminum lattice.<sup>7</sup> The explanation for the

clustering of Mg and Zn together can be explained thermodynamically. A mixture of aluminum and zinc, or of aluminum and magnesium, show a positive heat of solution, while a mixture of magnesium and zinc possesses a negative heat of solution. For this reason, the magnesium and zinc atoms will be expected to cluster together on quenching. A minimum in the heat of solution should be obtained at some fixed Mg:Zn ratio. Polmear<sup>11</sup> states that the continuous nature of the Guinier-Preston zone surface indicates that the composition and structure of the zones must remain fairly constant over a wide variation in composition. Gerold,<sup>12-13</sup> however, has shown that the composition of the zone is dependent on the Mg:Zn ratio. If the ratio is greater than unity, the zones have a MgZn composition, and if the ratio is less than unity, the composition becomes  $\text{Mg}_3\text{Zn}_5$ . The continuity of Polmear surface can be explained by the fact that there is not an abrupt change in zinc composition at these particular ratios, but rather a gradual transition between the two compositions, and that the thermal response of the two are very similar.

Nicholson and Lorimer<sup>14</sup> used transmission electron microscopy to determine the upper limit of Guinier-Preston zone stability. They quenched their samples directly from

the solutionizing temperature to the aging temperature, and observed the distribution of phases present. Since Polmear<sup>11</sup> had already shown that nucleation of Guinier-Preston zones was homogeneous while nucleation of  $\eta$  from the solid solution was not, Nicholson and Lorimer<sup>14</sup> described the temperature at which the nucleation switched from homogeneous to heterogeneous as the upper temperature limit of Guinier-Preston zones. The limit determined in this manner was approximately 15°C lower for a 5.9 w/o Zn-2.9 w/o Mg alloy.<sup>14</sup> Lorimer's procedure yields the upper temperature limit for nucleation of zones, while Polmear's gives the upper limit for the existence of zones nucleated at a lower temperature.

Mondolfo, Gjosten and Levinson<sup>15</sup> proposed the sequence of aging in the Al-Zn-Mg system to be:

spherical G.P. zones  $\rightarrow \eta' \rightarrow \eta$

Embury and Nicholson,<sup>16</sup> as well as Tomita et al.,<sup>17</sup> have shown that except for very low concentration (>.5 atomic % Mg), the G.P. zones remain spherical throughout the aging process. Tomita<sup>17</sup> observed the diffuse scatter at the base of the (111) peak in 6.8 atomic % Zn and .06 - 2.0 atomic % Mg alloys, and concluded that when this size effect scatter disappeared, the strain in the matrix caused by the mismatch between the zones and matrix had

become negligible. Without the rhombohedral strains present as in binary Al-Zn alloys, the zones will not undergo a shape change.

Graf<sup>18</sup> has shown that the transition phase  $\eta'$  grows on the (111) planes of the aluminum matrix, although some controversy exists as to the mode of nucleation of the phase. Asano and Hirano<sup>19-21</sup> propose from their calorimetric studies, that Guinier-Preston zones are an independent aging product, and do not act as a nucleation site for the formation of  $\eta'$ . Parker,<sup>22</sup> Polmear,<sup>8,10-11</sup> Thompson<sup>23</sup> and Baba<sup>24</sup> indicate that the presence of additional elements, particularly silver, chromium and copper, aid in the heterogeneous nucleation of  $\eta'$ . Dünkeloh, Kralik and Gerold,<sup>25</sup> as well as Lorimer and Nicholson,<sup>14</sup> support the theory that Guinier-Preston zones larger than a certain critical size can transform directly to the transition phase; the support for this being the homogeneous distribution of  $\eta'$ . The work of Chang and Morral<sup>26</sup> indicates that while the Guinier-Preston zones do not transform directly to  $\eta'$ , zones of sufficient size can act as nucleation sites for the heterogeneous nucleation of the precipitate. The homogeneous distribution of  $\eta'$  often observed would be explained by this process, as the distribution of critically sized zones which could act as

nucleation sites would be homogeneously distributed through the matrix. Bardhan and Starke<sup>27</sup> give the critical Guinier Radius necessary for Guinier-Preston zones to act as nucleation sites at  $35 \text{ \AA}$ , which is curiously similar to the size at which zones change from spherical to ellipsoidal in the binary Al-Zn alloys. While the  $\eta'$  phase is generally accepted to be hexagonal and semicoherent with the aluminum matrix,<sup>15,26</sup> with lattice parameters  $a_0 = 4.96 \text{ \AA}$ ,  $c_0 = 8.68 \text{ \AA}$ ,<sup>77</sup> Ryum<sup>28</sup> finds  $\eta'$  to be monoclinic with lattice parameters  $a=b=4.97 \text{ \AA}$ ,  $c=5.54 \text{ \AA}$  and  $\beta=120^\circ$ . Thackery,<sup>29</sup> on the other hand, finds no evidence for the existence of the  $\eta'$  phase, and proposes the aging process to be:



while speculating that previous x-ray investigations may have mistaken his X phase for  $\eta'$ .

The equilibrium  $\eta$  phase ( $\text{MgZn}_2$ ) can be formed directly by the change of lattice parameter and loss of coherency of  $\eta'$ .<sup>15</sup> The  $\text{MgZn}_2$  phase can also be nucleated heterogeneously at dislocations and grain boundaries.<sup>26,29</sup> With Mg:Zn ratios greater than 3:7,<sup>22</sup> the  $\eta$  phase will itself transform to the equilibrium T  $((\text{Al,Zn})_{49}\text{Mg}_{32})$  phase with aging treatments above  $200^\circ\text{C}$ ; although, it has been shown by Schmalzried and Gerold<sup>12</sup> that this transformation



remains incomplete, even with extended aging at temperatures greater than 200°C and is only completed with aging above 300°C.

Ryum<sup>28,30-31</sup> shows that this aging sequence is only one of a possible three which can occur simultaneously or independently, depending upon the conditions. The possible aging sequences as seen by Ryum are:

SOLID SOLUTION  $\rightarrow \eta$

SOLID SOLUTION  $\rightarrow$  "nuclei"  $\rightarrow \eta'$   $\rightarrow \eta$

SOLID SOLUTION  $\rightarrow$  G.P. zones  $\rightarrow \eta'$   $\rightarrow \eta$

The new "phase" introduced by Ryum<sup>30</sup> ("nuclei") is defined as a vacancy-solute atom aggregate, but with a higher upper temperature limit. Ryum<sup>31</sup> presents the upper temperature limit of the nuclei to be 300°C as opposed to 180°C for Guinier-Preston zones. The first of Ryum's sequences (solid solution  $\rightarrow \eta$ ) would have a high activation energy<sup>31</sup> and would occur heterogeneously on dislocations and grain boundaries, or homogeneously, with a low particle density, after long aging periods. Bardhan and Starke<sup>29</sup> also show the presence of quench-in MgZn<sub>2</sub> in a 5.8 weight % Zn-.71 weight % Mg, but not in a .51 weight % alloy. They attribute this difference to a greater degree of quench clustering in higher magnesium alloys.



Ryum<sup>31</sup> states that the second sequence (solid solution  $\rightarrow$  nuclei  $\rightarrow \eta' \rightarrow \eta$ ) occurs with quenching to room temperature, holding for five seconds, then aging at 150°C. The nuclei were not observed in the transmission electron microscope, with  $\eta'$  lying on {111} matrix planes being the first observable phase. This reaction did not occur in the grain boundary region or adjacent to dislocations in the matrix due to the low vacancy concentration. The final sequence is identical to that presented previously.

Several authors<sup>12,16,29-31</sup> have presented the orientation relationship of the  $\text{MgZn}_2$  phase and the transition phase  $\eta'$  with the matrix. Mondolfo et al.<sup>15</sup> suggest that the basal plane of the hexagonal  $\eta'$  phase lies on the (111) plane of the aluminum with the following relationship:

$$(0001)_{\eta} \parallel (111)_{\text{Al}}, (\bar{1}1\bar{2}0)_{\eta} \parallel (\bar{1}\bar{1}0)_{\text{Al}}$$

Schmalzried and Gerold<sup>12</sup> have proposed three possible orientation relationships between  $\eta$  phase and the aluminum matrix:

$$\text{a.) } (1010)_{\eta} \parallel (100)_{\text{Al}}, (0001)_{\eta} \parallel (011)_{\text{Al}}$$

$$\text{b.) } (1010)_{\eta} \parallel (110)_{\text{Al}}, (0001)_{\eta} \parallel (111)_{\text{Al}}$$

$$\text{c.) } (1010)_{\eta} \parallel (121)_{\text{Al}}, (0001)_{\eta} \parallel (111)_{\text{Al}}$$

Thackery<sup>29</sup> has shown that Gerold's relationship c.) can be written as:

$$(\bar{1}1\bar{2}0)_\eta || (110)_{Al}, (0001)_\eta || (\bar{1}\bar{1}1)_{Al}$$

which would make this orientation identical with that discovered by Mondolfo for  $\eta'$ , thereby indicating a direct transition between the two phases. Embury and Nicholson<sup>16</sup> give the orientation relationship to be:

$$(0001)_\eta || (110)_{Al}, (10\bar{1}0)_\eta || (\bar{1}\bar{1}0)_{Al}$$

which presents a larger mismatch between the two phases than those presented by Gerold.<sup>12</sup> Thackery,<sup>29</sup> examining an aluminum-6 weight % Zn-2 weight % Mg alloy, determined six possible relationships of  $\eta$  to the aluminum matrix.

- 1.)  $(\bar{1}2\bar{1}0)_\eta || (\bar{1}\bar{1}1)_{Al}, (0001)_\eta || (110)_{Al}$
- 2.)  $(\bar{1}2\bar{1}0)_\eta || (\bar{1}\bar{1}1)_{Al}, (30\bar{3}2)_\eta || (110)_{Al}$
- 3.)  $(\bar{1}2\bar{1}0)_\eta || (\bar{1}\bar{1}1)_{Al}, (20\bar{2}1)_\eta || (121)_{Al}$
- 4.)  $(\bar{1}2\bar{1}0)_\eta || (\bar{1}\bar{1}1)_{Al}, (10\bar{1}4)_\eta || (110)_{Al}$
- 5.)  $(0001)_\eta || (\bar{1}\bar{1}1)_{Al}, (10\bar{1}0)_\eta || (110)_{Al}$
- 6.)  $(10\bar{1}0)_\eta || (110)_{Al}, (0001)_\eta || (001)_{Al}$

Type 1 orientations were observed by Thackery to be laths lying on  $\{111\}$  planes of the matrix with Types 2, 3 and 4 basically similar with a rotation of the precipitate on the  $(111)$  planes. Type 5 corresponds to Gerold's Type

b.), while Type 6, which Thackery distinguished as elongated eight-sided platelets, is identical to Gerold's Type c.). Thackery found no evidence for the existence of Gerold's Type a.), or of the Embury-Nicholson orientation relationship. Thackery's Type 1 precipitate is presented as the most common, being nucleated heterogeneously on dislocations and at grain boundaries and forming as platelets on (111) matrix planes. Type 5 Thackery represents as forming only as coarse particles resulting from direct high temperature quenches, while Type 6 constitutes the majority of particles in samples first quenched to room temperature then aged.<sup>29</sup>

Ryum<sup>28</sup> found evidence for the existence of all three orientations proposed by Gerold, Embury and Nicholson's relationship, and those of Thackery. Ryum<sup>28</sup> also noted that Gerold's orientation Type a.) had an appearance similar to that of Thackery's X phase.<sup>29</sup>

Resistometry has been widely used to calculate the formation and activation energies of vacancies and vacancy complexes.<sup>2,14,23,32-39</sup> Panzeri and Federighi<sup>2,34</sup> did much of the early work with resistivity on the aluminum-zinc-magnesium system. By measuring the time to reach a maximum of resistivity as a function of aging temperature, they were able to calculate the values for the binding en-

ergy of zinc vacancy couples to be .06 eV and that of magnesium vacancy couples to be .54 .08 eV,<sup>34</sup> a value also given by Gould and Gerold.<sup>40</sup> They also concluded that magnesium vacancy couples can diffuse freely at room temperature, and that the movement of zinc atoms occurs by means of these couples, and not via single vacancies as in binary aluminum-zinc alloys.

Perry,<sup>33,41</sup> by employing the initial rate of aging as well as the time to peak resistivity, has determined the apparent vacancy formation energy to be .70-.71 eV. In working with concentrated (i.e., 10 weight %) zinc alloys, Perry<sup>41</sup> contends that the zinc vacancy binding energy measured is not the true binding energy, but merely an effective value obtained due to the clustering of zinc atoms on quenching; the value Perry obtained was .06 eV, in agreement with Panseri. Perry, however, obtains a vastly different binding energy (.17 eV) for the magnesium vacancy complexes, using a .009 atomic % Mg-4.01 atomic % Zn alloy.<sup>35</sup> Perry also notes that this small addition of Mg was sufficient to slow down the aging process due to the trapping of the vacancies by magnesium atoms. Panseri and Federighi,<sup>34</sup> as well as Gould and Gerold,<sup>40</sup> note that magnesium initially slows the aging process by trapping vacancies, but also extends the aging time by up to an

order of magnitude. This effect is due to the fact that magnesium will act as a vacancy source when the matrix has become depleted in vacancies.

Ceresara and Fiorini,<sup>37</sup> using a similar resistometric technique, have measured the total kinetic activation energy in Al-5 weight % Zn-1 and 3.4 weight % Mg alloys to be .67 eV, independent of magnesium concentration.

Several authors<sup>19-21,42-43</sup> have made use of a calorimetric method to study the thermal stability of Guinier-Preston zones, their reversion, and transformations to transition and equilibrium phases. Asano and Hirano<sup>19-21</sup> have shown that Guinier-Preston zones become stable to higher temperatures with longer aging times at lower temperatures. Their calorimetric scans indicate that with short aging times, the reversion of the zones is complete before formation of  $\eta'$ , which would indicate heterogeneous nucleation of the transition phase, independent of the zones. However, with longer low temperature aging times, the heat absorption of zone reversion overlaps the heat evolution of  $\eta'$  formation, which would imply some sort of  $\eta'$  nucleation on the zone sites.

Of particular importance to commercial alloys is their quench rate sensitivity, especially due to the presence of secondary alloying elements.

Several workers<sup>22-23,44-46</sup> have studied the quench rate sensitivity of Al-Zn-Mg alloys with the additions of chromium, silver, zirconium, manganese and copper. The consensus of these authors is that all these secondary alloy elements produce quench rate sensitivity, roughly in the order presented. The cause, however, is not the same for all these elements. In the case of copper, which presents the least effect, Mondolfo<sup>47</sup> has shown that the copper precipitate (CuMgAl) can precipitate with a lower activation energy and, being structurally similar to MgZn<sub>2</sub>, can act as easy nucleation sites for this phase; much the same is true for zirconium (Al<sub>2</sub>Zr),<sup>23</sup> and also for silver which clusters readily in aluminum alloys.<sup>42</sup> The effects of chromium and manganese are more complicated. Both of these elements have a low solubility in aluminum and would tend to form clusters,<sup>46</sup> but more important is that both elements act to retard recrystallization by forming subgrain structure.<sup>46</sup> This structure acts as both vacancy sinks and as additional heterogeneous nucleation sites, the former removing vacancies from the aging sequence and the latter, solute atoms. Both of these effects will be detrimental to the final mechanical properties.

The most important parameter affecting the mechanical properties is the size and distribution of the prepre-

precipitates and the precipitates. The only two ways to measure these parameters directly are small angle scattering and transmission electron microscopy. Many investigators have used TEM measurements to determine the precipitates present,<sup>46</sup> their orientation relationship with the matrix<sup>12,14,27,29,30-31</sup> and distribution within the matrix.<sup>26,48-53</sup> The lack of resolution during the early stages of aging and the tediousness of measurement of G.P. zone size using transmission electron microscopy makes x-ray small angle scattering the most accurate and fastest method of direct measurement of the precipitation process.

Guinier<sup>54-56</sup> and Gerold<sup>57-59</sup> developed much of the theory as it relates to the solid solution; this will be presented later. In addition, Gerold<sup>12-13,25,58-60</sup> also did much of the early work on the Al-Zn-Mg system. Tomita,<sup>17</sup> as well as Bardhan and Starke,<sup>27</sup> have shown that except for the very low concentration alloys, there is no zone size arrest, as in the Al-Zn system. Harkness, Gould and Hren<sup>48-50</sup> have developed the mathematics for converting the measured experimental small angle scattering parameters into actual particle size distributions; their development will be presented elsewhere.



Most of the direct measurements of G.P. zone size distributions as a function of aging conditions have been done on pure research grade alloys. The next logical step would be to measure their evolution in a commercial alloy complicated by the presence of a large number of alloying agents and also by the presence of impurity atoms. The purpose of this work will be to measure quantitatively the evolution of Guinier-Preston zones in a commercial 7075 alloy, the effects of thermomechanical treatments on the zones, and their relationship to the mechanical properties. The main technique of this investigation will be x-ray small angle scattering.

### Equilibrium Phases

The equilibrium phases possible in the aluminum-rich corner of the aluminum-zinc-magnesium system are given in Table 1.

The phases possible involving the trace impurity and alloying elements present, such as Si, Mg, Ti, Cr and Mn, will not be considered as their concentrations are sufficiently low that they will be either incorporated in solid solution, miscible in one of the other equilibrium phases, or so widely dispersed that they will have little effect on the alloy as a whole.



Table 1

## Equilibrium Phases

Phase	Notation	Crystal Structure	Lattice Parameter Å	
Al	$\alpha$	FCC	$a_o = 4.049$	(47)
MgZn <sub>2</sub>	$\eta$	HCP	$a_o = 5.16-5.22$	(47)
CuMgAl			$c_o = 8.49-8.55$	(47)
(Al,Zn) <sub>49</sub> Mg <sub>32</sub> CuMg <sub>4</sub> Al <sub>6</sub>	T	cubic	$a_o = 14.29-14.71$	(47)
?	X	HCP	$a_o = 2.66$ $c_o = 4.94$	(29)
FeAl <sub>3</sub>	$\chi$	Monoclinic	$a = 15.48$ $b = 8.083$ $c = 12.17$ $\beta = 107^\circ 43'$	

The  $\alpha$  phase lattice parameter varies linearly from a low of 4.018 Å at 57 weight % zinc to a maximum of 4.1294 at 17 weight % magnesium. The  $\eta$  phase, MgZn<sub>2</sub>, is a prototype of the hexagonal Laves Phase.<sup>47</sup> Thomas and Nutting<sup>88</sup> have shown that an appreciable amount of copper can also be dissolved in the  $\eta$  phase. Mondolfo, Gjosten and Levinson<sup>15</sup> have shown that the  $\eta$  phase is the only ternary phase that occurs with aging temperatures below 200°C.

The T phase, (Al,Zn)<sub>49</sub>Mg<sub>32</sub>, is a complex cubic structure of 162 atoms to the unit cell.<sup>47</sup> The lattice

parameter varies as the Al:Zn ratio with the magnesium content remaining essentially constant. Little, Hume-Rothery and Raynor<sup>89</sup> have shown that the T phase can dissolve a significant amount of copper also, as the  $\text{CuMg}_4\text{Al}_6$  phase is completely miscible with T. Mondolfo et al.<sup>15</sup> have shown that the T phase is slow to nucleate and is present only with extended aging above 200°C.

Thackery<sup>29</sup> indicates an undetermined phase present in Al-6 weight % Zn-2 weight % Mg, and designates it as X phase. He determined it to be hexagonal, appearing as triangular-shaped particles whose sides are parallel to (110) matrix planes, and whose lattice parameters are extremely similar to those of pure zinc. The X phase may truly be zinc precipitated from small zinc clusters with limited quantities of alloying elements in solid solution.

The  $\chi$  phase is the result of iron being an impurity in all commercial aluminum alloys. It is very slow to homogenize and does not tie up any of the major alloying elements, and is subsequently important to the aging process only to the degree that it can act as a heterogeneous nucleation site. The real importance of the  $\chi$  phase lies in its detrimental effect on the fracture mechanics of the alloy.

The chromium addition is present to enhance stress corrosion resistance and the phases formed do not greatly effect the aging process. Titanium is added as a grain boundary refiner, and the other impurities present may affect the kinetics of the aging process, but do not greatly tie up the effective alloying constituents.

## CHAPTER II

### THEORY OF SMALL ANGLE X-RAY SCATTERING

Small angle scattering has a variety of applications; the study of macromolecules, polymers and clays. In 1938, Guinier<sup>1</sup> proposed their use for the study of inhomogeneities in dilute alloy systems. There are several restrictions placed on the study of dilute alloy systems. First of all, the alloy must contain regions of electron density inhomogeneities of a size greater than atomic radii. Secondly, these inhomogeneities must be smaller than 1000 Å, the approximate upper limit of resolution at that time.

The inhomogeneity must have a fairly significant electron density difference from the matrix and must be reasonably concentrated (approximately 1% of scatterers for Guinier-Preston zones) in order to produce measurable scatter in a thin sample necessitated by x-ray absorption in the sample. (The thickness for an aluminum alloy using MoK $\alpha$  radiation is approximately 0.7 mm.)

The last of these restrictions, a measurable scatter, is largely restricted by instrumental parameters. As the electronics become quieter and more sensitive, the

minimum quantity of inhomogeneities also becomes lower. This is a result of the statistics of the count rate.

To understand the origin of the scatter, the concept of the reciprocal lattice must first be understood. In reciprocal space, all lattice planes ( $hkl$ ) of real space are represented as reciprocal lattice nodes. The size, shape and spacing of the reciprocal lattice nodes are inversely proportional to the size and shape of the crystal in real space, and the interplanar spacings, respectively. Thus, large crystals in real space would be represented as small point-like nodes in reciprocal space, while large platelets would appear as long narrow cylinders in reciprocal space.

In the case of Guinier-Preston zones, there are two sets of reciprocal lattices; the matrix and the G.P. zones themselves. The matrix, being large crystals, will be represented by sharp reciprocal lattice points, neglecting stress and temperature effects. The G.P. zones will have their reciprocal lattice nodes centered at the same position as the matrix nodes, as the G.P. zones have the same crystal structure as the matrix. However, the small size of the G.P. zones produces reciprocal lattice nodes which are broad and spread.

Applying the Ewald Sphere concept, diffraction will occur whenever the diffraction beam vector,  $\frac{S}{\lambda}$  ( $|S| = \frac{1}{\lambda}$ ), intersects a reciprocal lattice node. The diffraction vector,  $S$ , is drawn from the center of the Ewald Sphere, whose radius,  $|\frac{S_0}{\lambda}|$ , is directed to the (000) node, to any reciprocal lattice node that intersects the Ewald Sphere. When this happens, diffraction is said to occur. In the case of large crystals where the nodes are sharp and point-like, diffraction is restricted to these points, with nothing occurring between them. This diffraction is restricted to definite angular regions. However, with small G.P. zones, the nodes are large; thus, there is a greater probability of the Ewald Sphere intersecting a reciprocal lattice node of the G.P. zones surrounding those of the matrix. Figure 1 shows reciprocal space of the matrix and the G.P. zones. This accounts for the greater angular range of diffraction for the G.P. zones. The two diffraction peaks superimpose and the G.P. zone peak is evidenced as a deviation from a Gaussian distribution at the base of the matrix peak. This scatter is present around all the Bragg peaks, as well as the (000) node. Observation of this scatter is generally simplified around the (000) node, as such effects as strain and tem-

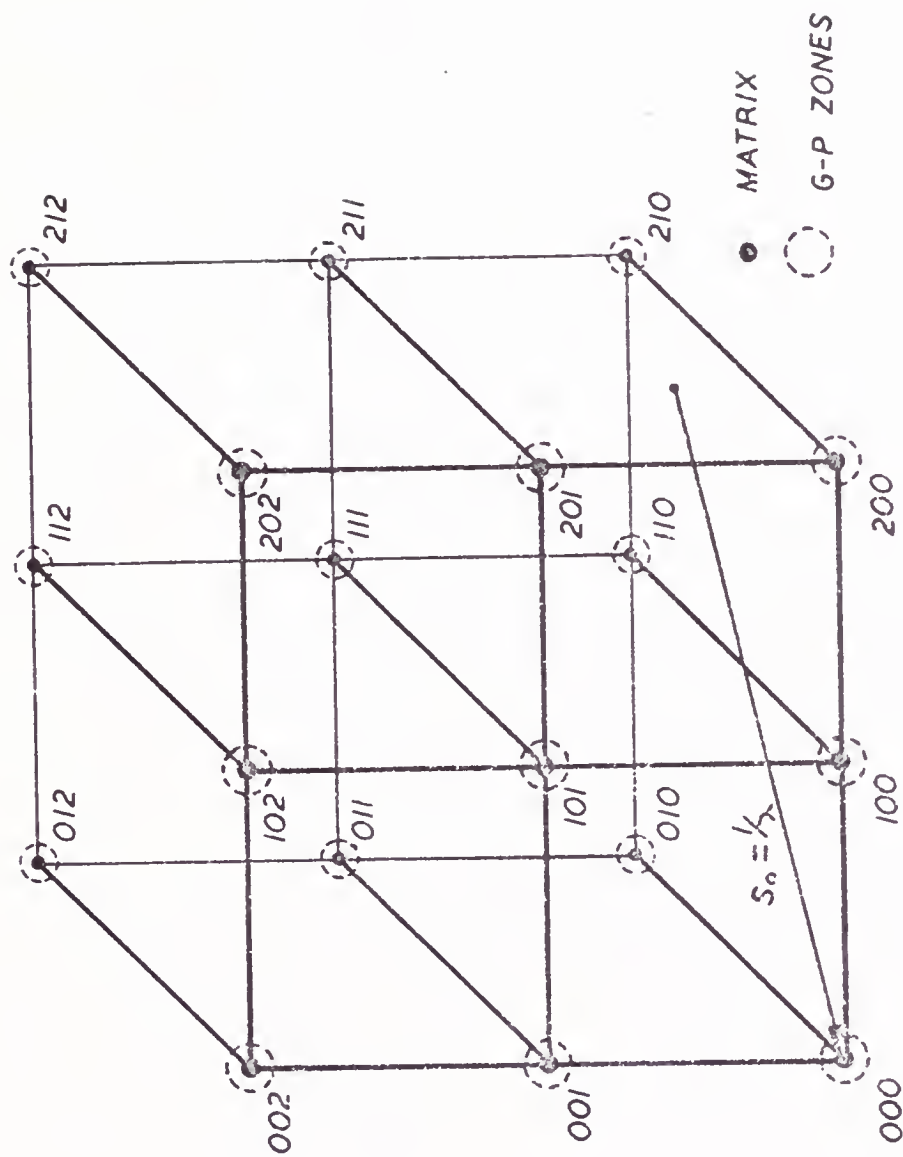


Figure 1. Reciprocal Space of the Aluminum Matrix and Guinier-Preston Zones

perature which cause broadening of the Bragg diffraction peaks are not present around the (000) node. The intensity is also maximized around the (000) node as the atomic scattering factor is maximized here, and the Compton Scattering, which subtracts from the intensity (as  $(1-\cos\theta)$ ), is minimized.

In order to understand the small angle scattering that results from the Guinier-Preston zones, it is necessary to start with the first principles of x-ray scattering. A dilute system is one in which there is a large volume available per particle as compared to the total volume of all the small particles. In addition, thin samples will only be considered such that absorption effects can be neglected. The basic development of Guinier<sup>1,2</sup> will be mostly followed.

For the case of a small isolated crystal, such as a G.P. zone, Guinier<sup>54</sup> has shown that the scattering power per unit cell is:

$$I(s) = \frac{F_{hkl}^2}{V V_c} \sum_h \sum_h \sum_\ell |\sum (s - r_{hkl}^*)|^2$$

where:  $V$  is the volume of the diffracting crystal

$V_c$  is the volume of a unit cell

$F_{hkl}$  is the structure factor of a particular node



$\Sigma(s)$  is the Fourier transform of the form factor  
 $r_{hkl}^*$  is the structure factor of a particular node  
 $s = \frac{\vec{S} - \vec{S}_0}{\lambda}$

Around the (000) node, the vector  $r_{hkl}^* = 0$ . Thus, around the (000) node:

$$I(s) = \frac{F_{(000)}^2}{V_c} |\Sigma(s)|^2$$

For very small angles, the structure factor,  $F_{(000)}$ , is equal to the number of electrons (N) present in the unit cell. The average electron density ( $\rho$ ) of the unit cell is then:

$$\rho = \frac{F_{(000)}}{V_c} = \frac{N}{V_c}$$

The total scatter ( $I_N(s)$ ) from all electrons in the crystal of total volume V is given by Guinier<sup>54</sup> as:

$$I_N(s) = I(s) \frac{V}{V_c} = \rho^2 \Sigma |(s)|^2$$

where:  $\frac{V}{V_c}$  is the total number of unit cells in the crystal

Thus, the maximum scattered intensity occurs at  $s=0$ , where  $\Sigma(0) = V$ .

$$I_{\max} = \rho^2 V^2$$

This maximum intensity peak of large crystals is masked,

however, by the main unscattered beam. Since  $s = \frac{2\sin\theta}{\lambda}$  where  $\theta$  is small,  $s = \frac{2\theta}{\lambda} = \frac{\epsilon}{\lambda}$ . Also,  $s \approx \frac{1}{d}$ ; therefore:

$$\epsilon = \frac{\lambda}{d}$$

The minimum angle where scatter can be observed is  $\epsilon \approx 10^{-3}$  radians. This would correspond to a particle diameter ( $d$ ) of approximately 1000 Å.

A Guinier-Preston zone can be considered as an isolated crystal within a medium other than vacuum, as long as it is a dilute system, as defined previously; the intensity from each particle will merely add. If the medium electron density is given as  $\rho_0$  and the isolated particle electron density as  $\rho$ , the scattering power per particle is:

$$I(s) = (\rho - \rho_0)^2 |\Sigma(s)|^2$$

Guinier<sup>54</sup> has determined that in order to obtain the average scattering power per particle if all particles are identical,  $|\Sigma(s)|^2$  must be averaged over the entire sphere of radius  $s = |s|$ . Thus,

$$I(s) = (\rho - \rho_0)^2 \left\{ \begin{array}{l} \text{average value of } |\Sigma(s)|^2 \\ \text{over the sphere} \\ \text{of radius } s = |s| \end{array} \right\}$$

To obtain the average value of  $\Sigma(s)$ , the form function must be integrated over the volume, and for the case of

spheres :

$$\Sigma(s) = \int_V \exp(2\pi i s \cdot x) dV_x$$

Guinier<sup>54</sup> has shown that for a spherical-shaped particle :

$$\Sigma(s) = \frac{4}{3} \pi a^3 \phi(2\pi sa)$$

for a sphere of radius  $a$ . Where the function  $\phi(2\pi sa)$  is given as :

$$\phi(2\pi sa) = 3 \left[ \frac{\sin 2\pi as - 2\pi as \cos 2\pi as}{(2\pi as)^3} \right]$$

Thus, the scattering power per particle is given by :

$$I(s) = [(\rho - \rho_0) \frac{4}{3} \pi a^3]^2 \phi^2(2\pi as)$$

We now wish to approximate the curvature of the intensity curve at the center ( $s=0$ ). The total scattering power  $I_N(s)$  for  $N$  unit cells of a particle of volume  $V$  has been shown by Guinier<sup>54</sup> to be :

$$I_N(\vec{s}) = (\rho - \rho_0)^2 |\Sigma(\vec{s})|^2$$

where:  $\Sigma(\vec{s}) = V$  at  $s=0$

Thus :

$$I_N(0) = (\rho - \rho_0)^2 V^2$$

For an isolated particle, the total number of scattering electrons  $n = \rho V$ . For a particle in a matrix, an effective number of scattering electrons can be defined as :

$$n = (\rho - \rho_0)V \text{ at } s = 0$$

The total scattering power per particle,  $n^2 = (\rho - \rho_0)V$ , at  $s=0$  decreases with  $s$  as  $n^2(1-Ks^2)$ .  $K$ , the curvature at the center of the intensity curve, is related to a simple geometric parameter of the particle, and is independent of the shape of the particle. The approximation of this curvature at the center of the intensity curve is known as the Guinier approximation.

$S_0$  is the direction of the incident beam on the scattering particle, as shown in Figure 2. As can be seen, for very small scattering angles  $\vec{s}$  is in the direction  $D$ , approximately normal to  $S_0$ , where  $s = (S - S_0)/\lambda$ .  $\vec{s}$  is in the plane of the incident and scattered rays, and  $|\vec{s}| = \frac{\epsilon}{\lambda}$  for small angles. Take any vector,  $\vec{x}$ , in real space. Then,

$$\vec{s} \cdot \vec{x} = sx_D$$

where  $x_D$  is the projection of the vector  $x$  on  $D$ . In order to calculate the function  $\Sigma(s)$ , we must evaluate the integral:

$$\Sigma(s) = \int_V \sigma(x_D) \exp(2\pi i \vec{s} \cdot \vec{x}_D) dV_x$$

where  $\sigma(x_D)$  is the cross sectional area of the particle along a plane normal to  $D$  at a distance  $x_D$  from the origin as shown in Figure 3. If the origin of the coordinate

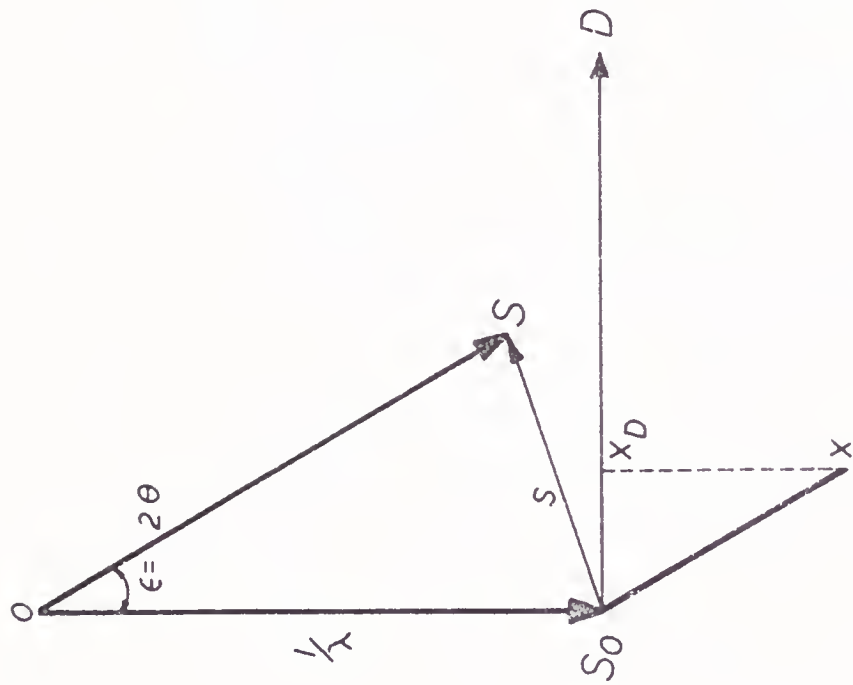


Figure 2. Direction of Incident and Scattered Beam

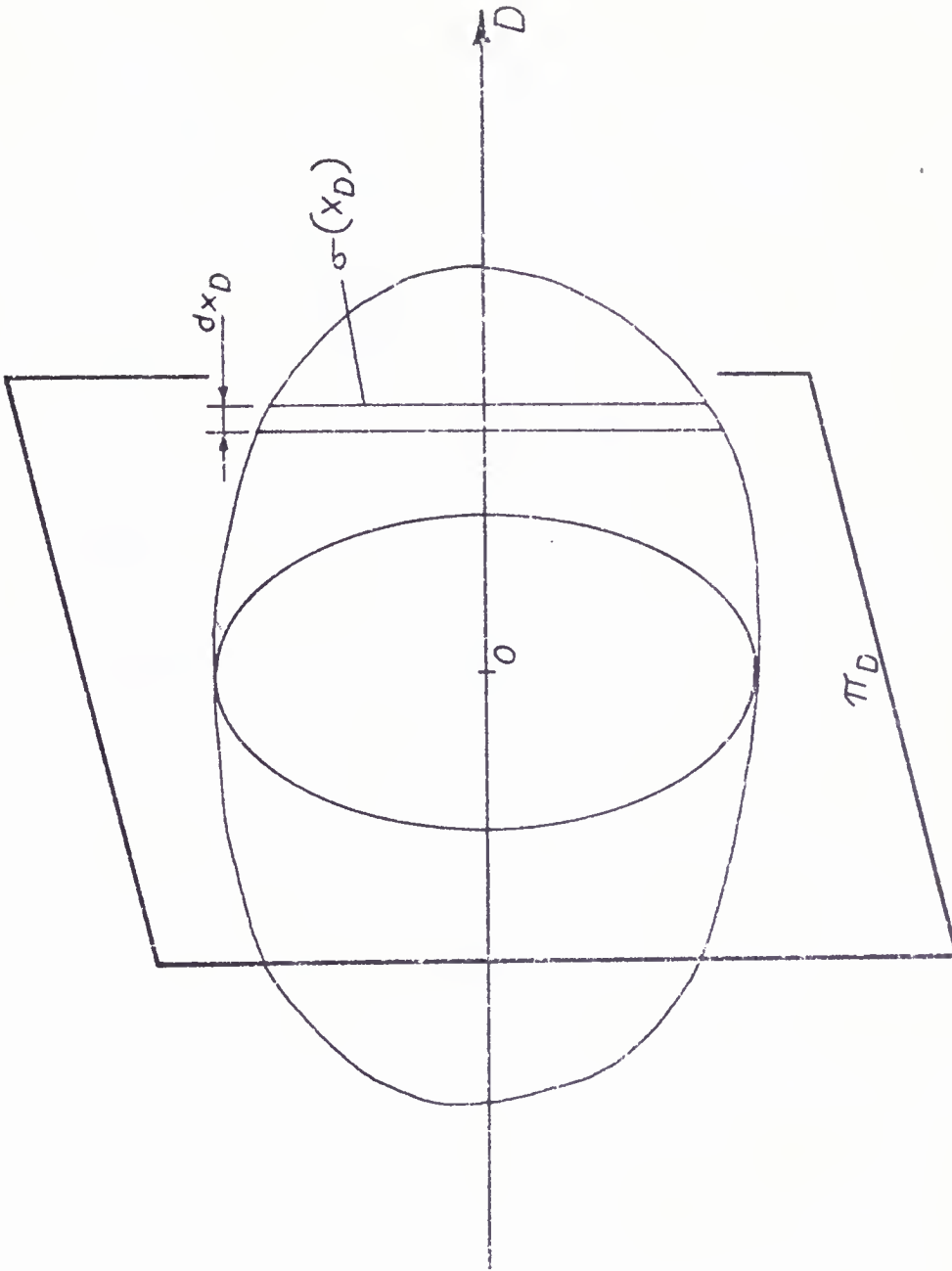


Figure 3. Moment Distribution of a Particle About the Origin

system in real space is chosen to be the center of gravity of the particles, then the sum of the moments of the particles about the origin is zero. Thus, since

$$\Sigma \vec{x} dV_x = 0$$

and

$$dV_x = \sigma(x_D) dx_D$$

$$\int x_D \sigma(x_D) dx_D = 0$$

Now we can expand the exponential function in the equation of  $\Sigma(\vec{s})$ , neglecting terms of order greater than  $s^2$ , since  $s$  remains very small within the scattering particle. Now:

$$\Sigma(s) = \int_V \sigma(x_D) \exp(2\pi i \vec{s} \cdot x_D) dV_x =$$

$$\int \sigma(x_D) dx_D + 2\pi i s \int x_D \sigma(x_D) dx_D - 2\pi^2 s^2 \int x_D^2 \sigma(x_D) dx_D$$

The first term of the above equation is the volume of the particle, while the second term is zero, due to the choice of the origin as shown above. In order to evaluate the third term, an additional term,  $R_D^2$ , must be defined:

$$R_D^2 = \frac{1}{V} \int x_D^2 \rho(x_D) dx_D$$

$R_D$  is defined as the average inertial distance along  $D$  to the plane  $\pi_D$  passing through the origin and perpendicular to  $D$ .

Thus:

$$\Sigma(\vec{s}) = V - 2\pi^2 s^2 V R_D^2$$

which can be rewritten in exponential form as:

$$\Sigma(\vec{s}) = V \exp(-2\pi^2 s^2 R_D^2)$$

Then, the scattering power per particle:

$$I(\vec{s}) = (\rho - \rho_0)^2 |\Sigma(s)|^2$$

becomes

$$I(s) = (\rho - \rho_0)^2 V^2 \exp(-4\pi^2 s^2 R_D^2)$$

$R_D$ , as written here, assumes all particles have identical orientations. For a random orientation of particles,  $R_D^2$  must be replaced by  $\bar{R}_D^2$ , which is the average value of  $R_D^2$  for all directions of  $D$ .

In order to calculate  $R_D$ , we must remember that  $D$  is merely one coordinate axis of an orthogonal coordinate system. The other two axes,  $U$  and  $V$ , are shown in Figure 4, along with  $D$ . The origin is the center of gravity and any point may be represented as  $x_D$ ,  $x_U$  or  $x_V$ . The distance  $r$  of any point from the origin is given as

$$r^2 = x_D^2 + x_U^2 + x_V^2$$

Similarly,  $R$ , which is the radius of gyration of a particle about its center of gravity, is given by:



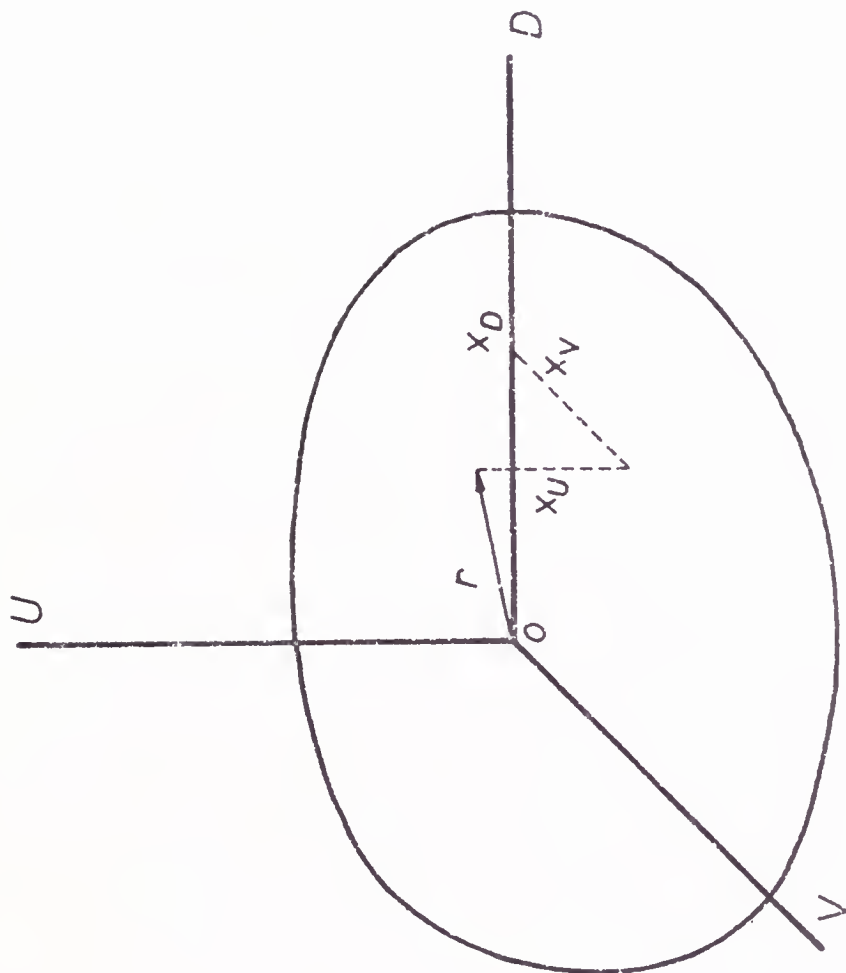


Figure 4. Geometric Relation of a Particle to the Origin

$$R^2 = R_D^2 + R_u^2 + R_V^2$$

where  $R_D$ ,  $R_u$  and  $R_V$  are the inertial distances taken along the three coordinate axes D, U and V, respectively. Now, if we consider the rotation of the three coordinate planes about the origin, as would be the case for random particle orientation,  $R^2$  remains constant and  $\bar{R}_D^2$ ,  $\bar{R}_u^2$  and  $\bar{R}_V^2$ , on the average value, are equal, Therefore:

$$3\bar{R}_D^2 = R^2$$

This makes the average scattering power per particle

$$I(s) = n^2 \exp\left(-\frac{4\pi^2 s^2 R^2}{3}\right) = n^2 \exp\left(-\frac{4\pi^2 R^2}{3\lambda^2}\right)$$

The radius of gyration of a sphere is given as

$$R = \left(\frac{3}{5}\right)^{1/2} a$$

Thus:

$$I(s) = n^2 \exp\left(-\frac{4\pi^2 a^2 \epsilon^2}{5\lambda^2}\right)$$

By taking the logarithm of both sides of the equation:

$$\ln I(s) = \ln n^2 - \frac{4\pi^2}{3\lambda^2} .4343 R^2 \epsilon^2$$

Guinier<sup>54-55</sup> has shown that the radius of the particles can be calculated from the slope of the line obtained by plotting  $\ln I(s)$  versus  $\epsilon^2$ . Thus, R, assuming all parti-

cles are the same size and randomly oriented in a dilute system, is given as:

$$R = .416\lambda\sqrt{-\alpha}$$

A system does not usually contain all identical spherical particles, but a size distribution is usually present. To correct for this, an integration must be made to account for each size particle:

$$I(s) = (\rho - \rho_o)^2 \int_0^{\infty} n(a) a^6 (1 - \frac{4\pi^2 s^2 a^2}{5}) da$$

where  $n(a)$  is the number of particles of radius  $a$  and the  $a^6$  term is the result of  $V^2 = Ka^6$ . This can be written as:

$$I(s) = (\rho - \rho_o)^2 N_o K | \langle a^6 \rangle - \frac{4\pi^2}{5} \langle a^8 \rangle |$$

where  $N_o$  is the total number of particles and  $\langle a \rangle$ , the average value of  $a$ , is obtained by:

$$\langle a^n \rangle = \frac{1}{N_o} \int_0^{\infty} n(a) a^n da$$

Rewriting the intensity equation in exponential form:

$$I(s) = (\rho - \rho_o)^2 N_o \langle a^6 \rangle \exp \left| -\frac{4\pi^2}{5} s^2 \frac{\langle a^8 \rangle}{\langle a^6 \rangle} \right|$$

Baur and Gerold<sup>58-59</sup> determined that by plotting  $\ln I(s)$  versus the scattering angle squared ( $\epsilon^2$ ), one obtains a value for the Guinier approximation which is defined as:

$$R_G = \left| \frac{\langle a^8 \rangle}{\langle a^6 \rangle} \right|^{1/2}$$

Porod<sup>61</sup> has also developed an approximation for the scattering curve, but his deals with the tail region of the curve, rather than the central region. Porod uses the approximation of the form factor:

$$\Sigma(s) = \int \exp(-2\pi i s \cdot x) dV_x$$

The scattering intensity may be written as

$$I(s) = \frac{(\rho - \rho_0)^2}{8\pi^3} \left[ \frac{4\pi a^2}{s^4} + \frac{1}{\pi s^6} - \frac{4a}{s} \sin 4\pi a s \right. \\ \left. + \left( \frac{4\pi a^2}{s^4} - \frac{1}{\pi s^6} \right) \cos \pi a s \right]$$

If there exists a distribution of spheres of radius  $a_K$  which varies between  $a_1$  and  $a_2$ , and the number of spheres of radius  $a_K$  per unit mass is given by  $g_K$ , then the intensity may be written as:

$$I(s) = \frac{(\rho - \rho_0)^2}{8^3} \left[ \Sigma g_K 4\pi a_K^2 \frac{1}{s^4} + \dots \right. \\ \left. + \Sigma \cos 4\pi a_K s [\dots] + \Sigma \sin 2\pi a_K s [\dots] \right]$$

For the case where  $(2a_1s - 2a_2s)$  is much larger than unity, the two sinusoidal summations go to zero as the positive terms cancel the negative terms. Therefore, for a large  $s$ , the only remaining term is that containing  $\frac{1}{s^4}$ . For large  $s$ ,  $I(s)$  is written as  $I_{\text{asym}}$ , or the asymptotic values of the intensity.

$$I_{\text{asym}} = \frac{(\rho - \rho_0)^2}{8\pi^3} \left[ \sum g_K 4\pi a_K^2 \frac{1}{s^4} \right]$$

The total surface of the particles per unit mass is given by  $S = \sum g_K 4\pi R_K^2$ . Then, for the point collimation:

$$I_{\text{asym}} = \frac{(\rho - \rho_0)^2}{8\pi^3} \frac{S}{s^4}$$

Another important property of the scattering intensity is the total integrated intensity,  $Q$ . Guinier and Fournet<sup>55</sup> have shown that the total integrated scattering intensity is given by:

$$Q = \frac{V}{V_a} (\rho - \rho_0)^2 dV = 4\pi \int_0^\infty s^2 I(s) ds$$

In the case of a metal alloy, the electron densities,  $\rho$  and  $\rho_0$ , must be computed as the weighted average of the elemental concentration in both the particle and the matrix. Then, as shown by Gerold:<sup>57-59</sup>

$$\rho = \frac{1}{V_a} [\bar{Z}_B + M_1(Z_A - \bar{Z}_B)]$$

$$\rho_0 = \frac{1}{V_a} [\bar{Z}_B + M_2(Z_A - \bar{Z}_B)]$$

where:  $\rho$  is the electron density of the particles

$\rho_0$  is the electron density of the matrix

$V_a$  is the atomic volume

$M_1$  is the solute concentration in the particles

$M_2$  is the solute concentration in the matrix

$Z_A$  is the atomic number of the solute

$\bar{Z}_B$  is the average atomic number of the solvent

It is necessary to use  $\bar{Z}_B$  because in an alloy, several solvent elements may be present; therefore, the average atomic number must be used to obtain the electron density. Then, the difference in electron density is given by:

$$\begin{aligned}(\rho - \rho_0) &= \frac{1}{V_a} [M_1(Z_A - \bar{Z}_B) - M_2(Z_A - \bar{Z}_B)] \\&= \frac{1}{V_a} [(M_1 - M_2)(Z_A - \bar{Z}_B)] \\(\rho - \rho_0)^2 &= \frac{1}{V_a} [(M_1 - M_2)^2 (Z_A - \bar{Z}_B)^2]\end{aligned}$$

If  $p$  represents the total volume of particles transformed and  $cpV$  the total volume of all particles, we can get the average solute concentration,  $M_A$ , in the bulk alloy as:

$$cM_1 + (1 - C)M_2 = M_A$$

and also the integrated intensity as a function of concentrations:

$$Q = \frac{pc}{V_a} (1 - C)(M_1 - M_2)^2 (Z_A - Z_B)^2$$

The problem remains now of evaluating the integrated intensity from the measured scattered intensity. The intensity measured by a radiation detector,  $E(s)$ , is given by:

$$E(s) = \frac{I_e}{4r^2} n f E_o I(s) de^{-\mu d}$$

where the constant factor,  $\frac{I_e}{4r^2} n f$ , can be written as a constant, K. Then:

$$E(s) = K E_o I(s) de^{-\mu d}$$

where:  $K = \frac{I_e}{4r^2} n f$

$I_e$  is the Thompson factor ( $7.9 \times 10^{-26} \text{ cm}^2$ )

$n$  is the number of atoms per  $\text{cm}^3$

$f$  is the surface area of the detector

$r$  is the sample to detector distance

$E_o$  is the incident beam intensity

$I(s)$  is the scattering power

$d$  is the thickness of the sample

$\mu$  is the linear absorption coefficient

This equation holds true for a beam of x-rays of point cross section. In order to evaluate the intensity measured from a line-shaped beam, Guinier and Fournet<sup>55</sup> have derived the following integration:

$$E(s) = K E_o de^{-\mu d} \frac{1}{t_o} \int I(s^2 + t_o^2)^{1/2} dt$$

where  $t$  is a reciprocal lattice parameter related to the length of the line beam. The determination of the integrated intensity is accomplished by evaluating the inte-

gral:

$$Q = 4\pi \int_0^{\infty} s^2 I(s) ds = 4\pi \int_0^{\infty} I(s^2 + t^2)^{1/2} dt ds$$

Guinier and Fournet<sup>55</sup> have shown that this leads to

$$Q = \frac{2y}{\pi E_0 r \lambda d} 2\pi \int_0^{\infty} s E(s) ds$$

where  $2y$  is the width of the detector-receiving slit. In order to evaluate the integral:

$$\int_0^{\infty} s E(s) ds$$

the Porod approximation for the tail of the scattering curve must be adjusted for a line-shaped beam to:

$$E(s) = ks^{-3}$$

Then:

$$\int_0^{\infty} s E(s) ds = \int_0^{S_0} s E(s) ds + S_0^2 E(S_0)$$

All of the above equations assume a dilute system, i.e., no interparticle interference, monoshaped particles and identical composition of all particles. If the system is not sufficiently dilute, the diffraction maxima will not coincide with  $s=0$ , but will be centered at some finite  $s_0$ . It is still possible to analyse the curvature at the center of the scattering curve, i.e., the Guinier region, and the tail of the curve, the Porod region.



Gerold<sup>3</sup> has derived an expression for the Porod radius ( $R_p$ ) by assuming a constant volume fraction of the scattering zones. Combining this assumption with the scattering curve, he concluded that the surface area of the zones ( $S$ ) computed at large angles should be given by:

$$S = 4\pi N_V \langle a^2 \rangle = \frac{I(s)s^4 8\pi^3}{(\rho - \rho_0)^2} N_V$$

Combining this with the total volume of the particles:

$$cV = \frac{4}{3} \pi \langle a^3 \rangle N_V$$

where:  $V$  is the total volume of irradiated material

$c$  is the volume fraction of the scattering particles

Gerold<sup>3</sup> solved for the expression  $\frac{cV}{s}$  by use of the equation for integrated intensity given previously. He showed that:

$$R_p = \frac{3}{8\pi} \frac{1}{(1-c)} \frac{\int sE(s) ds}{I(S_0)S_0^3}$$

Baur and Gerold<sup>58-59</sup> have shown that this reduces to

$$R_p = \frac{\langle a^3 \rangle}{\langle a^2 \rangle}$$

Recently, Harkness, Gould and Hren<sup>48-50</sup> have shown that the particle size distribution can be obtained from the experimentally determined values of the Guinier radius

and the Porod radius. Harkness et al.<sup>19</sup> determined that a log normal distribution could be used to represent the particle size distribution. A log normal function has the form:

$$F(X) = \frac{1}{\sqrt{2\pi} X \ln \sigma} \exp\left[-\frac{1}{2}\left(\frac{\ln \mu - \ln X}{\ln \sigma}\right)^2\right]$$

where:  $\mu$  is the geometric mean

$\sigma$  is the variance

Using the general moment equation for a log normal distribution function, the  $n^{\text{th}}$  moment is given by:

$$r^n = \exp\left[n \ln \mu + \frac{n^2}{2} \ln^2 \sigma\right]$$

Applying this relationship to the results of Baur and Gerold,<sup>58-59</sup> Harkness et al.<sup>49</sup> showed that

$$R_G = \left[\frac{\langle R^7 \rangle}{\langle R^5 \rangle}\right]^{1/2} = \exp[\ln \mu + 2.5 \ln^2 \sigma]$$

and

$$R_p = \left[\frac{\langle R^3 \rangle}{\langle R^2 \rangle}\right] = \exp[\ln \mu + 6 \ln^2 \sigma]$$

Solving these equations for  $\mu$  and  $\sigma$  yields:

$$\ln \mu = \ln R_G - 1.71 \ln \frac{R_G}{R_p}$$

$$\ln^2 \sigma = \frac{\ln\left(\frac{R_G}{R_p}\right)}{3.5}$$

Using these equations and the assumption of a log normal distribution, it is possible to plot the zone size distribution from the experimentally determined values for the Guinier radius and the Porod radius.

Harkness et al.<sup>49</sup> have also determined that  $N_V$ , or the number of zones per  $\text{cm}^3$ , can be determined using the zone size distribution and the volume fraction,  $V_f$ , of zones obtained from knowledge of the miscibility gap as follows:

$$\frac{4}{3}\pi \langle R^3 \rangle N_V = V_f$$

In this manner, it is possible to plot the actual number of particles within each zone size.

Changes in the volume fraction can be monitored as a function of changes in the integrated intensity. Gerold<sup>3</sup> has shown that the volume fraction of particles at any time,  $t$ , can be given as:

$$f(t) = \frac{Q_0(t)}{Q_0(\infty)} f(\infty)$$

where:  $f(t)$  is the volume fraction at time  $t$

$f(\infty)$  is the volume fraction of the fully aged sample as determined from the phase diagram

$Q_0(t)$  is the integrated intensity at time  $t$

$Q_0(\infty)$  is the integrated intensity of the fully aged alloy

Using this relationship, the volume fraction of particles can be accurately determined throughout the aging sequence, and, therefore, accurate particle size distributions can be determined.

### CHAPTER III

#### EXPERIMENTAL EQUIPMENT AND PROCEDURES

##### The Alloy

The 7075 commercial aluminum alloy was supplied as 3/4 inch alclad plate from the Reynolds Aluminum Company. The alloy was analyzed spectrographically by two x-ray methods. First, it was analyzed using an x-ray energy dispersive system at Oak Ridge National Laboratories, and secondly, it was analyzed using a Norelco\* crystal dispersive x-ray spectrometer. The averaged results of these tests showed the composition to be:

Zn-5.80 wt %	Cr-.22 wt %
Mg-2.62 wt %	Si-.19 wt %
Cu-1.74 wt %	Ti-.04 wt %
Fe-0.27 wt %	Al-balance

##### Small Angle Scattering and Tensile Test Sample Preparation

The plate was prepared for rolling by milling 1/16 inch off of each face in order to remove both the alclad layer, as well as any effects of it in the 7075 substrate. The plate was then cold-rolled on a Fenn<sup>†</sup> rolling mill,

\*Philips Electronic Instruments, Mount Vernon, New York

†Fenn Manufacturing Company, Newington, Connecticut

with intermediate anneals of 30 minutes at 460°C to thicknesses of .85 mm, .80 mm and .72 mm. These thicknesses produced a constant .72 mm thickness for all samples when the final mechanical treatments of 15%, 10% and 0% were later applied. This large reduction with intermediate anneals was sufficient to break up any large precipitates present in the as-received condition.

Specimens for the tensile tests were prepared in the same manner, with the gage section being cut on a Tensile-Kut\* high speed milling machine, according to ASTM Specification A370 (substandard size) subsequent to aging.

#### Resistometry Sample Preparation

Resistometry samples were prepared by first turning 1/2 inch rods from the 3/4 inch plate. This rod was swaged on a Fenn swaging machine, with intermediate anneals at 460°C for 30 minutes, down to .106 inches diameter. This thin rod was then drawn using a wire drawer down to .02 inches. Intermediate anneals at 460°C for 30 minutes were necessary after each draw; however, annealing left the wire too soft to draw. Thus, it was necessary to slightly age-harden the alloy by heating for 10 minutes at 135°C after annealing in order to develop sufficient

---

\*Sieburg Industries, Danbury, Connecticut

strength. The wire was then made into a coil and voltage leads were spot welded onto it.

#### Solution Heat Treating and Aging

The small angle scattering and tensile specimens were solution heat treated at  $460^{\circ}\text{C} \pm 3^{\circ}\text{C}$  for 2 hours in a vertical tube furnace equipped with a large Inconel block for temperature stability. Quenching was accomplished by drop-quenching the specimens and holding the rod into an ice water bath ( $1/2^{\circ}\text{C}$ ). The solutionized samples were stored in liquid nitrogen prior to elevated temperature aging.

The resistometry specimens were solutionized in a forced air furnace for 2 hours at  $460^{\circ}\text{C}$  and were quenched by dropping into an ice water bath. The wires were mounted onto a phenolic board immediately after quenching and were then promptly aged.

All elevated temperature aging was conducted in a Lauda\* constant temperature oil bath, capable of maintaining a given temperature within  $\pm 1^{\circ}\text{C}$ , containing 50 cs Dow Corning<sup>†</sup> silicon oil. After aging, and prior to testing, the samples were stored in a refrigerator ( $\sim 4^{\circ}\text{C}$ ).

\*Brinkman Instruments, Westbury, New York

†Dow Corning Corporation, Midland, Michigan

Retesting of specimens, even after long periods of storage in the refrigerator, indicated that no measurable change in the zone state had occurred, provided some elevated temperature aging had been performed.

#### Wide Angle Diffraction

Small strips, approximately  $1/8$  inch x  $5/8$  inch x .72 mm, were cut from the small angle scattering samples to be used as samples for wide angle diffraction. The wide angle diffraction was done using an Enraf-Nonius,\* Guinier-De Wolff camera. The essentials of this camera are shown in Figure 5. This camera is equipped with an incident beam, elastically curved, quartz monochromating crystal, which focusses the primary and diffracted beams onto the diffraction circle (i.e., the film). All exposures were run at room temperature with the chamber evacuated to eliminate air scatter. The use of monochromatic radiation and an evacuated path eliminates fogging of the film and allows long time exposures to be run. The lower limit of detection with this method is on the order of .05 to .10% of a second phase. This technique was used to determine any quenched-in precipitates and also to follow the sequence of precipitation. Four samples can be run

\*Enraf-Nonius, Inc., Garden City Park, New York



# GUINIER DeWOLFF CAMERA

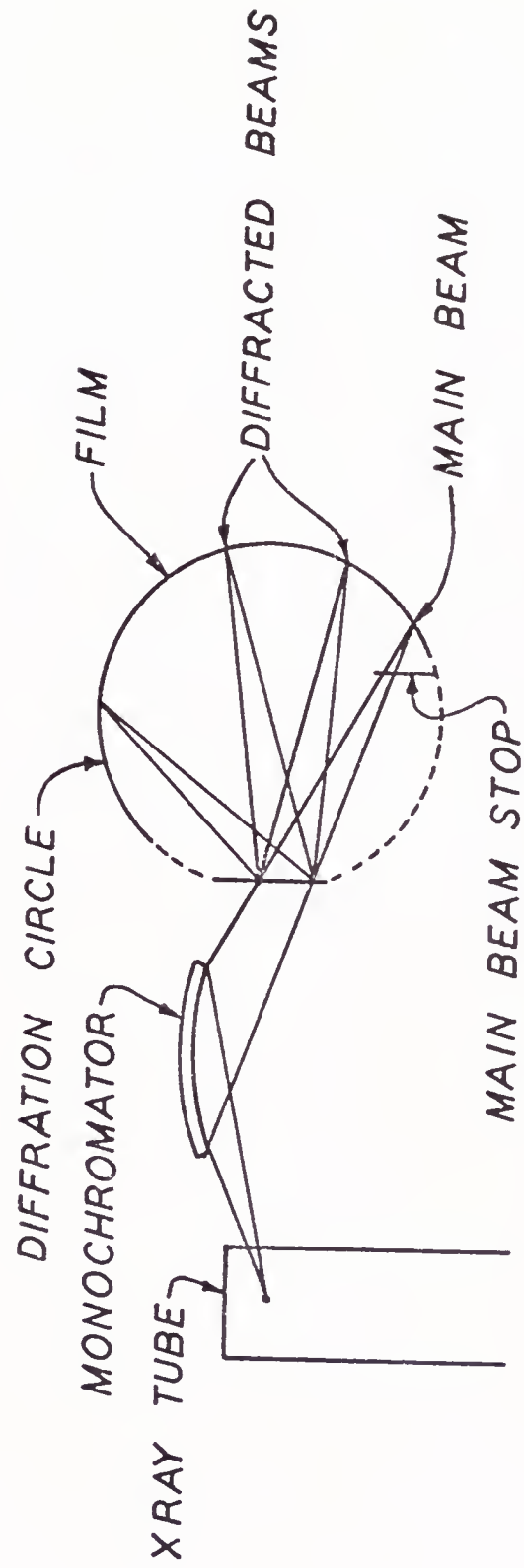


Figure 5. Schematic Representation of Guinier De Wolff Camera

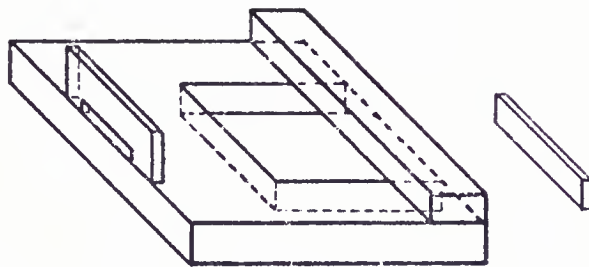
simultaneously in a Guinier-De Wolff camera. All exposures were run for 48 hours, with machine settings of 45 KV-20 ma. The films were densitometered after development in order to determine intensities of the weak precipitate diffraction lines.

#### Small Angle X-Ray Scattering

The small angle scattering experiments were conducted using a Siemen's\* Kratky small angle camera. Figure 6 shows a schematic of the essentials of this type of camera. Small angle scattering cannot be observed using standard x-ray diffraction equipment due to the divergence of the primary beam; thus, the need for such a system. Figure 7 is a diagram of the collimation system for the Kratky camera. The first slit, or entrance slit, restricts the height of the primary beam. The next set of slits, in the Kratky block, restrict the divergence of the primary beam to include only parallel, or nearly so, rays in the incident beam. These two slit systems greatly reduce the intensity of the primary beam by severely limiting the solid angle of the x-ray beam front observed, but, when aligned, are capable of producing a flat, parallel beam of uniform intensity. The condition of uniform in-

\*Eastern Scientific Sales Co., Marlton, New Jersey





*KRATKY BLOCK*

Figure 7. Schematic of Slits System in Kratky Block

tensity and "infinite" slit width<sup>61</sup> is necessary in order to satisfy the conditions of the Porod equation. For the Kratky camera, the condition of infinite width is expressed as:

$$l \leq 2m + \sigma$$

where:  $m$  is the height of observation above main beam

$\sigma$  is the width of the primary beam at the exit slit

$l$  is the length of the primary beam that is of uniform intensity

A uniform intensity beam of 3.5 cm was obtained on alignment of the Kratky camera, while the rear slits were set at 1 cm.

A graphite crystal diffracted beam monochromator was used in order to measure only monochromatic radiation, and pulse height selection was employed to eliminate any harmonic diffraction which might occur.

Table 2 gives the operating machine parameters used in this investigation. Plateau voltage curves were run on the detector in conjunction with varying gain settings in order to determine the peak operating voltage of the detector. The pulse height selector settings were set exactly at the base of the  $\text{MoK}\alpha$  energy peak.

Table 2  
Machine Parameters

## SLIT SIZES

Front Entrance - 100  $\mu$   
Rear Exit - 200  $\mu$  x 1 cm

SPECIMEN TO DETECTOR DISTANCE - 215 mm

OPERATING CONDITIONS - 45 KV  
20 ma

RADIATION - MoK $\alpha$   $\lambda$  = .71  $\text{\AA}$

DETECTOR VOLTAGE - 1100 V (Bicron\* scintillation)

## PULSE HEIGHT SELECTOR

Lower Limit - 2.0 volts  
Upper Limit - 4.0 volts

STEP SIZE - 100 $\mu$

\*Bicron Corporation, Newbury, Ohio

All samples were step scanned using an Ortec\* Model 6713 axis controller and Ortec counting equipment. Scans began from a height of approximately 300  $\mu$  above the centroid of the primary beam to about 10,000  $\mu$  above the main beam. Collection time was 1,000 seconds or at least 12,000 counts at each of the 100  $\mu$  steps. All scans were run with the Kratky block, specimen holder and tank evacuated in order to reduce air scatter.

\*Ortec, Inc., Oak Ridge, Tennessee

A sample of Lockheed pyrolytic graphite<sup>62</sup> was used both as a test of proper camera alignment and as a scattering standard to correct for variations in primary beam intensity between runs. Figure 8a shows the scattering curve of the graphite, while 8b shows the Porod region, where a slope of -3 indicates proper camera alignment.

All intensity corrections were made with the graphite standard. Main beam intensity variations were corrected for by ratioing the intensity of the graphite scattered at a fixed position before each run to that of the graphite scatterer measured before the pure aluminum run. Variations in sample absorption were corrected for by measuring the intensity of the graphite standard with the pure aluminum in the absorption position and ratioing it to that of the graphite standard with the aluminum alloy sample in the absorption position. The total corrected intensity for a sample is given by:

$$I_{\text{corr}} = I_{\text{meas}} \frac{I_{\text{g}}^{\text{std}}}{I_{\text{g}}^{\text{sam}}} \frac{A_{\text{abs}}^{\text{pure}}}{A_{\text{abs}}^{\text{sam}}}$$

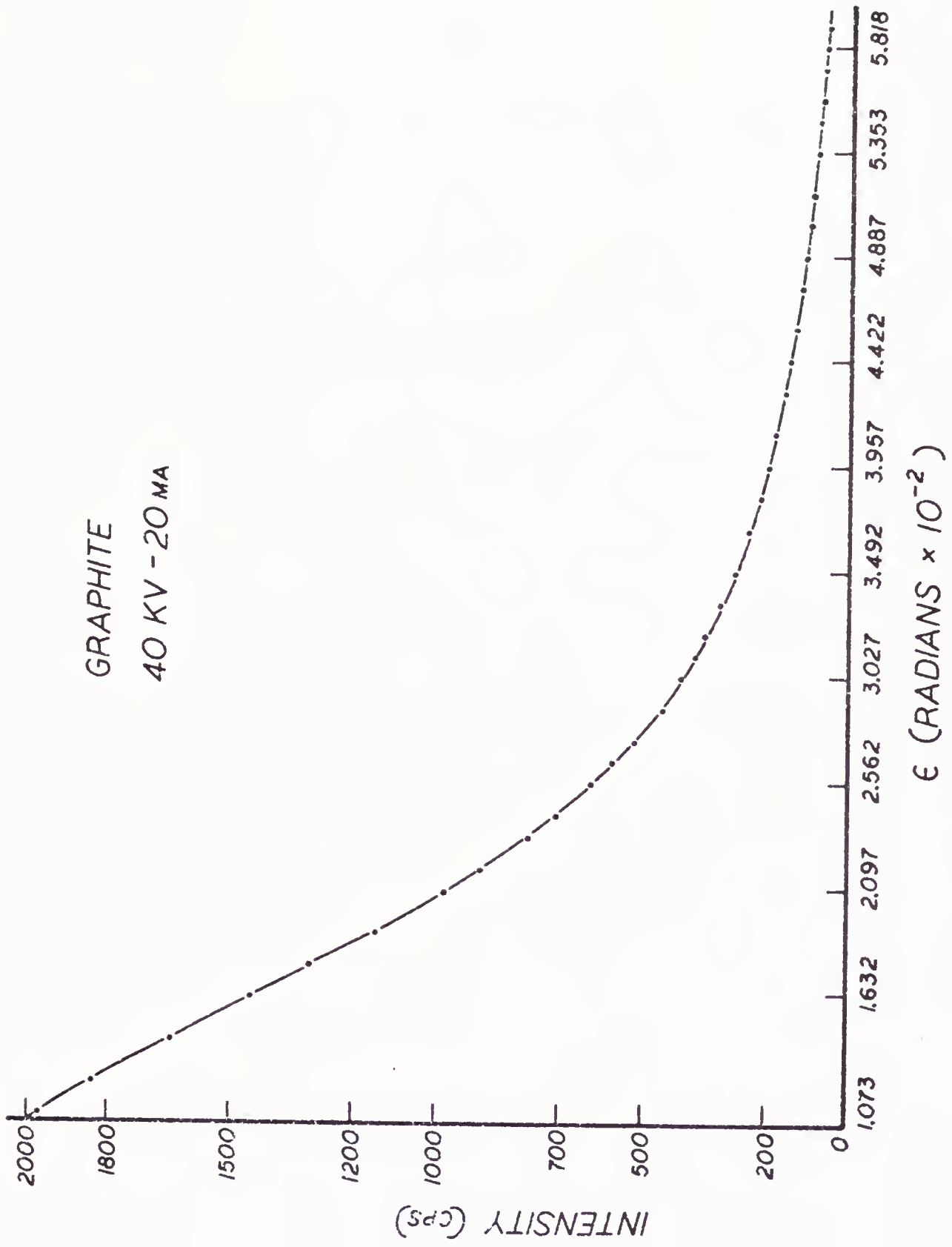
where:  $I_{\text{corr}}$  is the corrected intensity

$I_{\text{meas}}$  is the measured intensity

$I_{\text{g}}^{\text{sam}}$  is the graphite intensity measured prior to each run

Figure 8a. Scattering Curve for Lockheed Pyrolitic Graphite





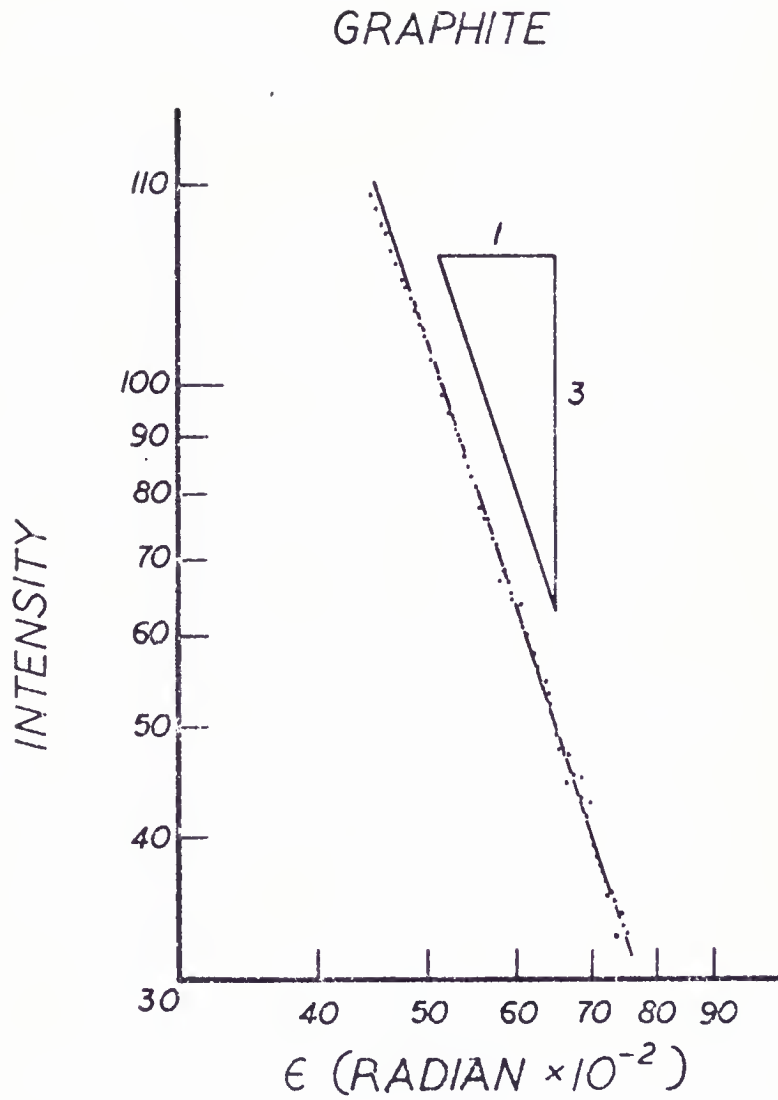


Figure 8b. Porod Region of Lockheed Pyrolytic Graphite Scatterer

$I_g^{std}$  is the graphite intensity measured prior to the pure aluminum run

$A_{abs}^{pure}$  is the absorption factor of the pure aluminum

$A_{abs}^{sam}$  is the absorption factor of the sample

The sample scattering curves were corrected for background by subtracting the intensity scattered from a 99.999% pure aluminum sample with the proper correction factors described above applied. All data was plotted and smoothed by hand before evaluation by a computer program written by Gould and Kirklin,<sup>63</sup> and modified by Healey and Hill<sup>64</sup> for this work. This program corrects for primary beam intensity variation due to sample thickness and tube fluctuations automatically, and calculates the Guinier Radius, Porod Radius, integrated intensity and the particle size distribution, based upon the method of Harkness, Gould and Hren.<sup>48-50</sup>

#### Resistometry Measurements

Resistometry measurements were made using a Leeds and Northrup\* Kelvin bridge-type potentiometer, standardized against a .001 ohm standard resistor.<sup>65</sup> Measurements were made at liquid nitrogen temperature. It was not possible

\*Leeds and Northrup Company, Philadelphia, Pennsylvania

to measure true resistivity ( $\rho$ ) of the sample as the exact length between the voltage leads was not known. Instead, the resistance, or actually the voltage between the two welded leads with an exact current of 1 amp, was measured. This was plotted as  $\frac{R-R_0}{R_0}$ , where  $R_0$  was the resistance measured immediately after quenching.

### Tensile Testing

Tensile tests were performed on the specimens cut to ASTM Specification A370 (substandard size) on an Instron\* testing machine. All tests were run at a strain rate of .02 inches per minute.

---

\*Instron Corporation, Canton, Massachusetts

## CHAPTER IV

### EXPERIMENTAL RESULTS

All data presented here has been obtained from commercial 7075 alloy, whose chemical composition is presented elsewhere. A series of isothermal aging treatments, with and without deformation, were performed on the samples. The term preaging, as used here, will include any thermal treatment given to a series of samples prior to the final thermal aging treatment. Table 3 presents all treatments performed on the various series and their designations.

#### Resistivity

The resistivity-aging time curves for the wire specimens are given in Figure 9. This resistivity data is summarized in Figure 10 as an Arrhenius plot.<sup>33</sup> The physical significance of this plot lies in the slope of the line having the units of energy, and corresponding to  $E_m$ , the activation energy of motion.

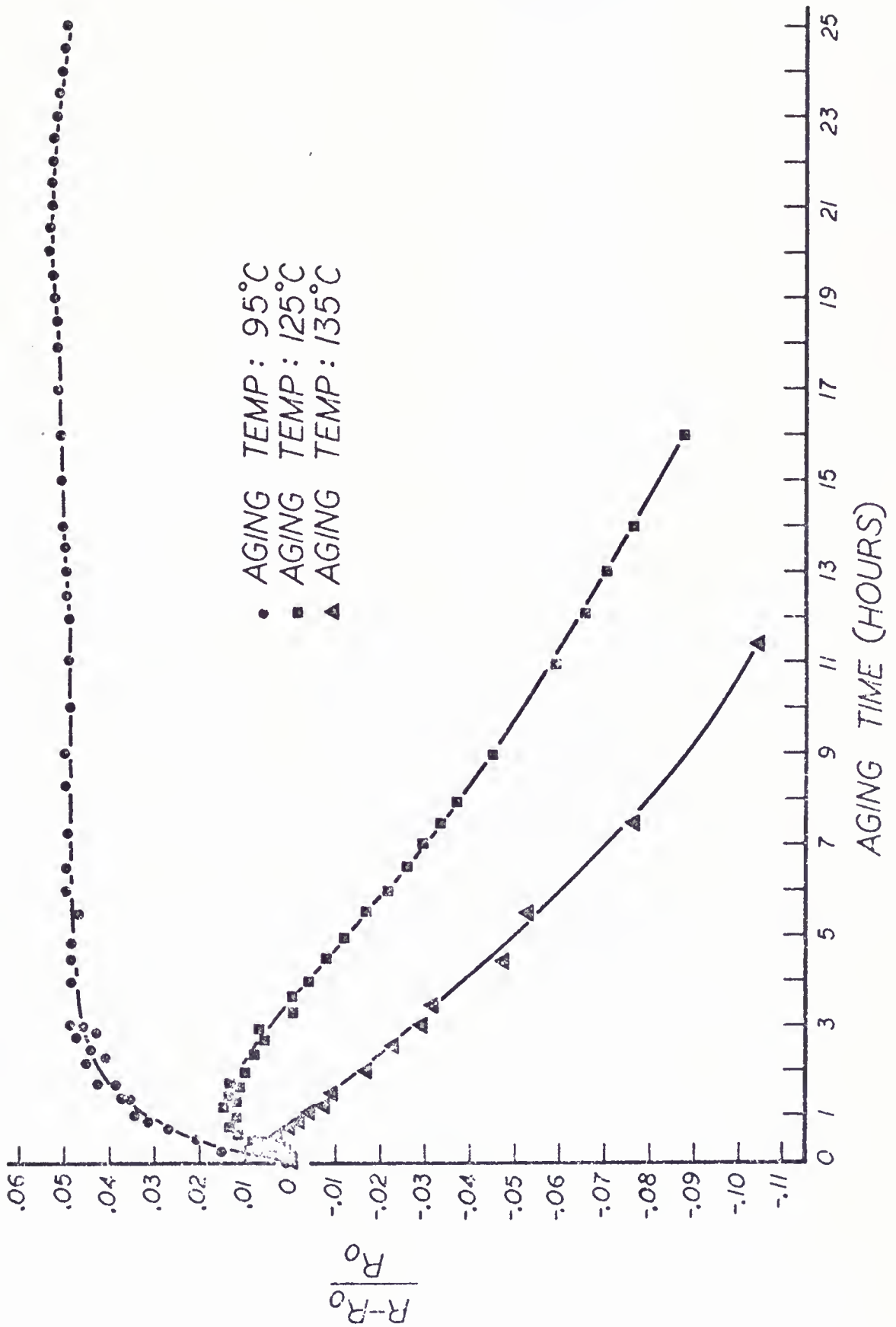


Figure 9. Resistivity Aging Behavior of 7075 Wires

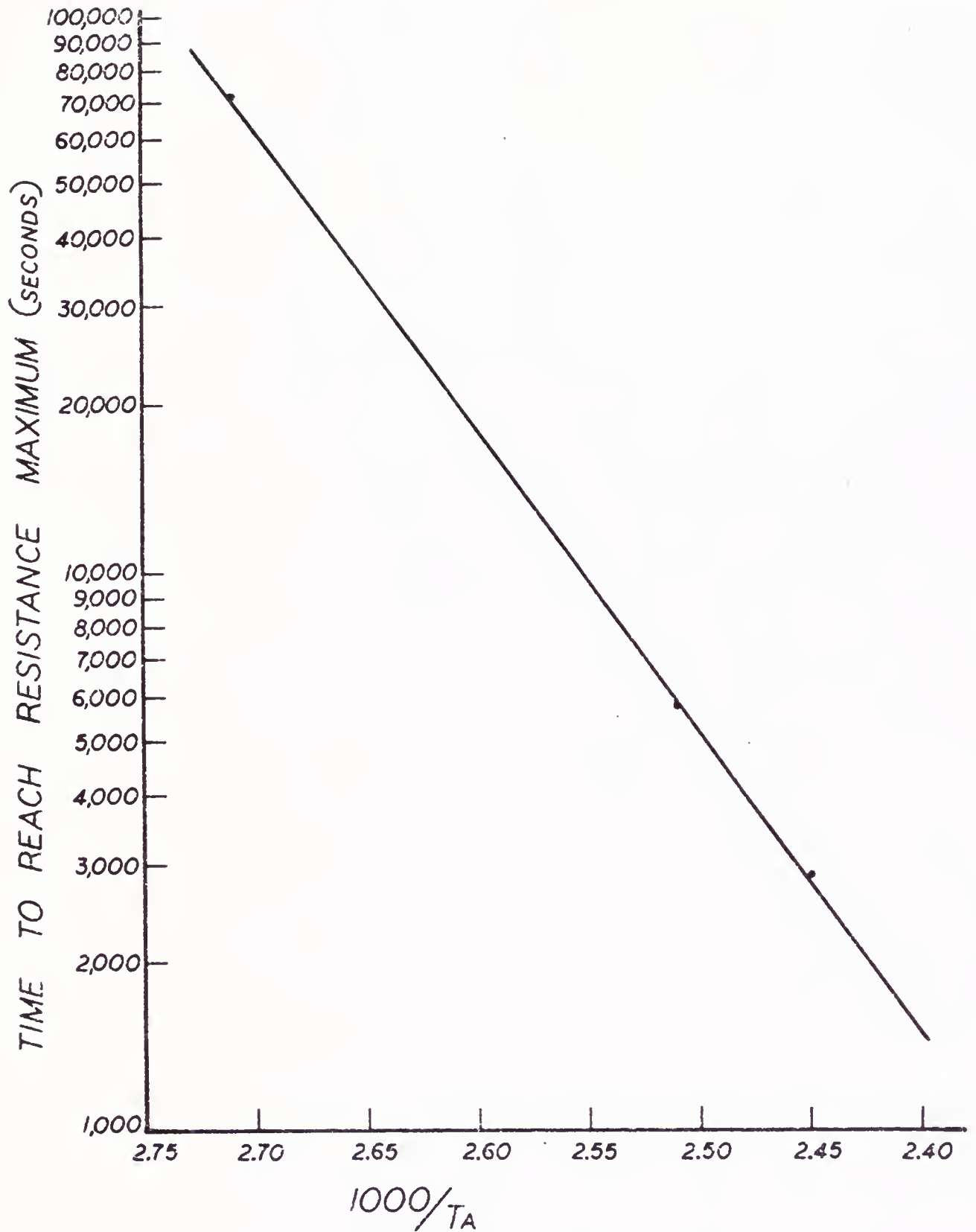


Figure 10. Arrhenius Plot of Resistivity Maxima

Table 3  
Summary of Aging Series

Series	Defm	Preage Treatment	Aging Temperature
A	0	NONE	135°C
B	5%	NONE	135°C
D	15%	NONE	135°C
E	0	NONE	125°C
F	15%	NONE	125°C
FlH	15%	1 hour 125°C	125°C
G	0	NONE	75°C
H	15%	NONE	75°C
J	0	100 hours 75°C	125°C
K	0	25 hours 75°C	125°C
L	0	100 hours 95°C	155°C
M	0	25 hours 95°C 5 hours 125°C	155°C

### Small Angle X-Ray Scattering

#### Preliminary Studies of Initial Aging

A similar study to that of resistivity was performed using small angle scattering. A single sample was isothermally aged at three temperatures (135°C, 145°C and 165°C) with homogenization at 460°C for two hours between temperatures, and the scattered intensity was measured at



0.011 radians as a function of aging time. Figure 11 shows the scattering curves obtained, while Figure 12 is an Arrhenius plot of the log of the time to reach a scattering intensity of 1.5 counts per second versus  $1000/T_a$ , where  $T_a$  is the isothermal aging temperature.<sup>40</sup>

A preliminary study of the effects of deformation on the initial aging rate was performed in a similar manner. The scattering intensity at 0.011 radians is plotted versus aging time for the A, B and D series, see Figure 13.

#### Change in Zone Size Parameter

Entire scattering curves are necessary to determine the two size parameters; the Guinier Radius,  $R_G$ ; and, the Porod Radius,  $R_p$ . Figures 14 and 15 show two such scattering curves, one representative of a direct-aged sample (Figure 14) and the other a sample that had been preaged before the final aging treatment (Figure 15). Corrections for sample variation were performed according to the procedure presented in Chapter III. The results of the evolution of the Guinier Radius are given in Figures 16 through 21. Evaluation of the Guinier Radius in the unaged or very short direct aged samples was difficult due to the low scattering intensity. For the low temperature aging series (G and H), this problem was encountered throughout the aging sequence as the growth was extremely slow.

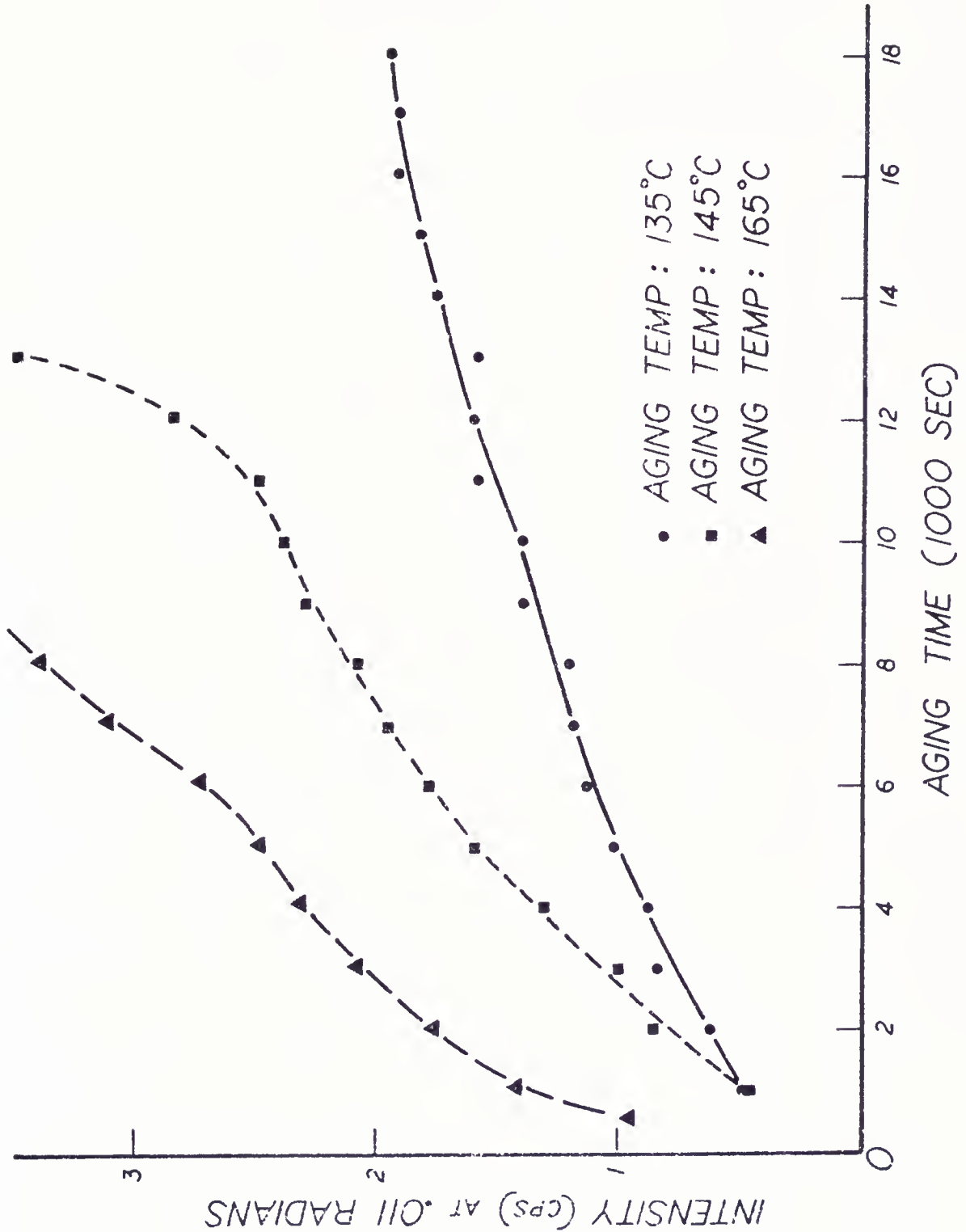


Figure 11. Fixed Angle Scattered Intensity for 7075 Alloy

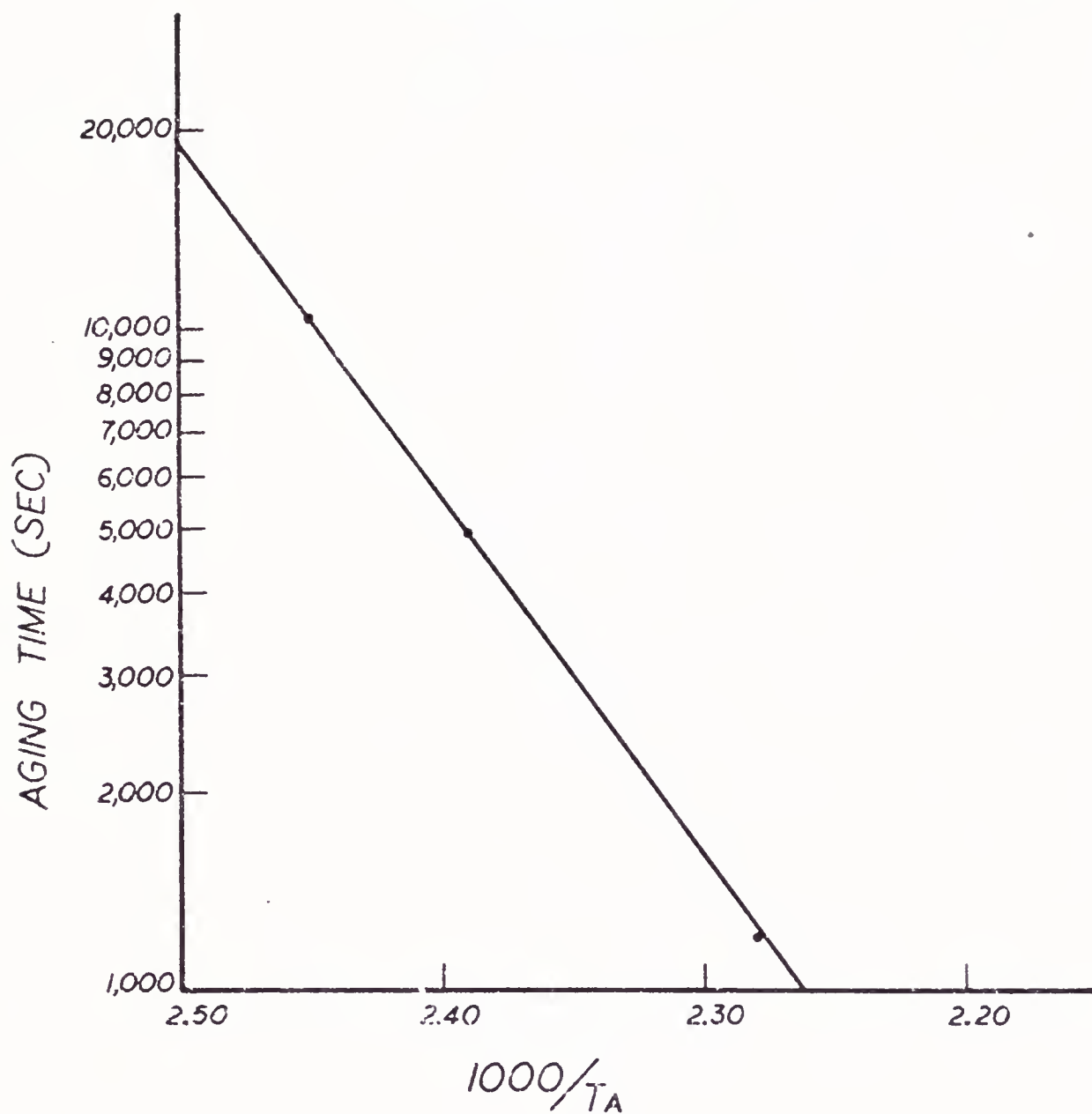


Figure 12. Arrhenius Plot of Time to Reach Scattered Intensity of 1.5 Counts Per Second

Figure 13. Preliminary Study of Effect of Deformation-Fixed Angle Scattered Intensity

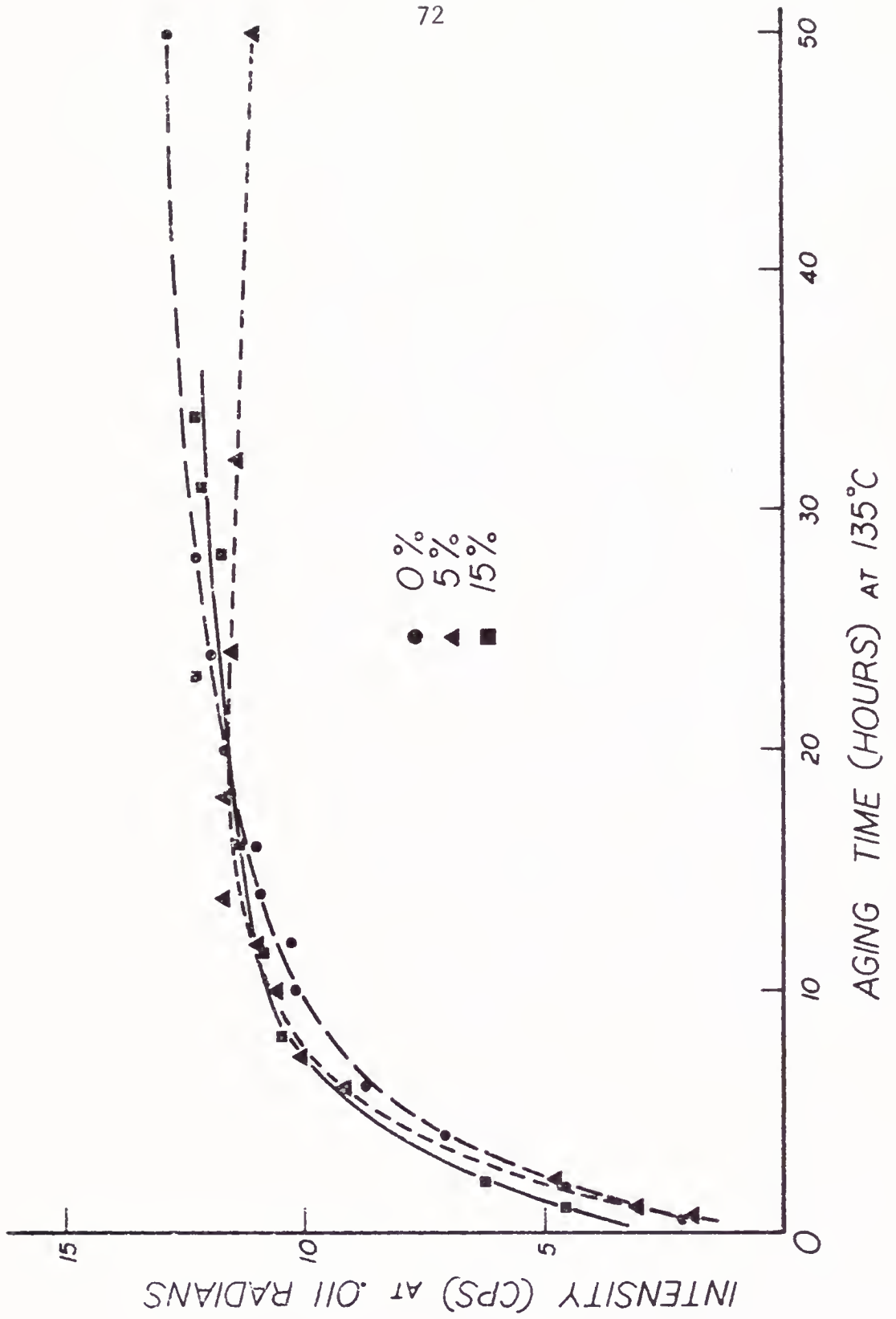


Figure 14. Typical Small Angle Scattering Curve of Directly Aged Sample

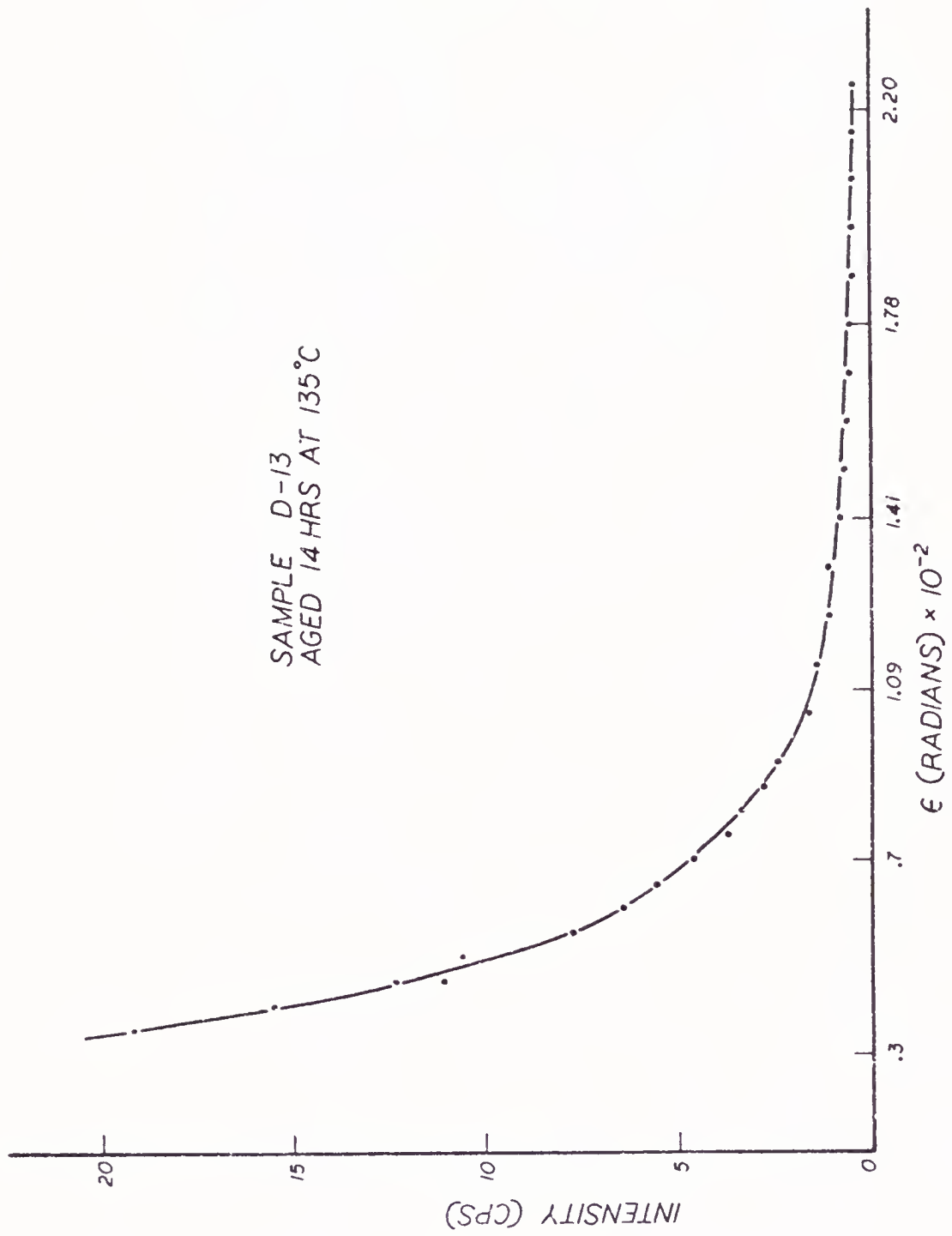
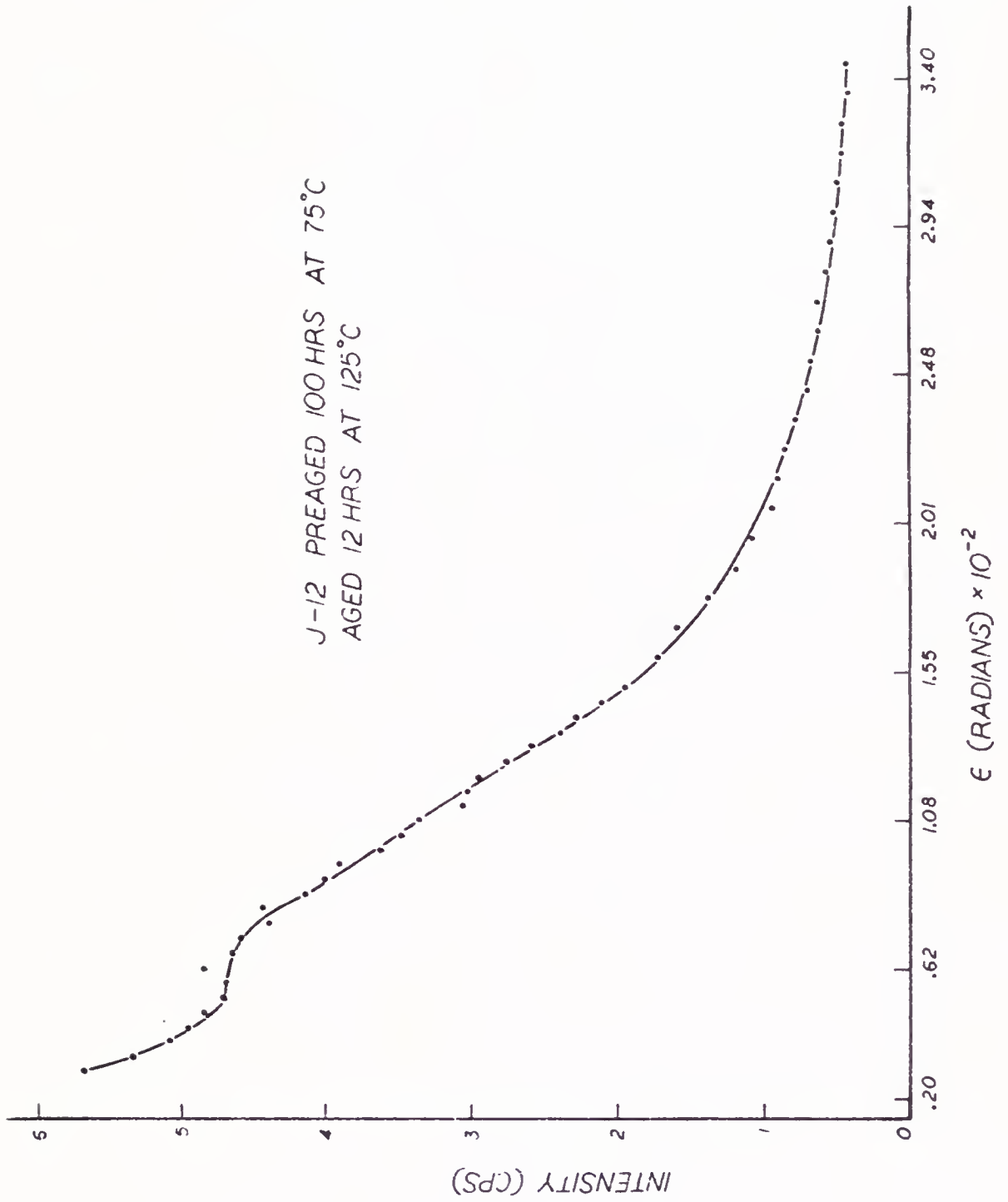
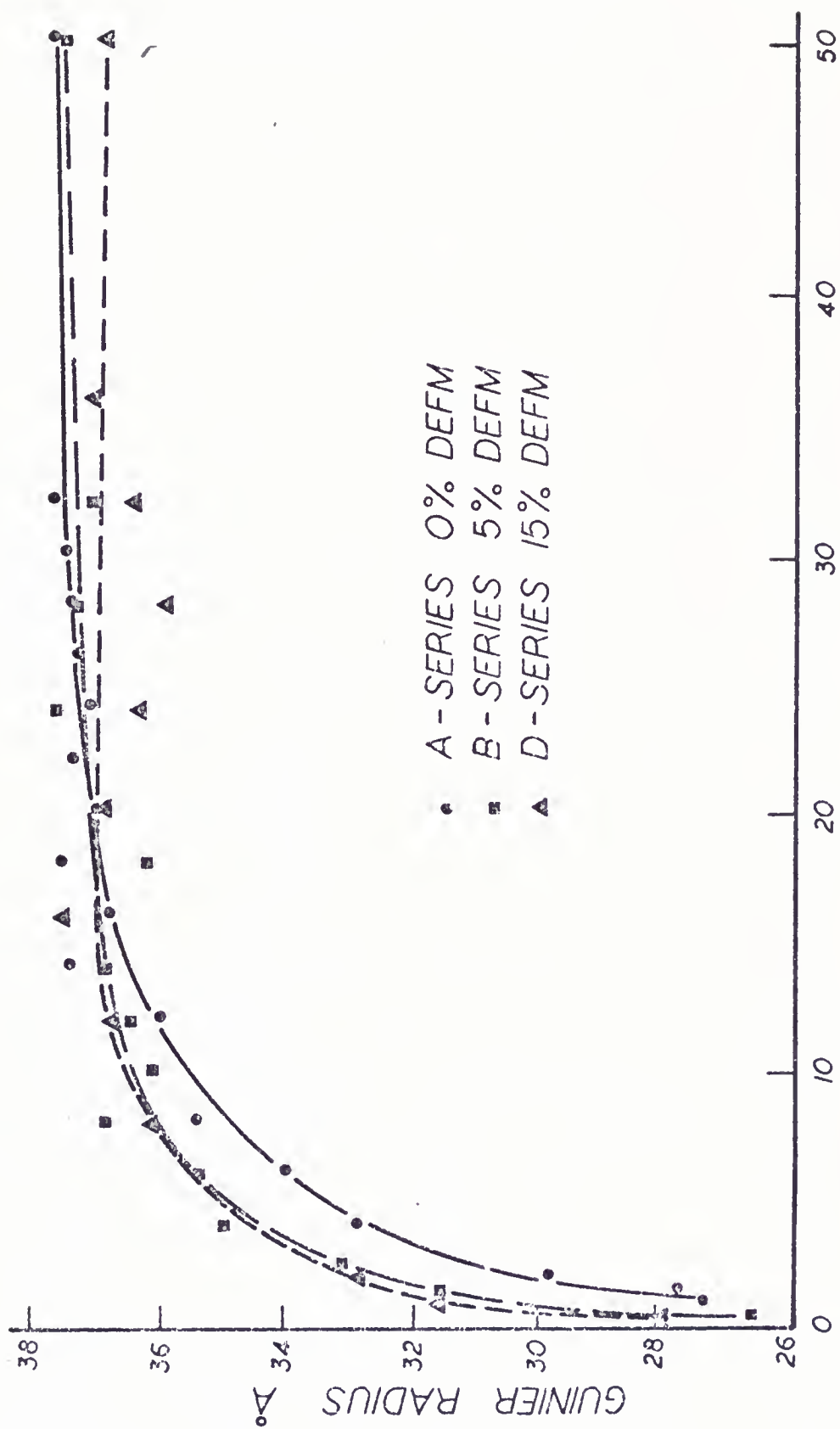


Figure 15. Typical Small Angle Scattering Curve from a Preaged Sample







AGING TIME (HOURS) AT 135°C

Figure 16. Evolution of Guinier Radius as Determined from SAXS for A, B, D Series

Figure 17. Evolution of Guinier Radius as Determined from SAXS for E, F, FLH Series

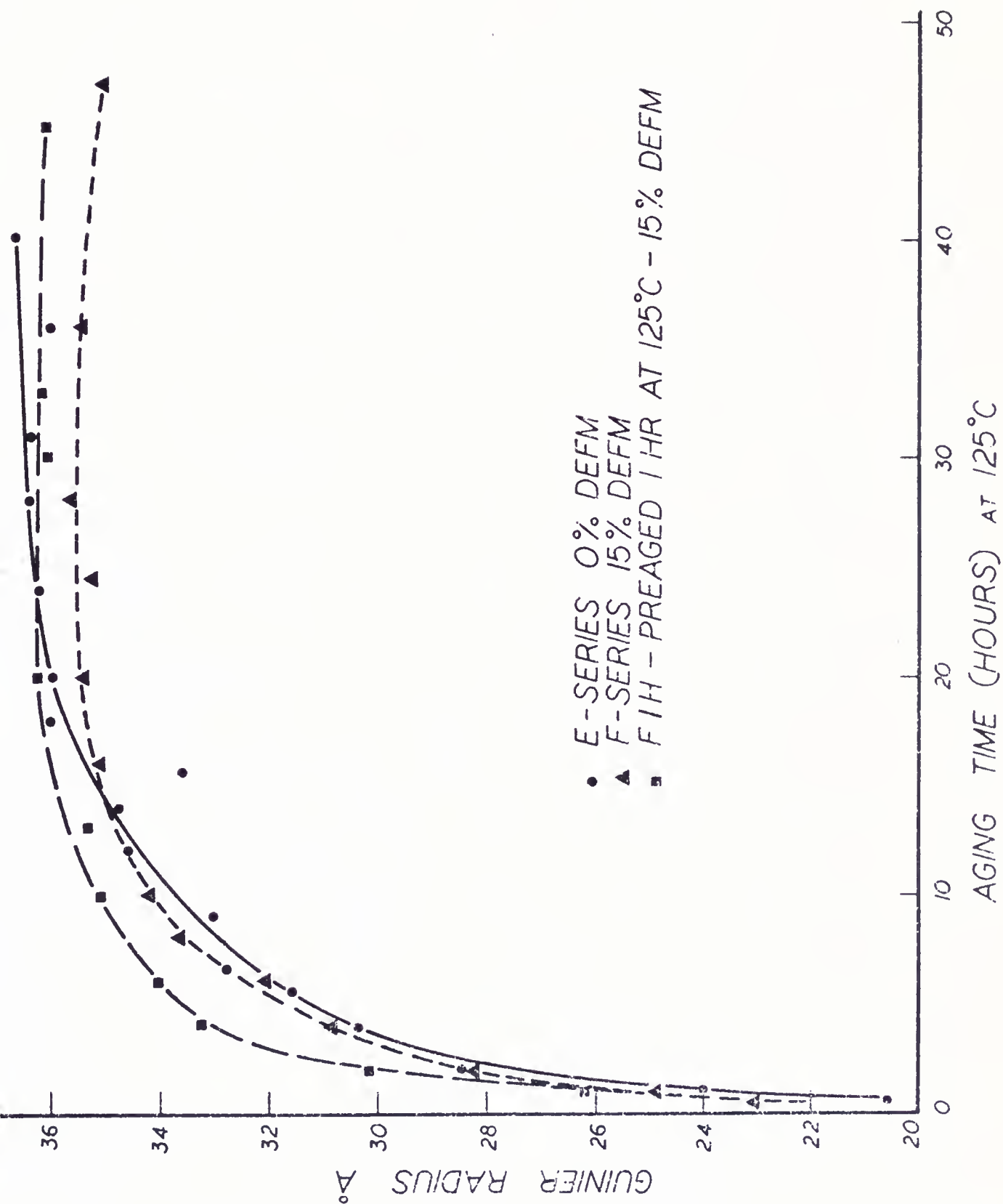


Figure 18. Evolution of Guinier Radius as Determined by SAXS for G and H Series

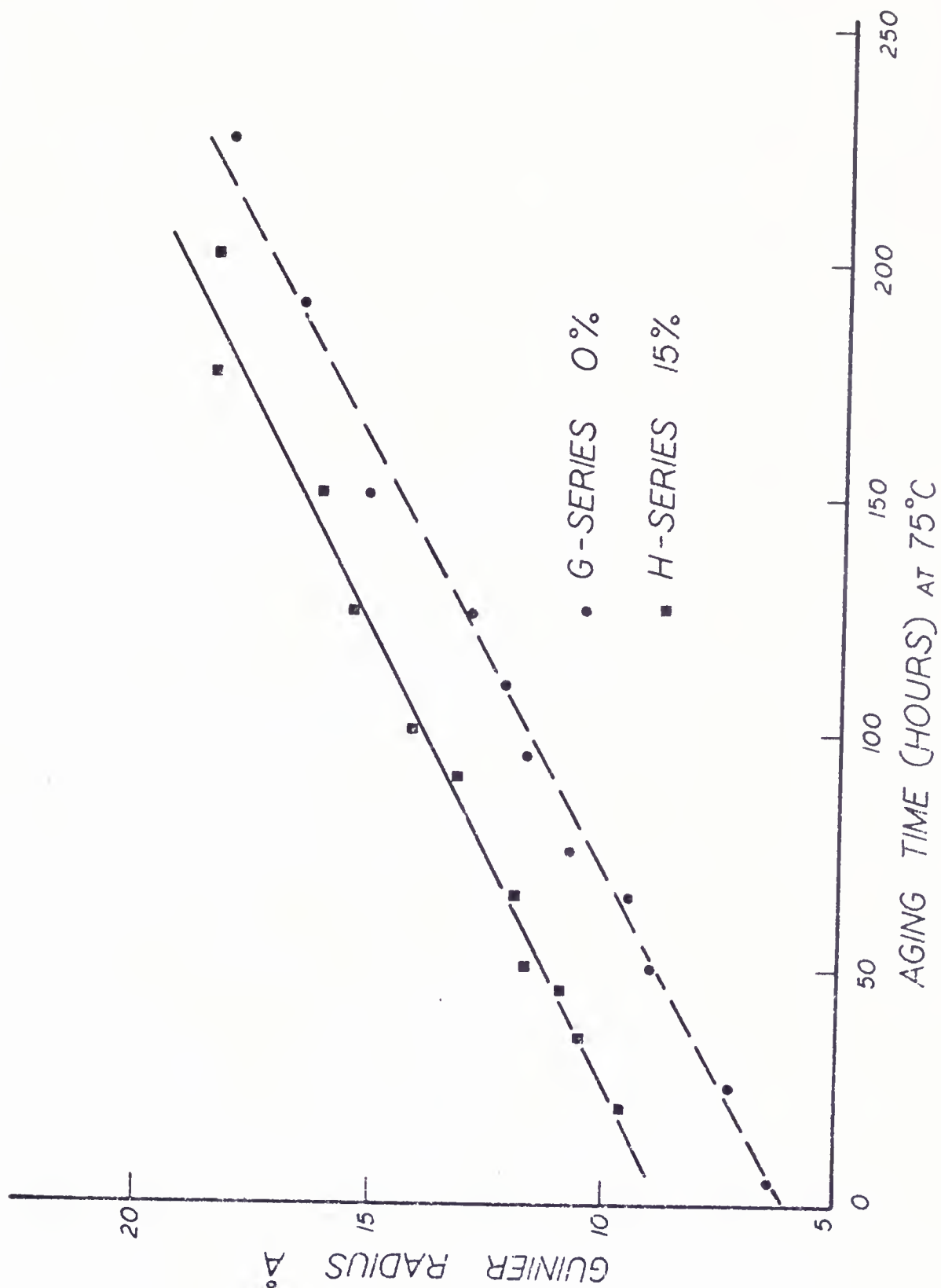
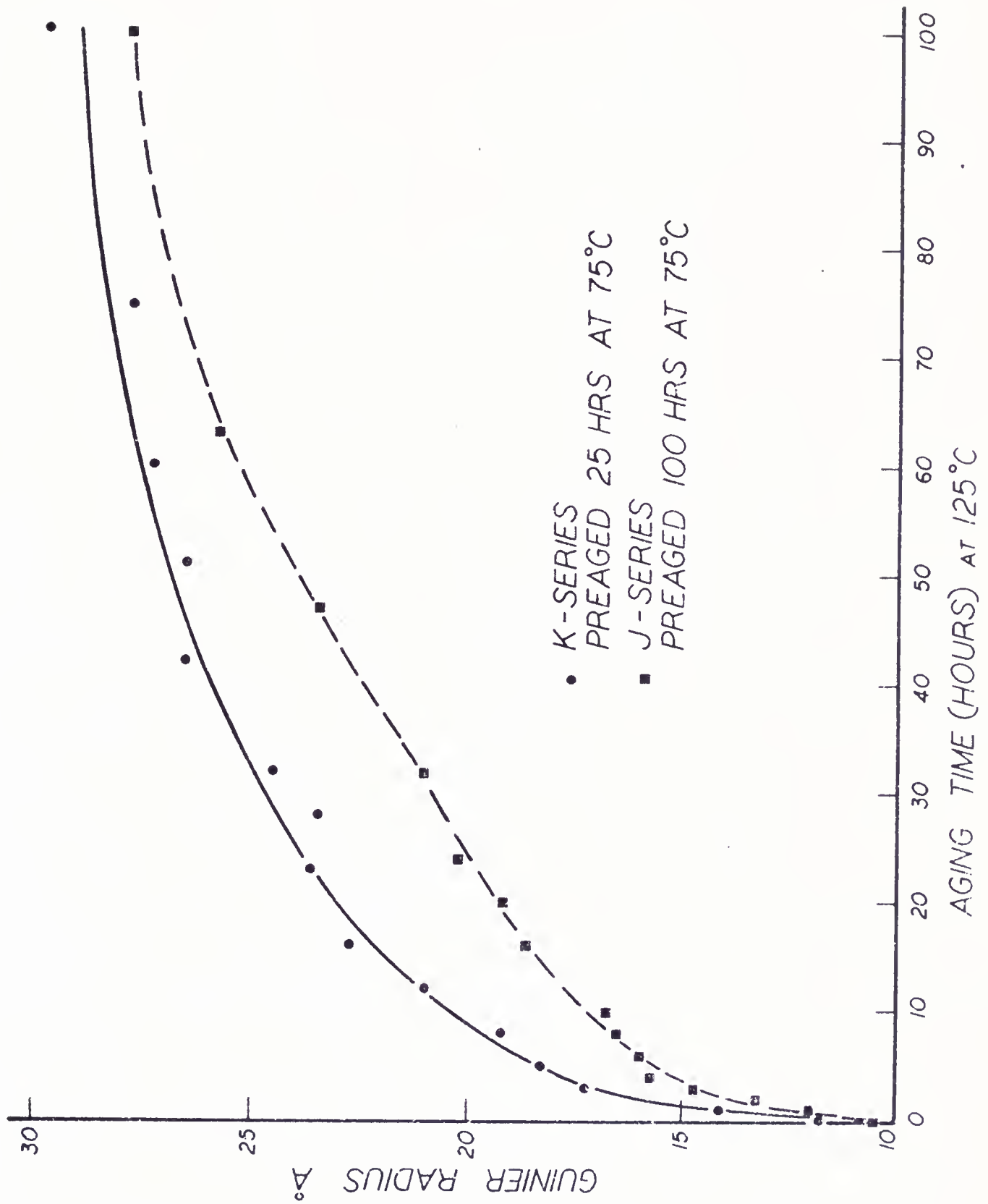


Figure 19. Evolution of the Guinier Radius as Determined by SAXS for J and K Series





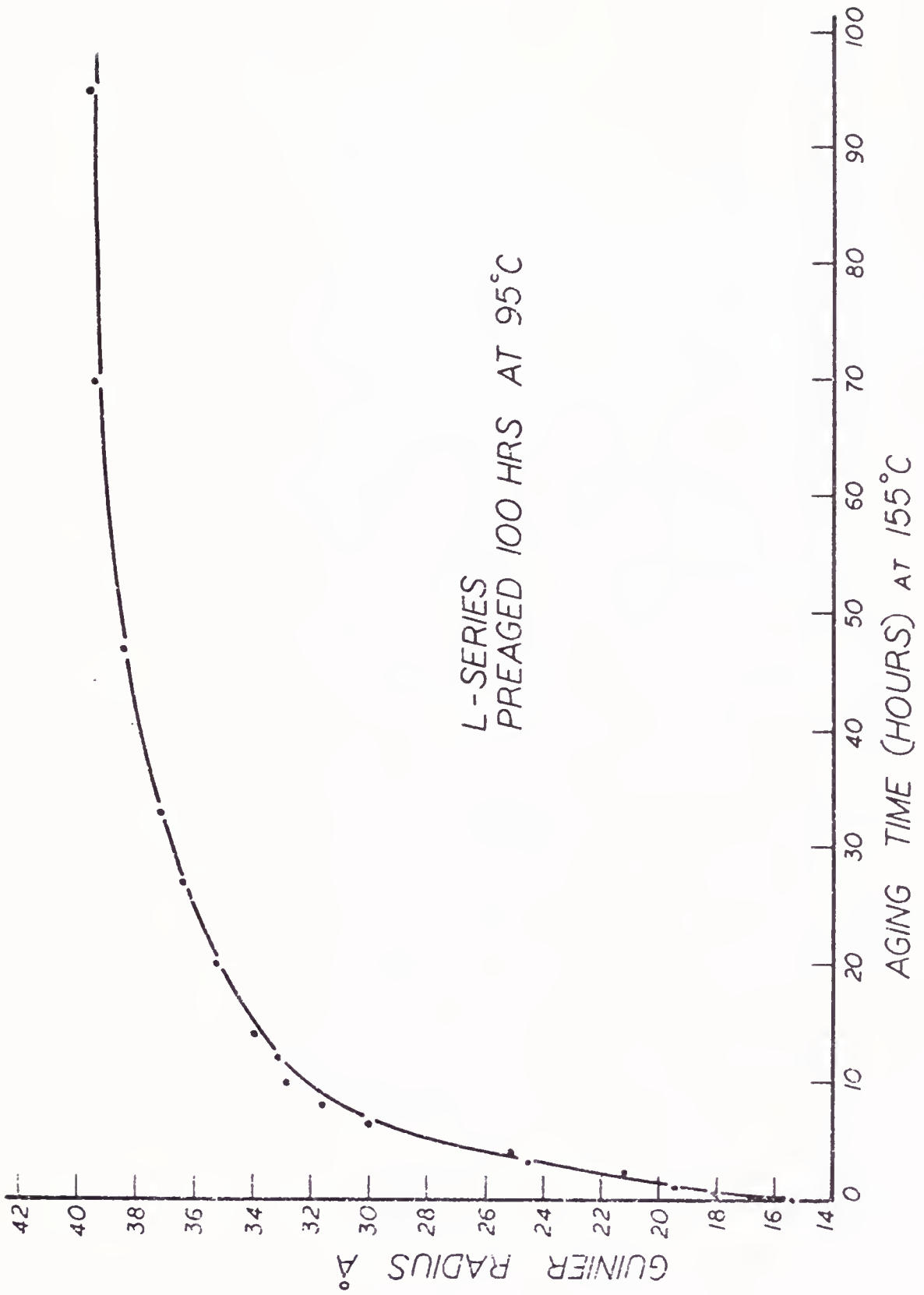
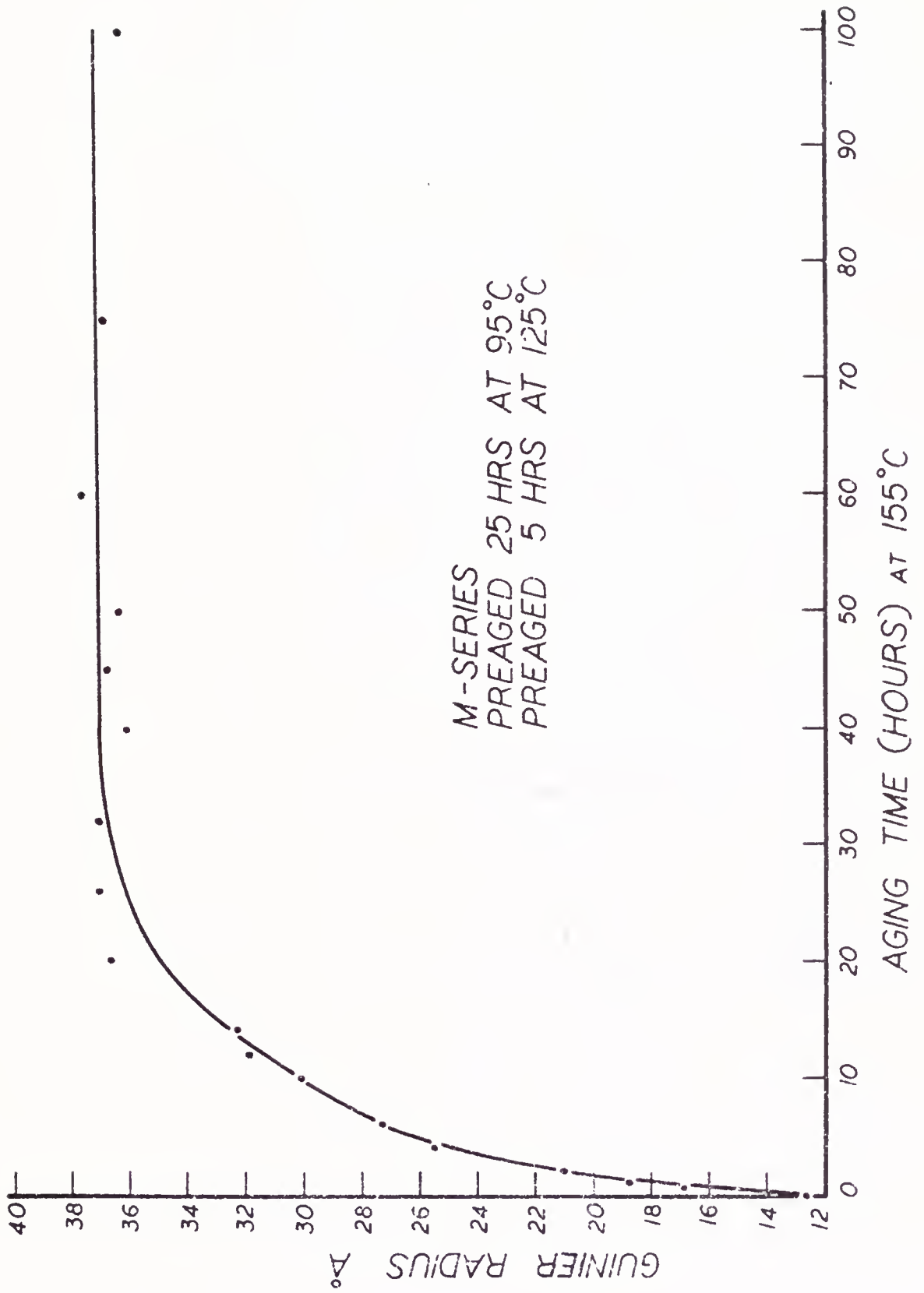


Figure 20. Evolution of Guinier Radius as Determined by SAXS for L Series

Figure 21. Evolution of Guinier Radius as Determined by SAXS for M Series



The results for the Porod radius are presented in Figures 22 through 26. It was not possible to obtain a meaningful Porod radius for the very short aging time samples as the Porod region was either at too high an angle, or buried within the background. Also, it was not possible to obtain a Porod radius with physical significance for the G and H series as the Porod region was beyond the workable angular range of the Kratky camera.

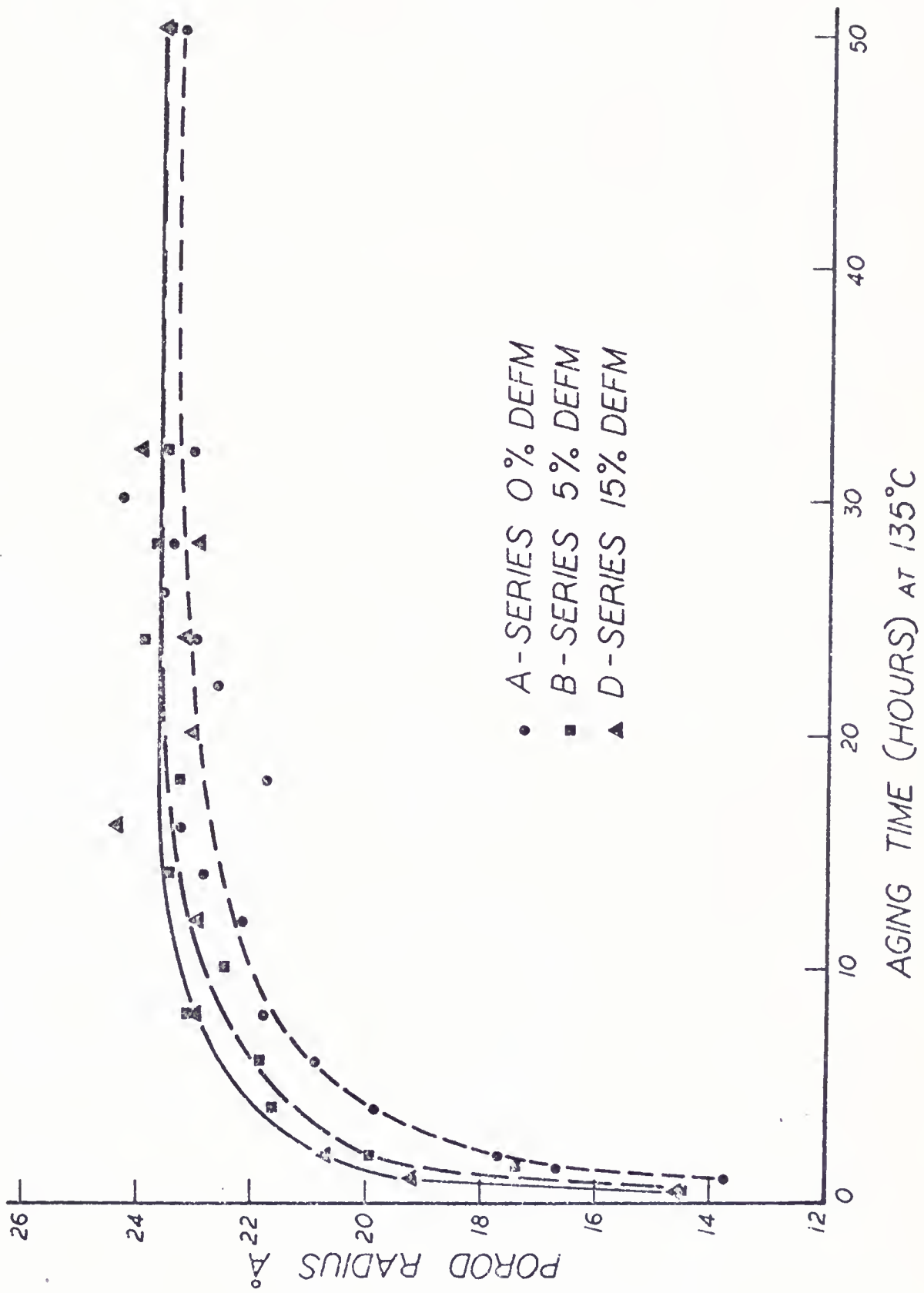
The radius of maximum abundance values are plotted in Figures 27 through 32. These determinations assume a log normal distribution.

It was not possible to obtain a radius of maximum abundance for samples for which no Porod radius could be calculated. The Porod radius is necessary for this determination as described in Chapter II.

Frequency distribution plots of the particle radii as a function of aging time are presented in Figures 33 through 41. These distributions were generated assuming a log normal distribution, and spherical particles, and again were generated only for samples for which it was possible to obtain both a Guinier and Porod radius.

All of the above parameters were calculated using the modified computer program of Gould and Kirklin<sup>63-64</sup> which is described in the Appendix.

Figure 22. Porod Radius Evolution for A, B, D Series as Determined by SAXS



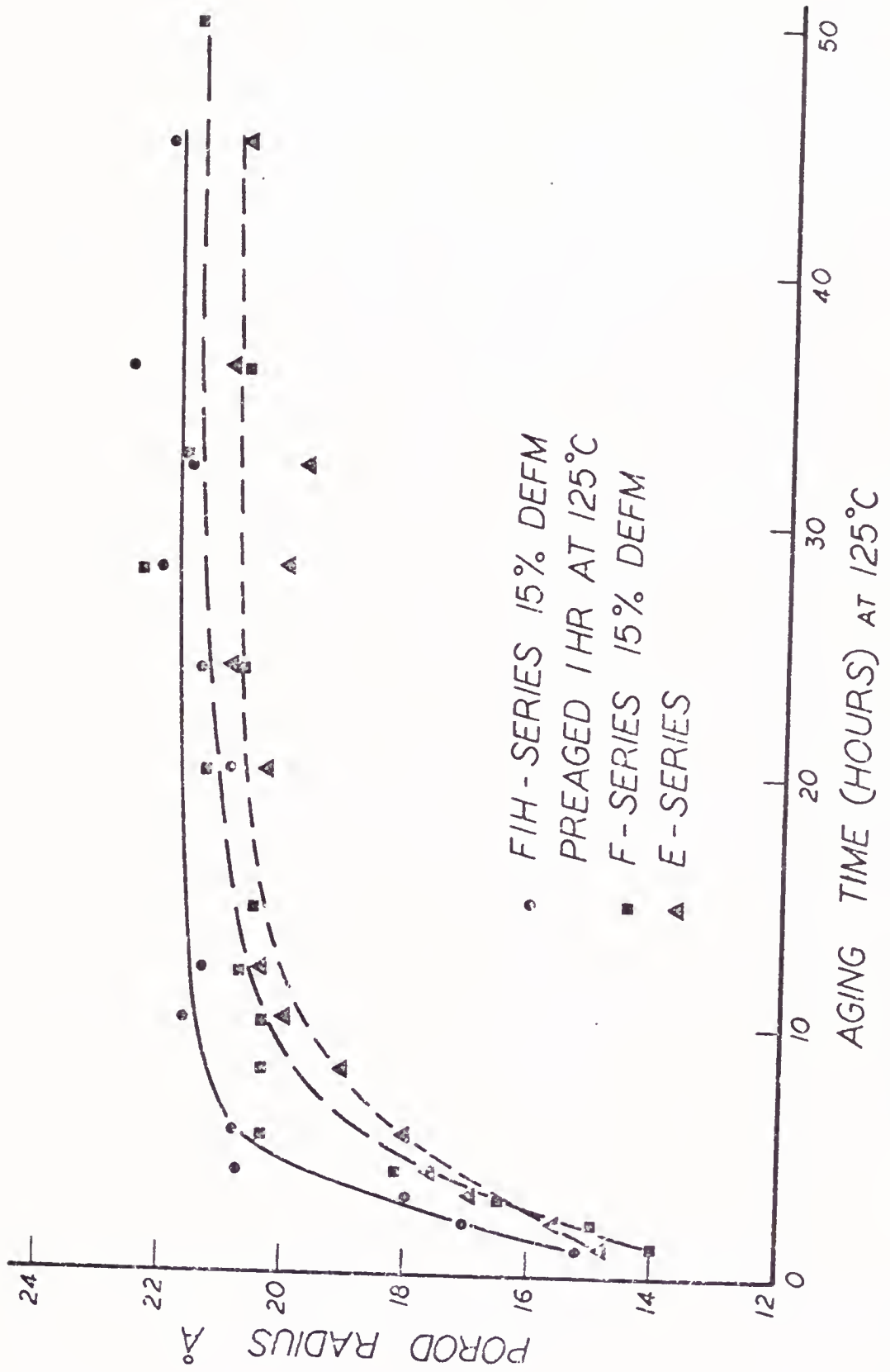
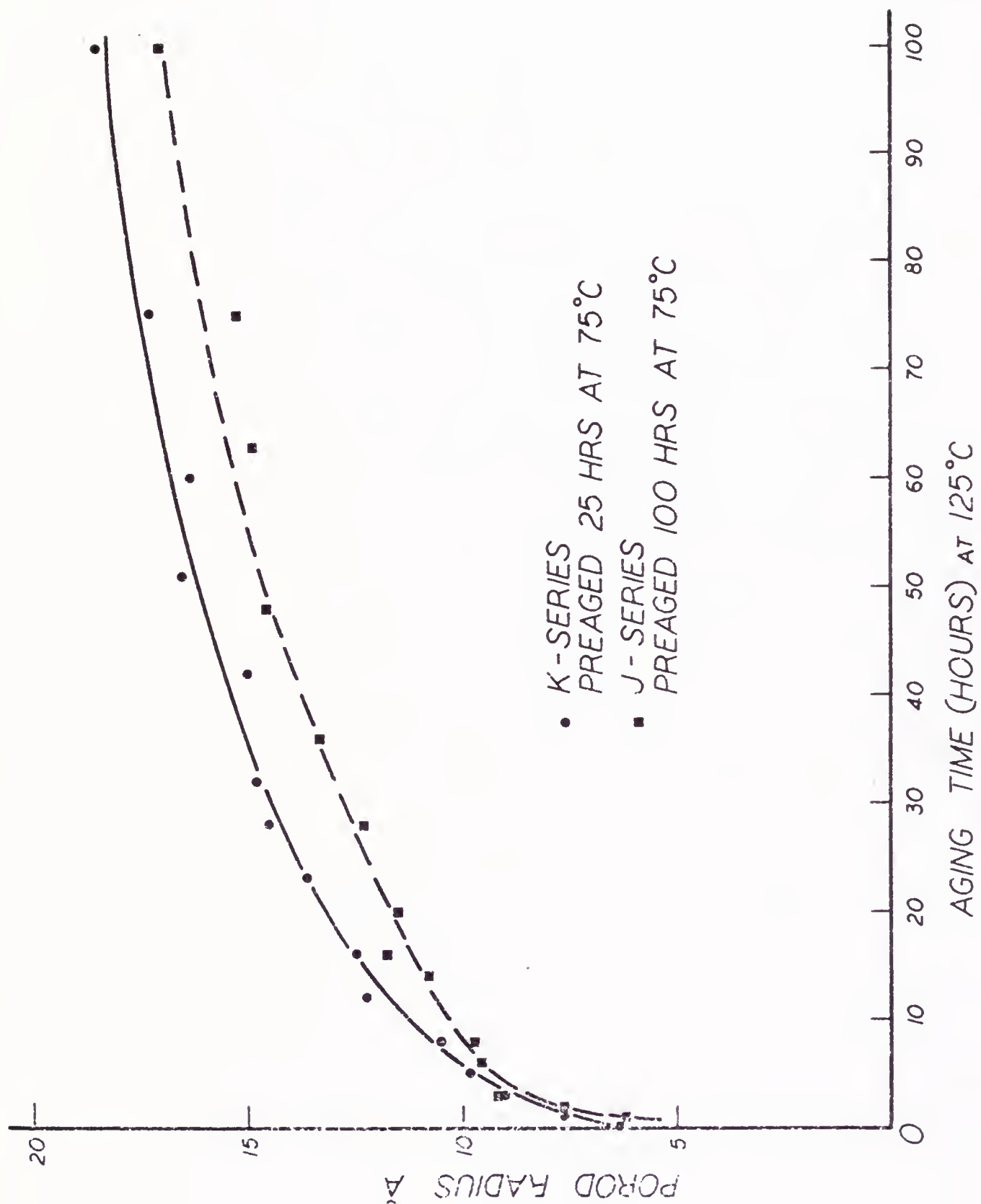


Figure 23. Porod Radius Evolution for E, F, FIH Series as Determined by SAXS

Figure 24. Porod Radius Evolution for J and K Series as Determined by SAXS





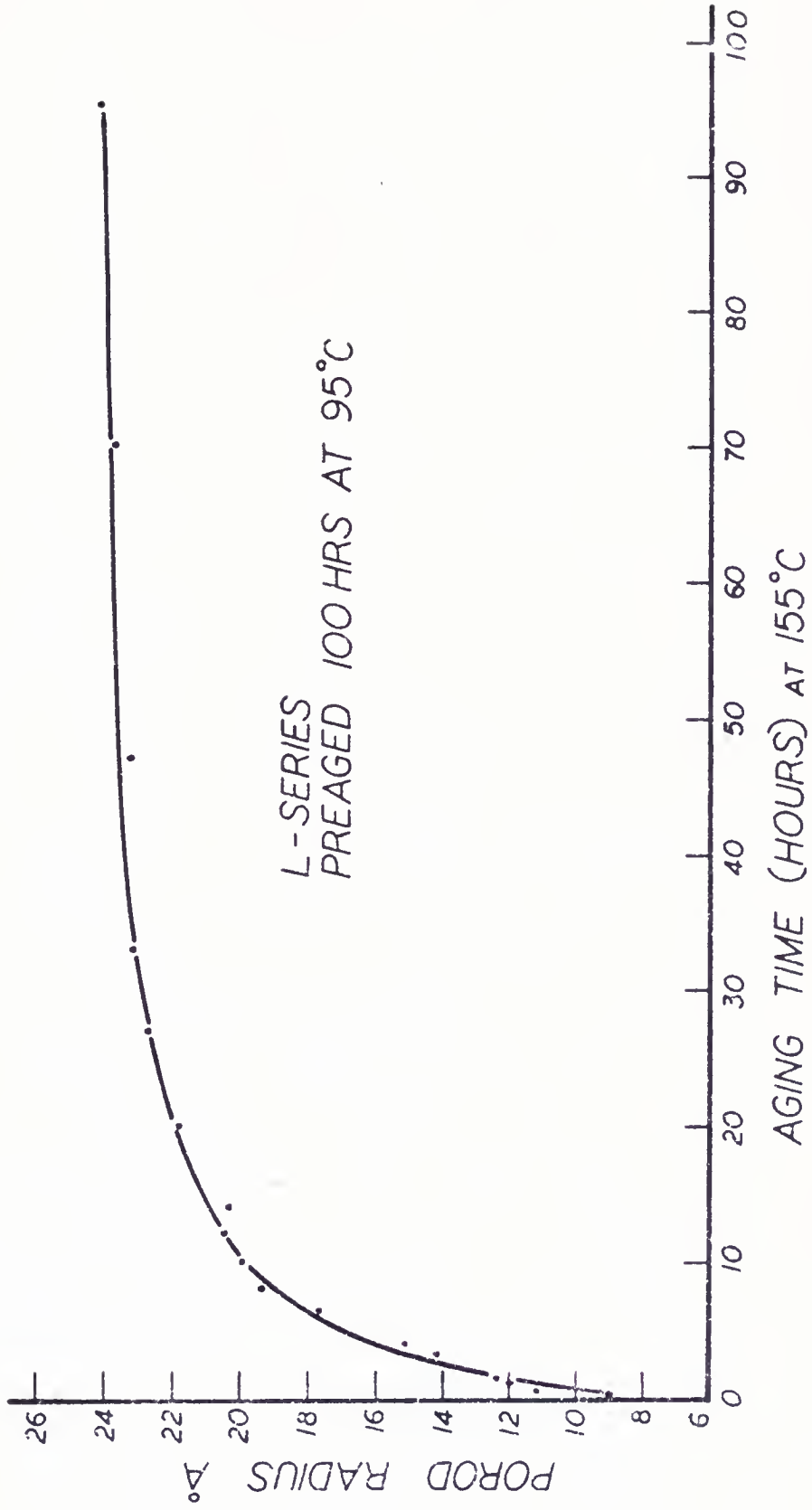


Figure 25. Porod Radius Evolution for L Series as Determined by SAXS

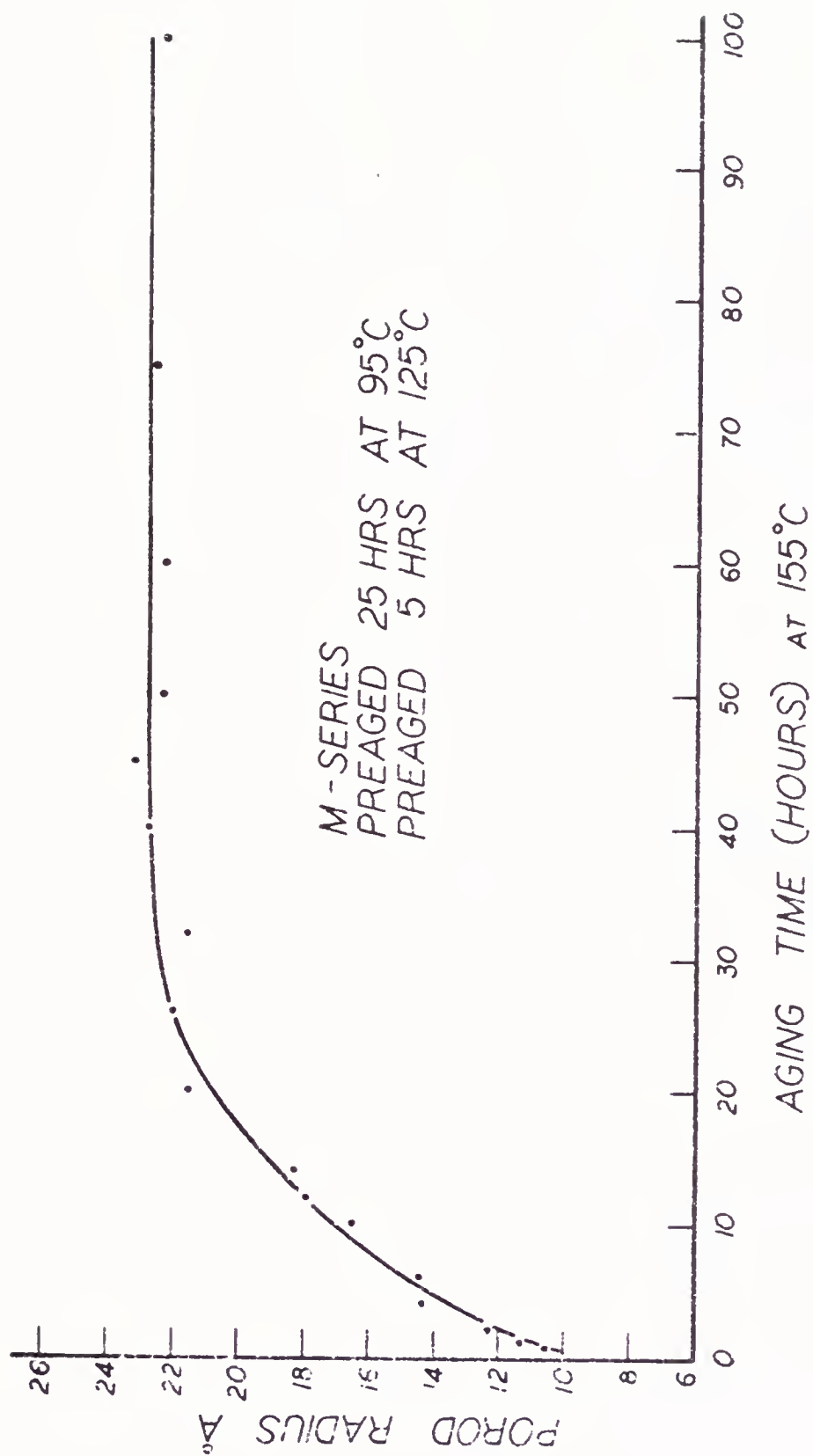


Figure 26. Porod Radius Evolution for M Series as Determined by SAXS

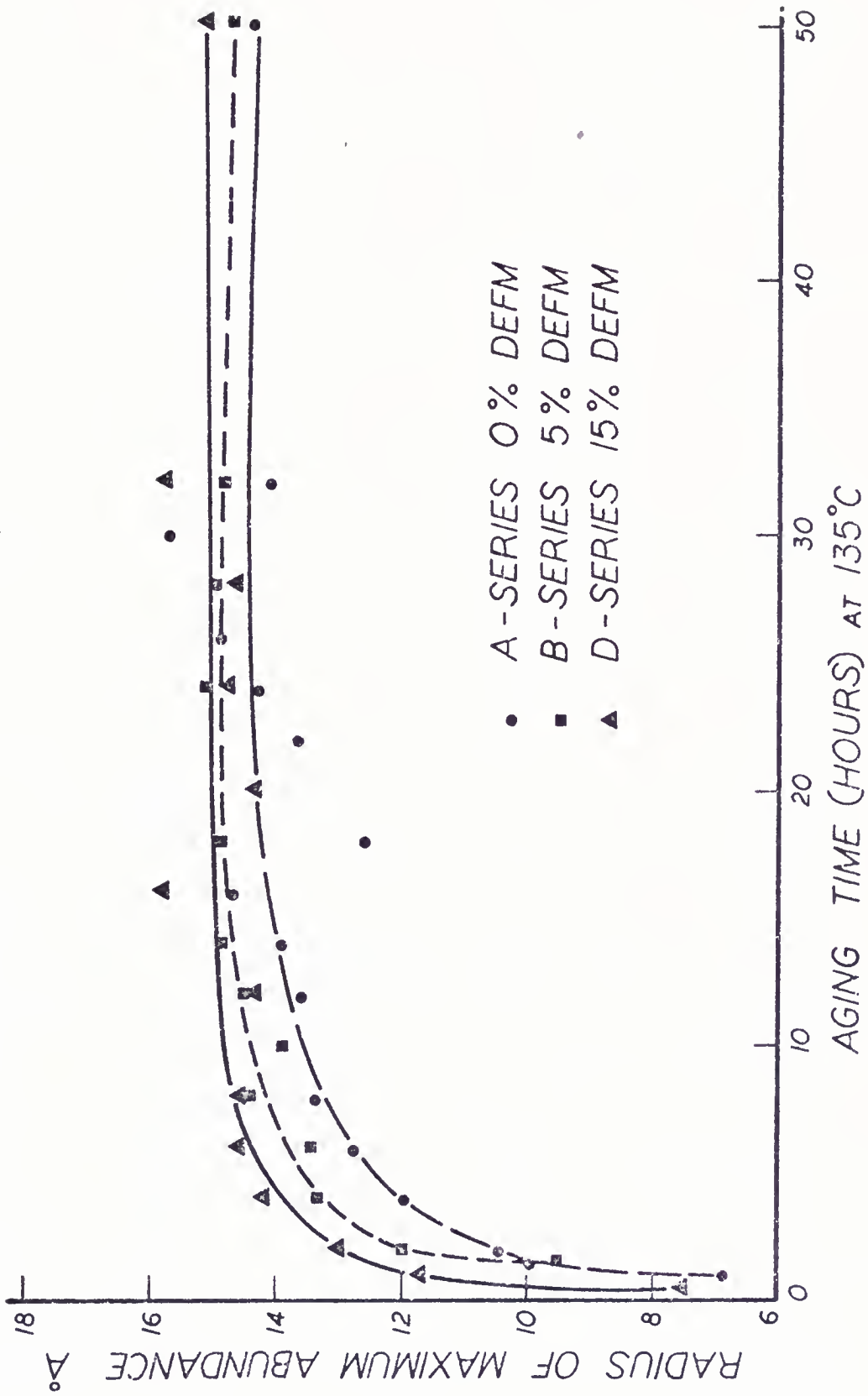


Figure 27. Radius of Maximum Abundance for A, B, D Series as Determined by SAXS

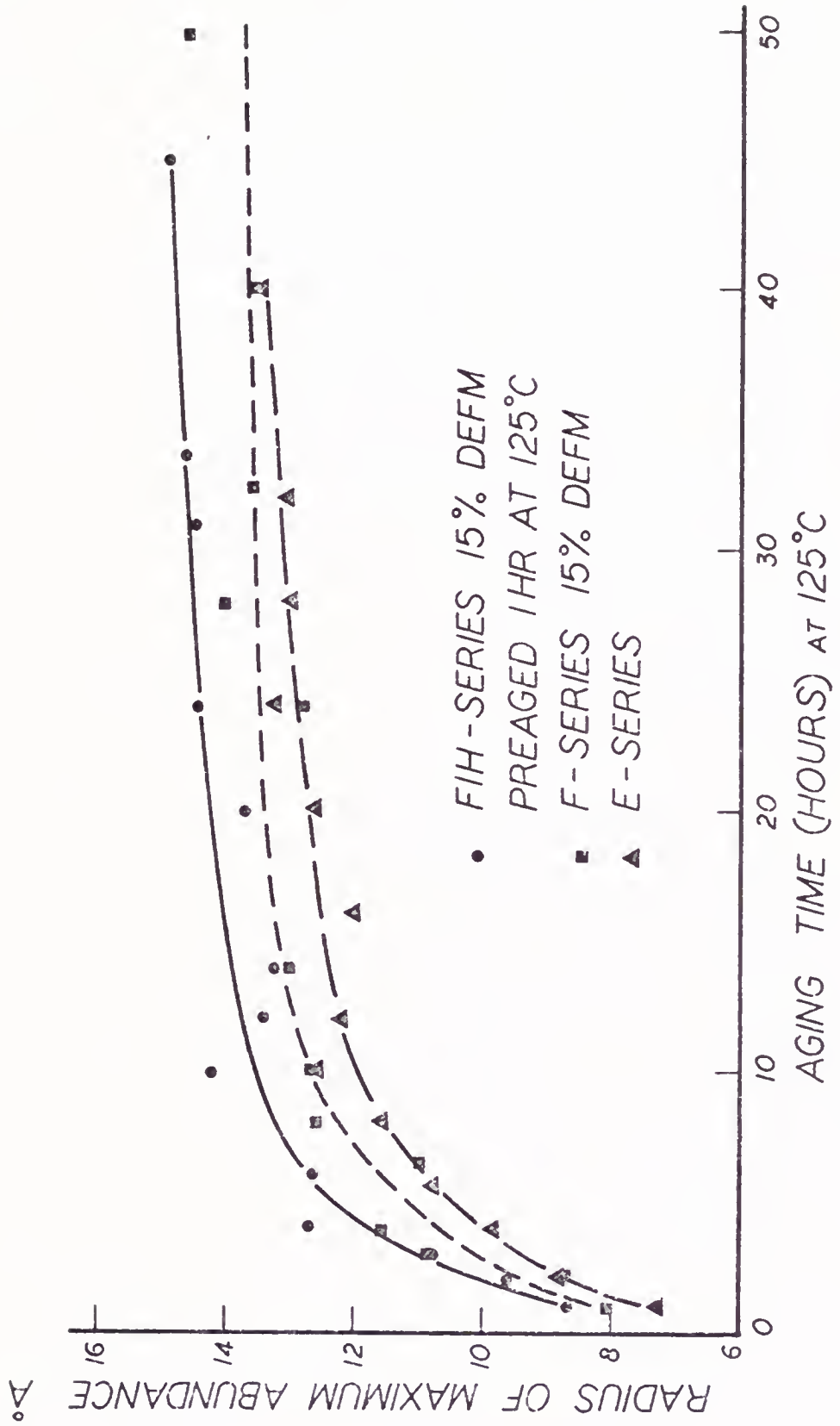


Figure 28. Radius of Maximum Abundance for E, F Series as Determined by SAXS

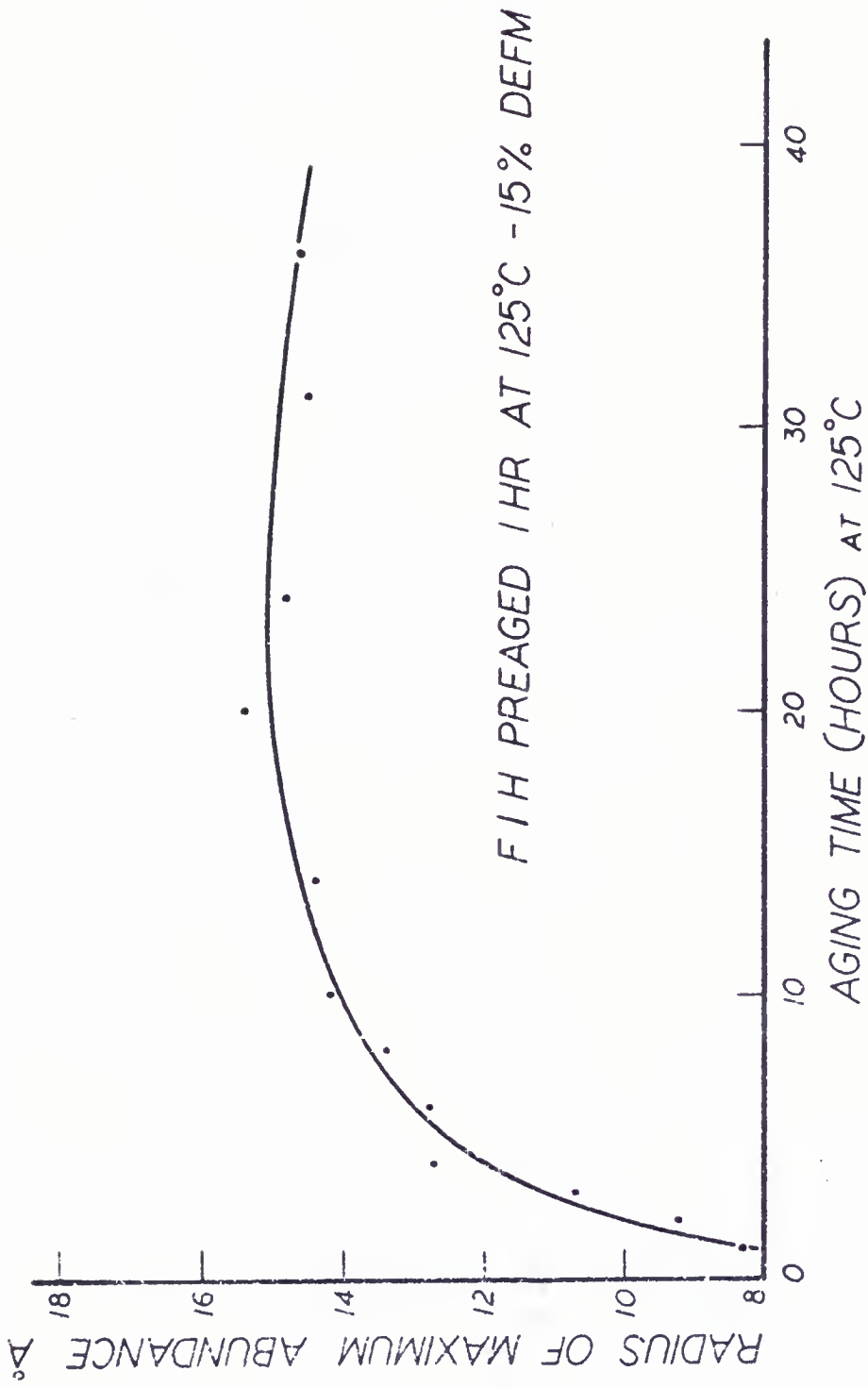


Figure 29. Radius of Maximum Abundance for FIH Series as Determined by SAXS

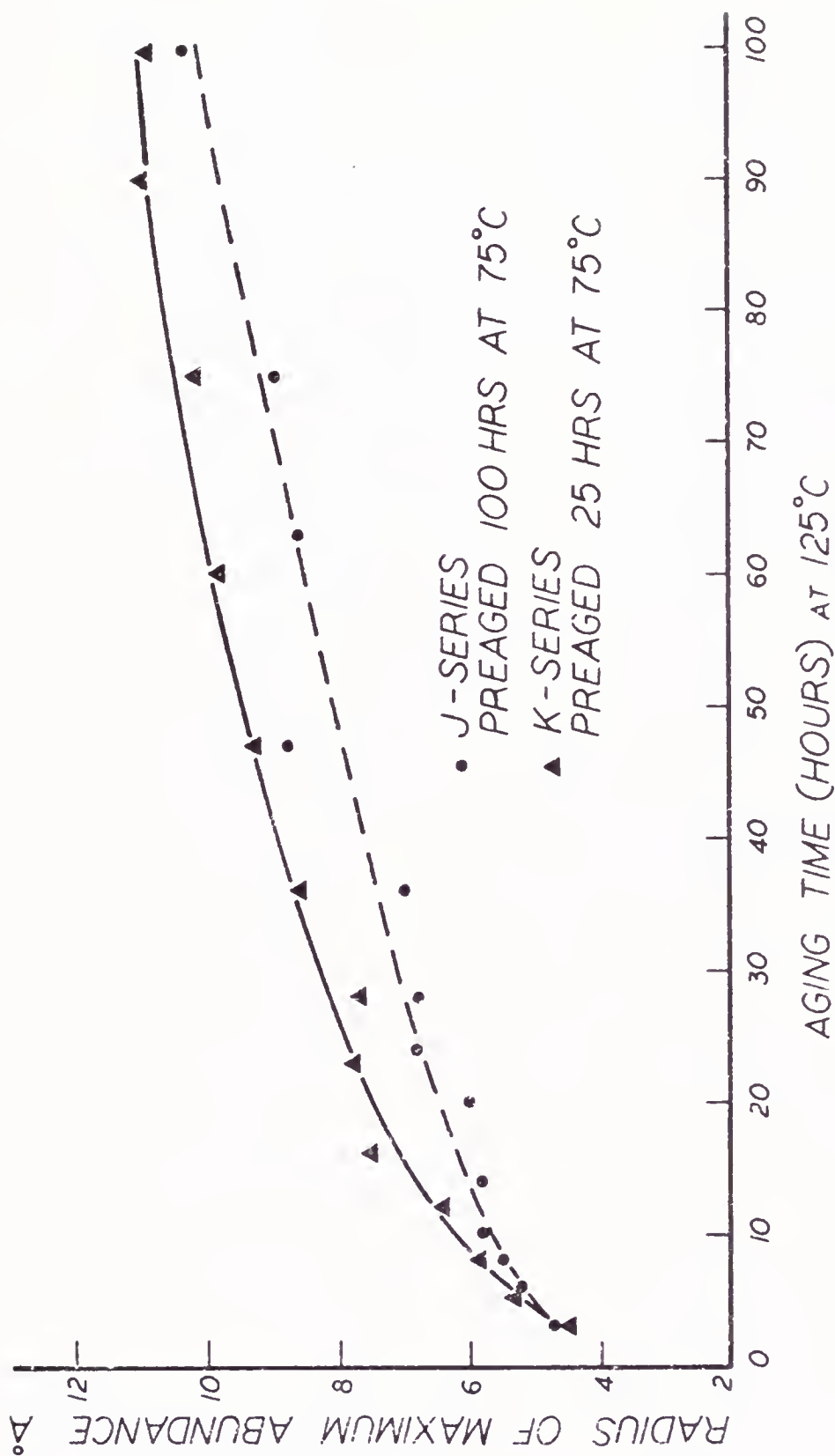


Figure 30. Radius of Maximum Abundance for J and K Series as Determined by SAXS

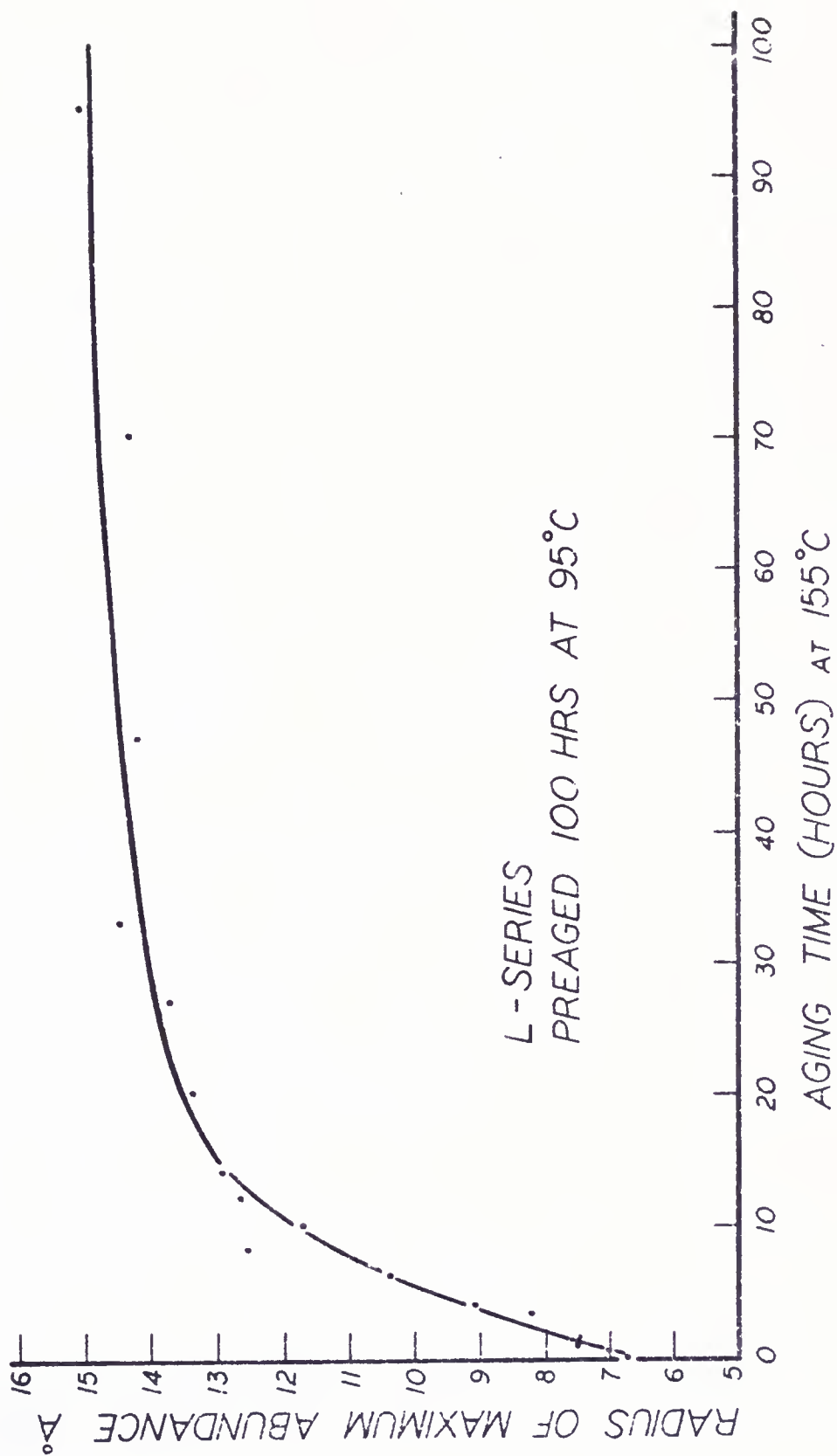


Figure 31. Radius of Maximum Abundance for L Series as Determined by SAXS



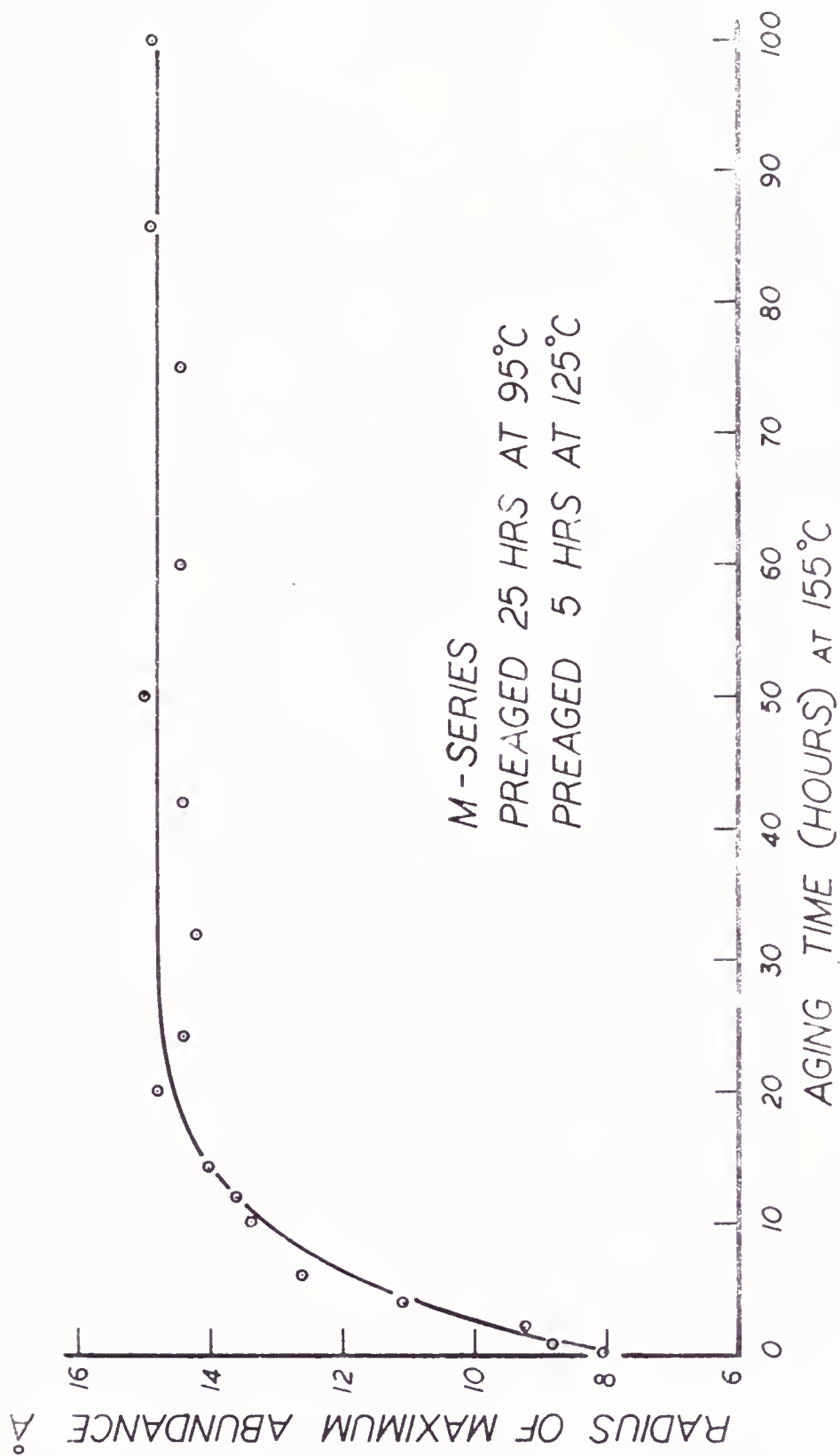


Figure 32. Radius of Maximum Abundance for M Series as Determined by SAXS

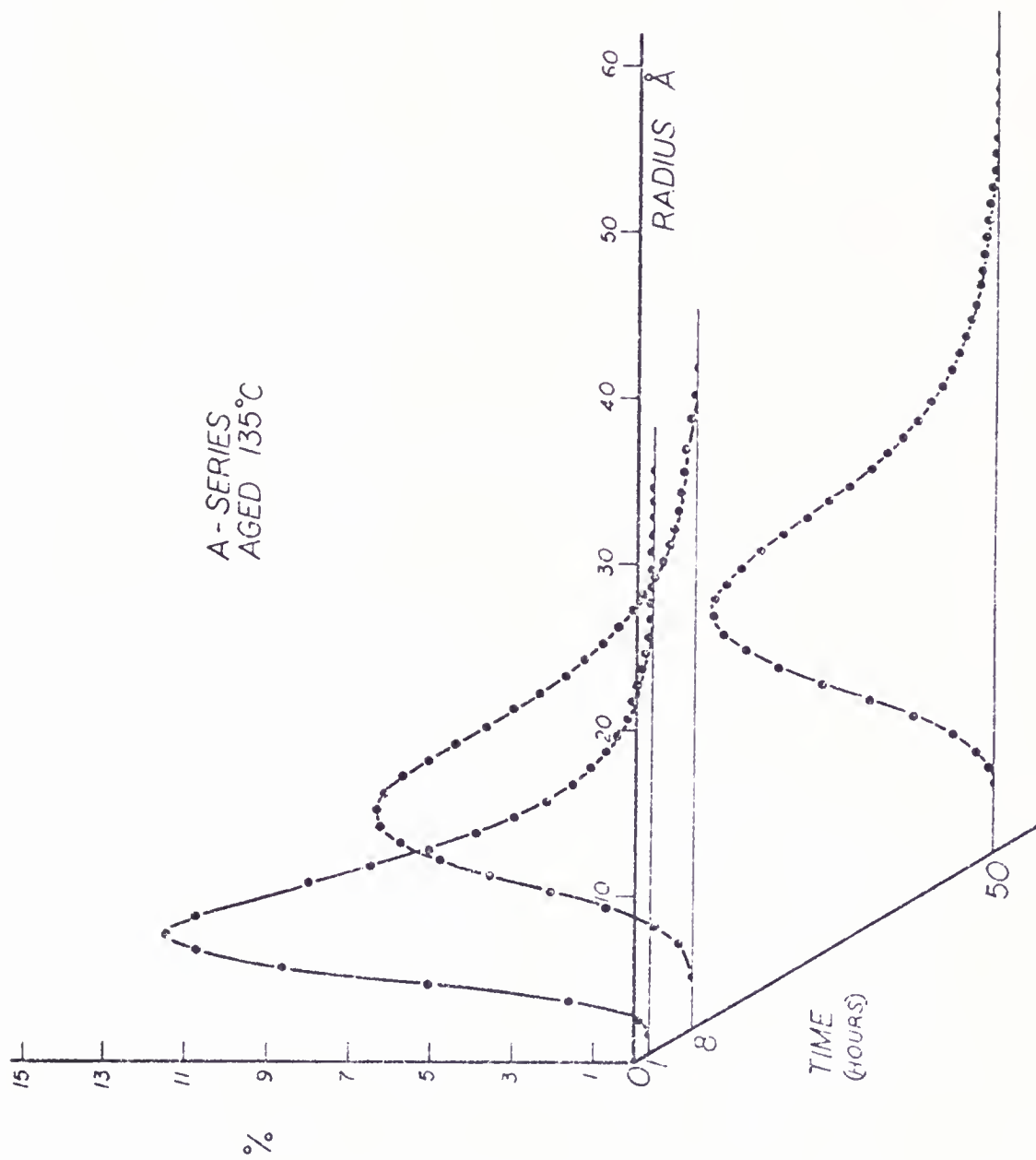


Figure 33. Particle Size Distribution Evolution for A Series

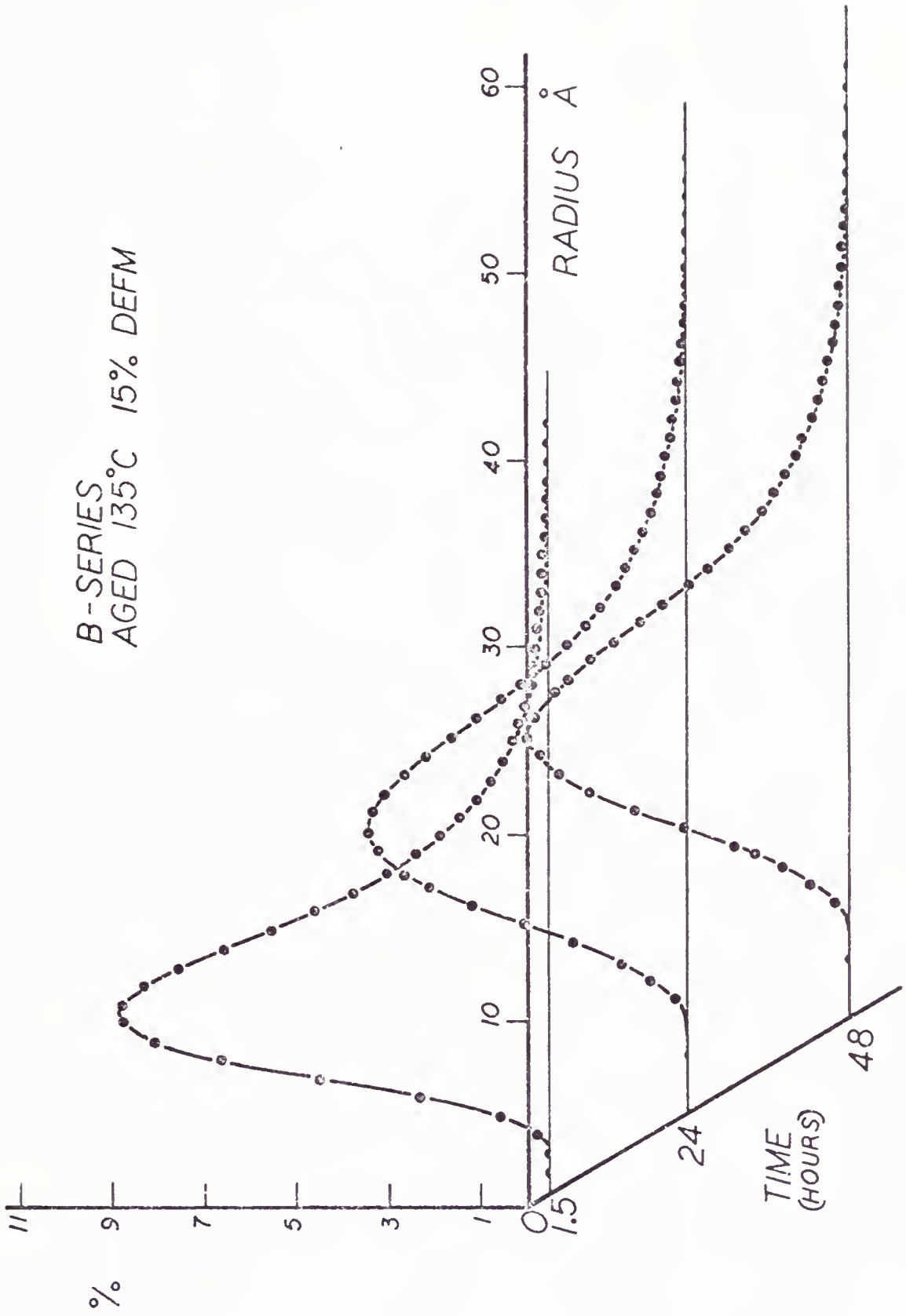


Figure 34. Particle Size Distribution Evolution for B Series

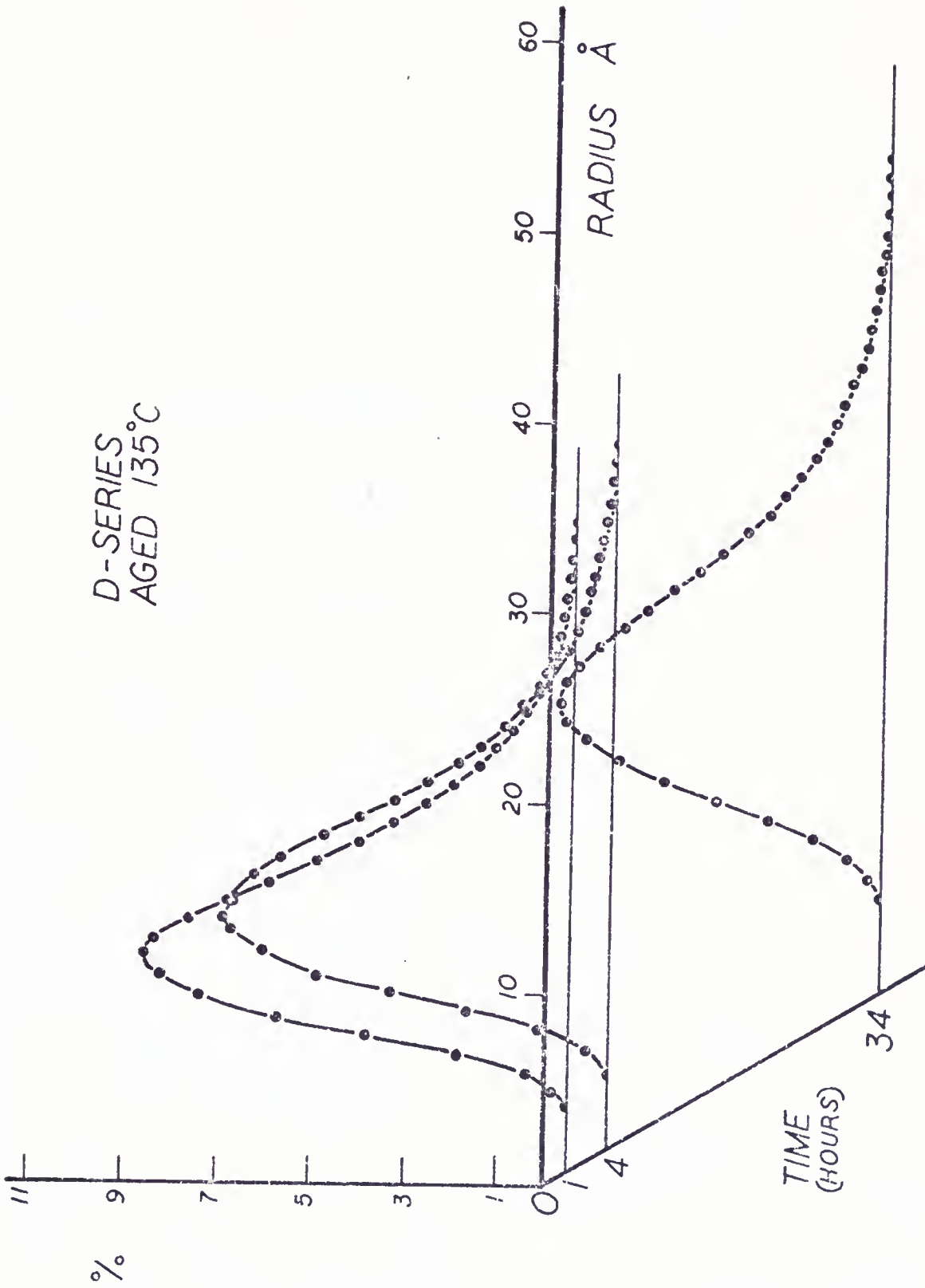


Figure 35. Particle Size Distribution Evolution for D Series

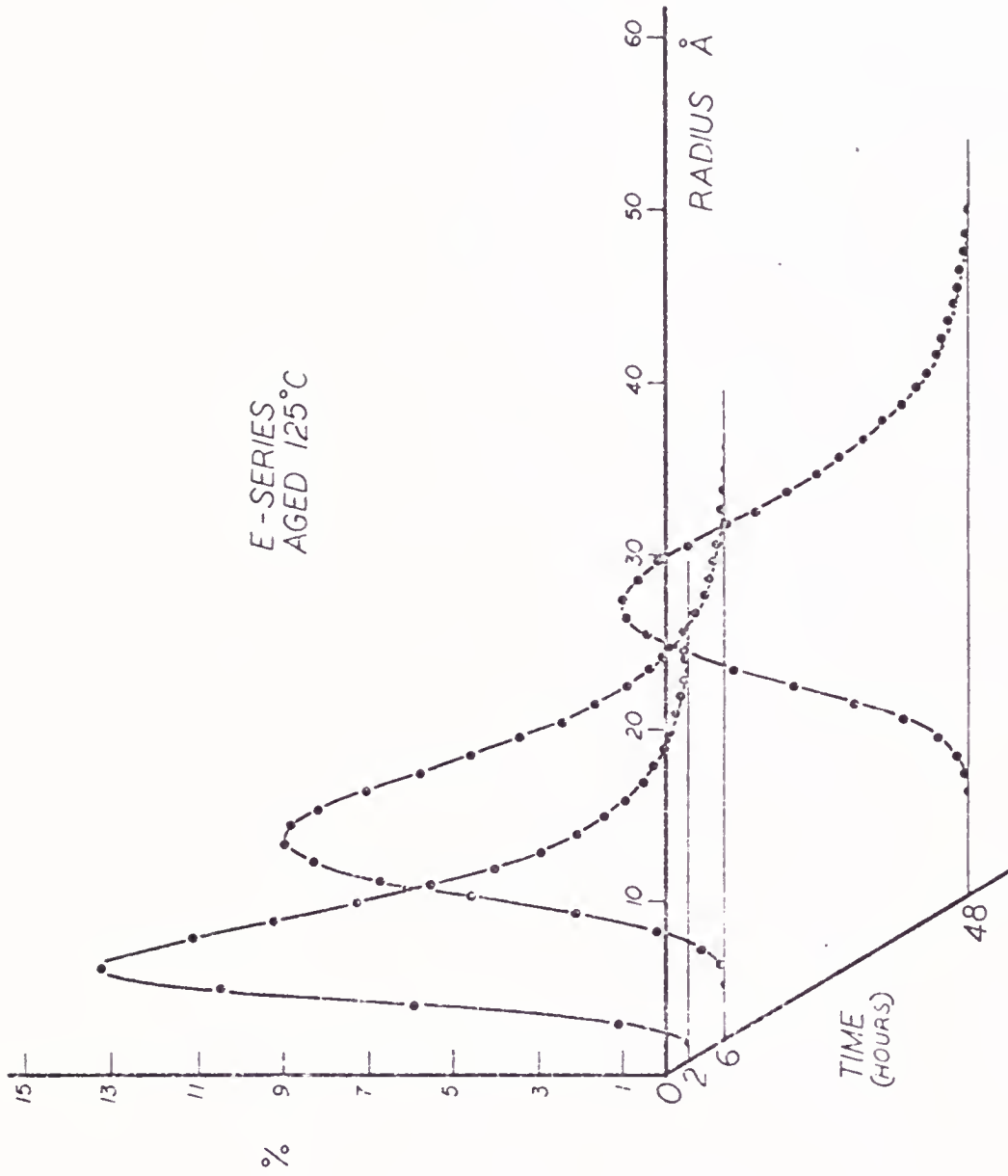


Figure 36. Particle Size Distribution Evolution for E Series

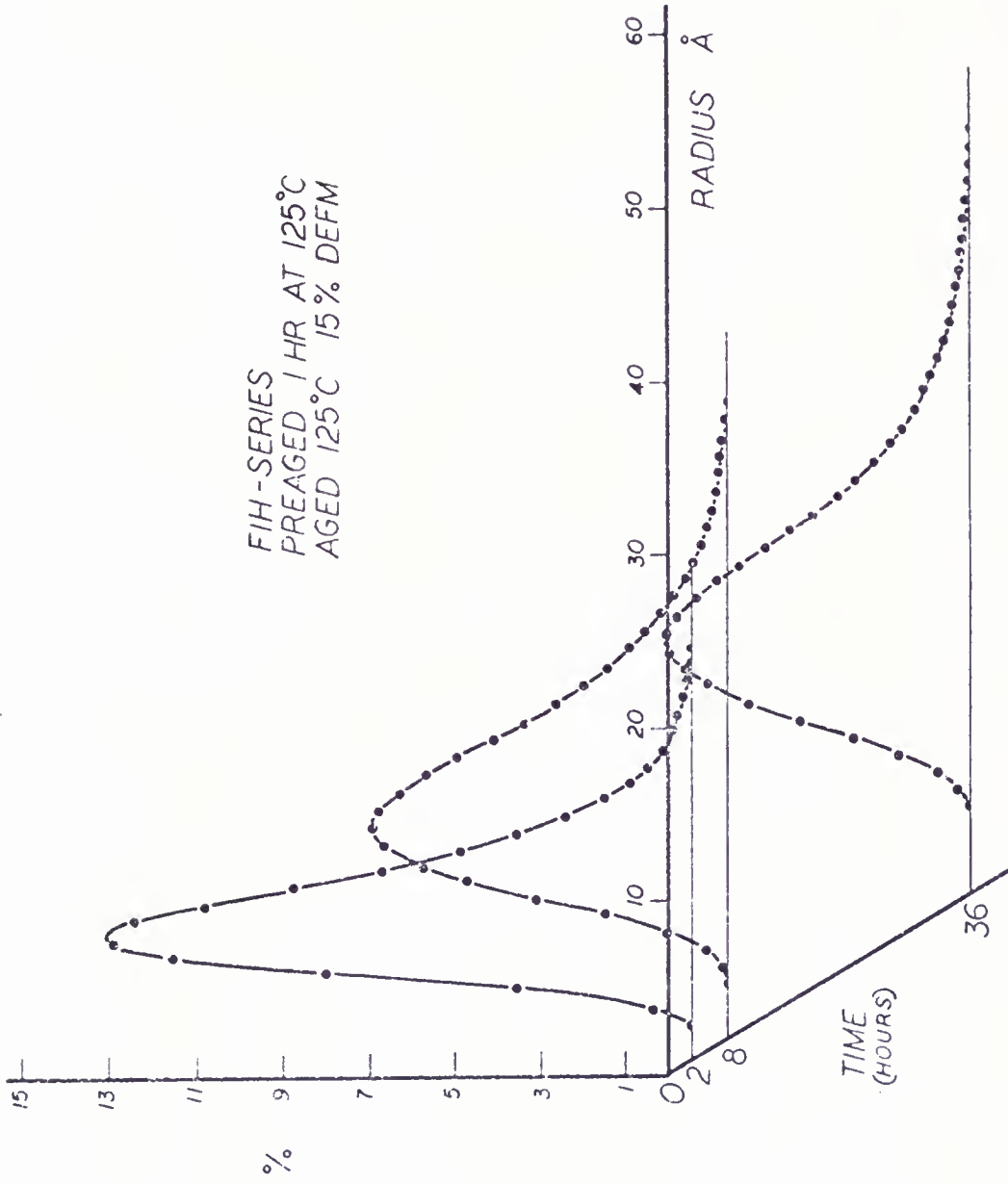


Figure 37. Particle Size Distribution Evolution for FIH Series

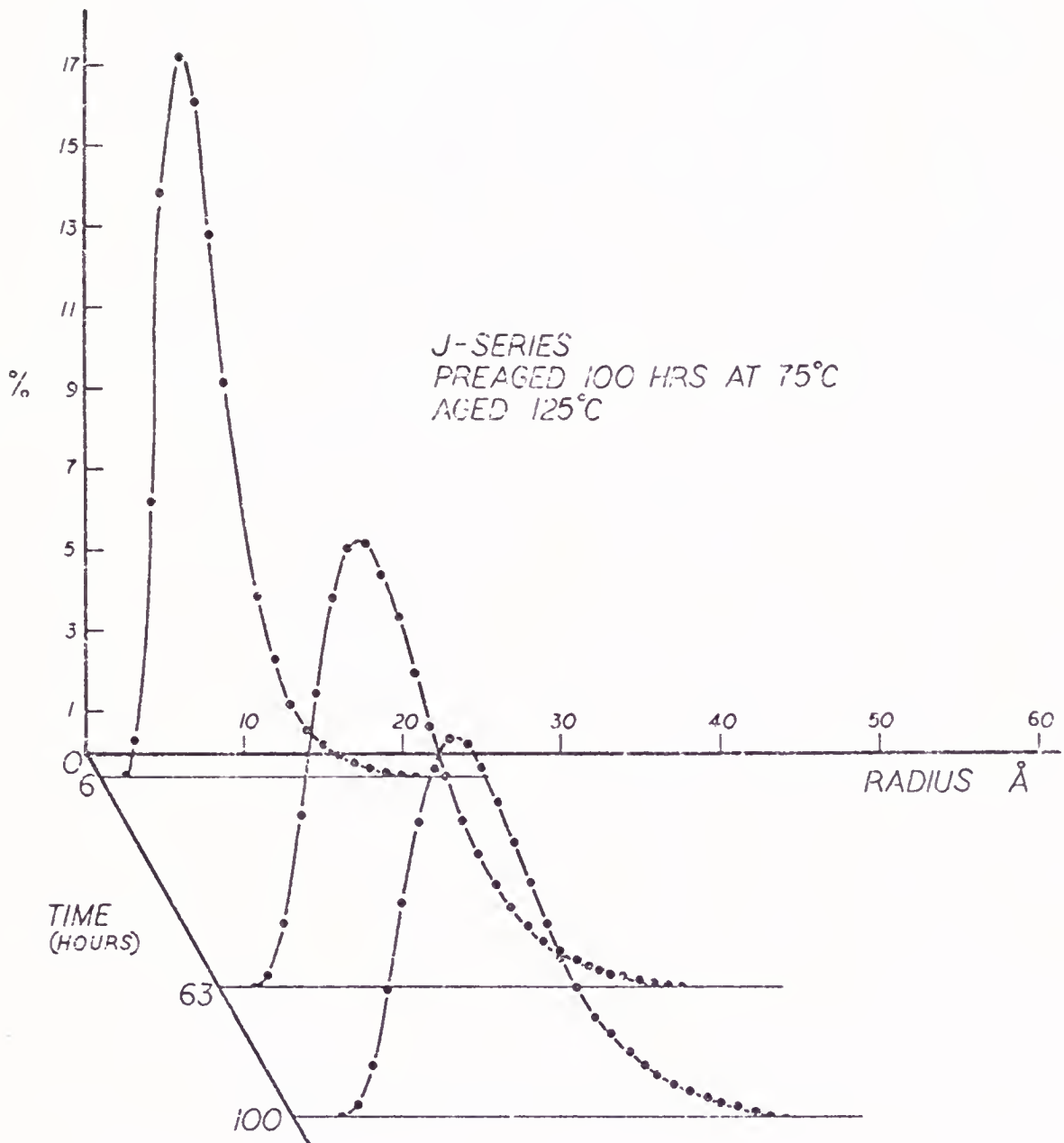


Figure 38. Particle Size Distribution Evolution for J

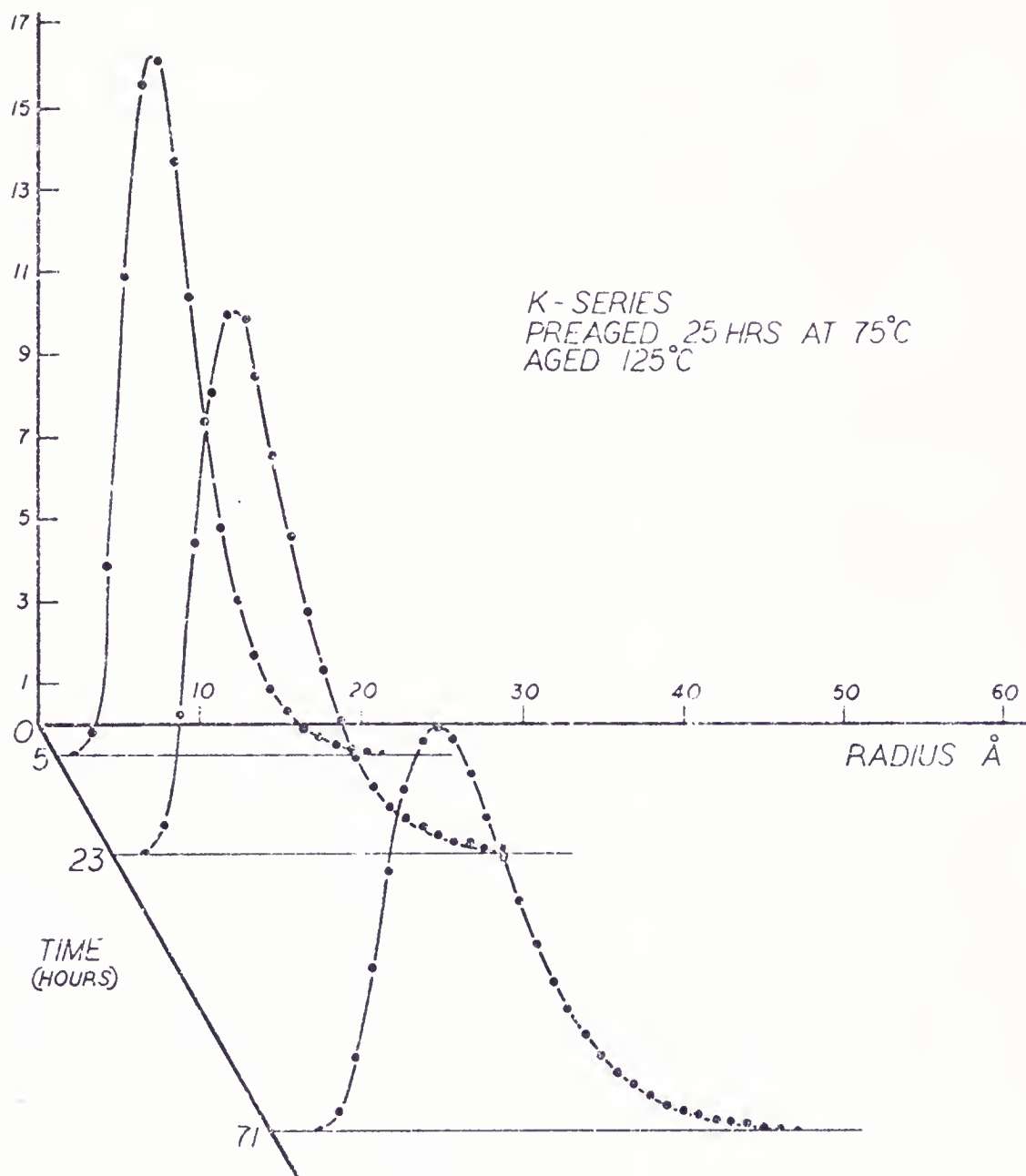


Figure 39. Particle Size Distribution Evolution for K Series



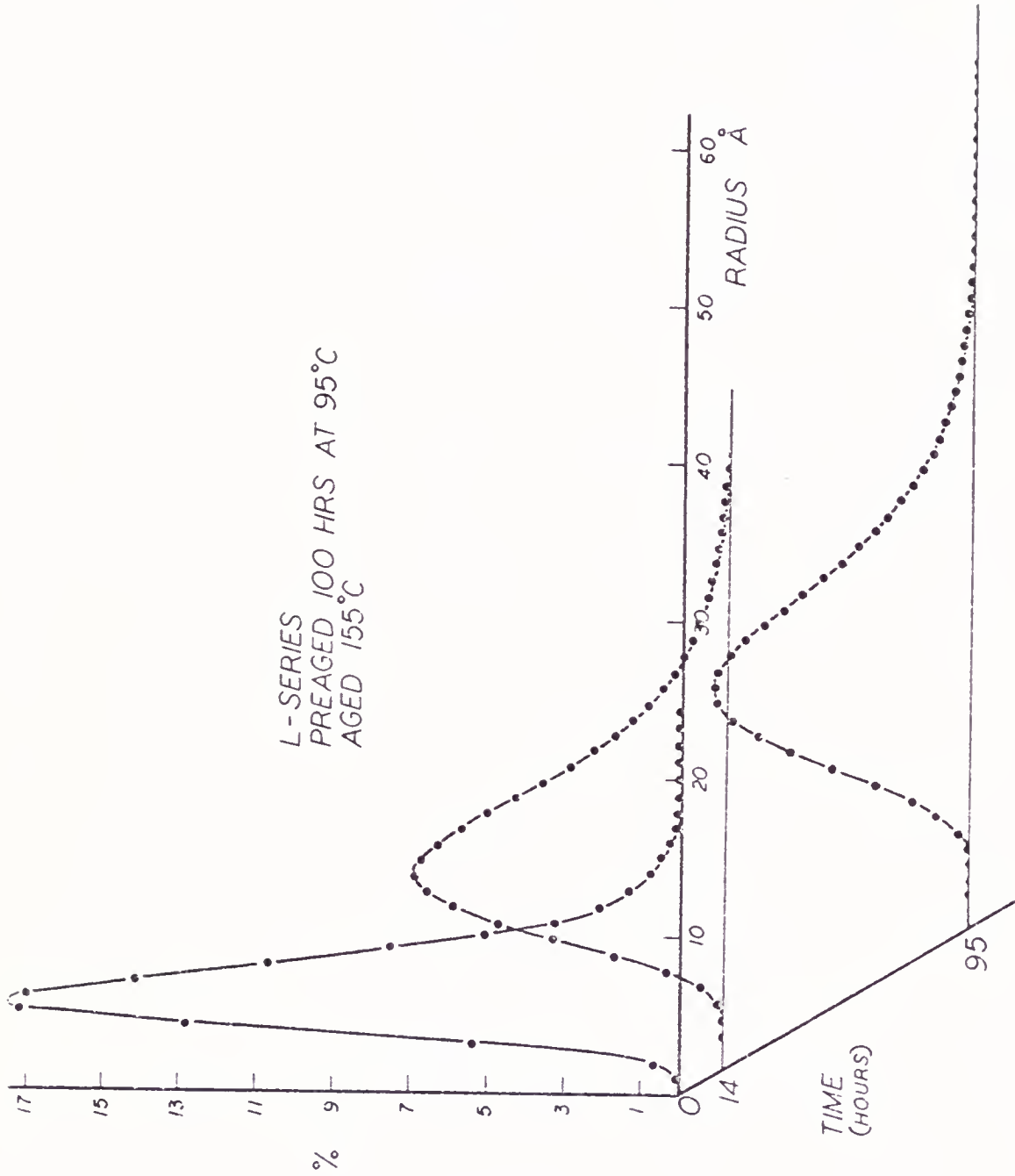


Figure 40. Particle Size Distribution Evolution for L Series

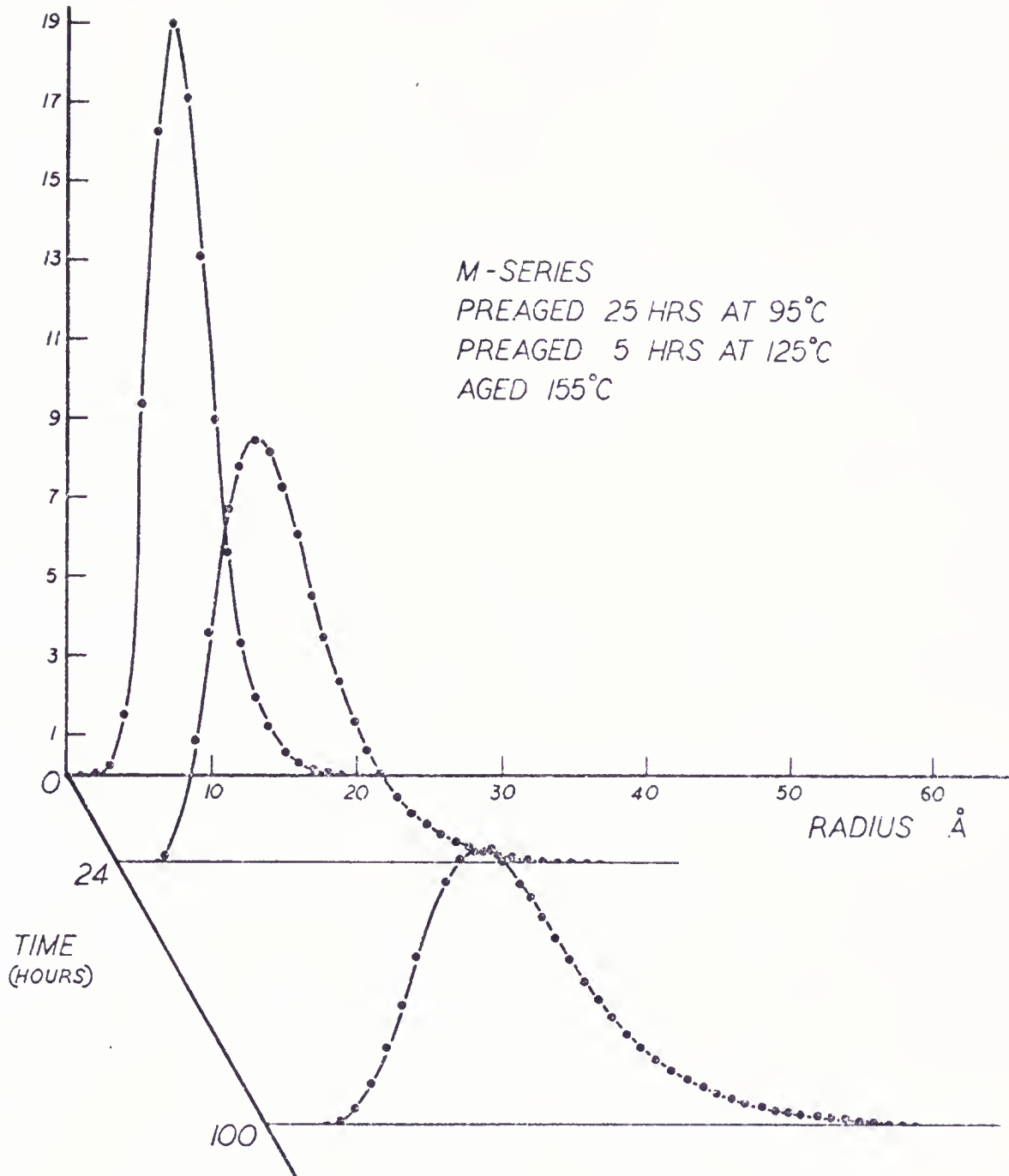


Figure 41. Particle Size Distribution Evolution for M Series

### Relative Integrated Intensity

The value of the relative integrated intensity was also calculated by the same computer program. The changes in the integrated intensity as a function of aging time are presented in Figures 42 through 47. The physical significance of this parameter will be discussed in Chapter V.

### Wide Angle Diffraction

Preliminary experiments were conducted on a diffractometer. The results of this technique proved to be too dependent upon surface condition, so all high angle diffraction studies were made in transmission using a Guinier-De Wolff camera and  $M_oK$  radiation. Figure 48 shows a typical sequence of densitometer scans of the films for one of the series. Table 4 gives the d spacings obtained, and the phases identified.

### Tensile Tests

Tensile tests were performed on two or three duplicate samples to obtain the yield and ultimate tensile strength. The tests were run at room temperature and the results of the average values obtained for the duplicate samples are presented in Figures 49 through 55. The yield values are those obtained at 0.02% strain offset using samples described in Chapter III. The change in the val-

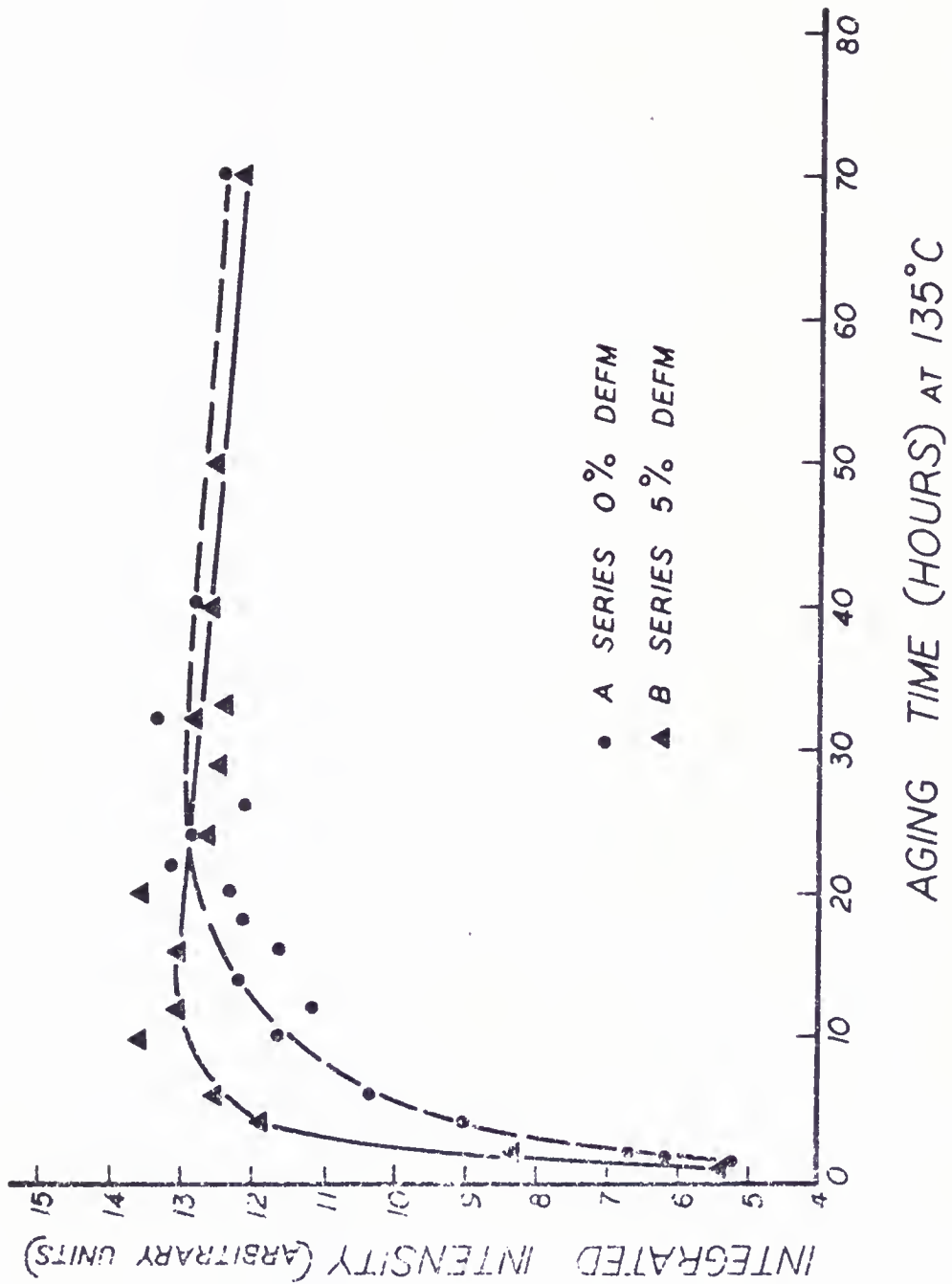
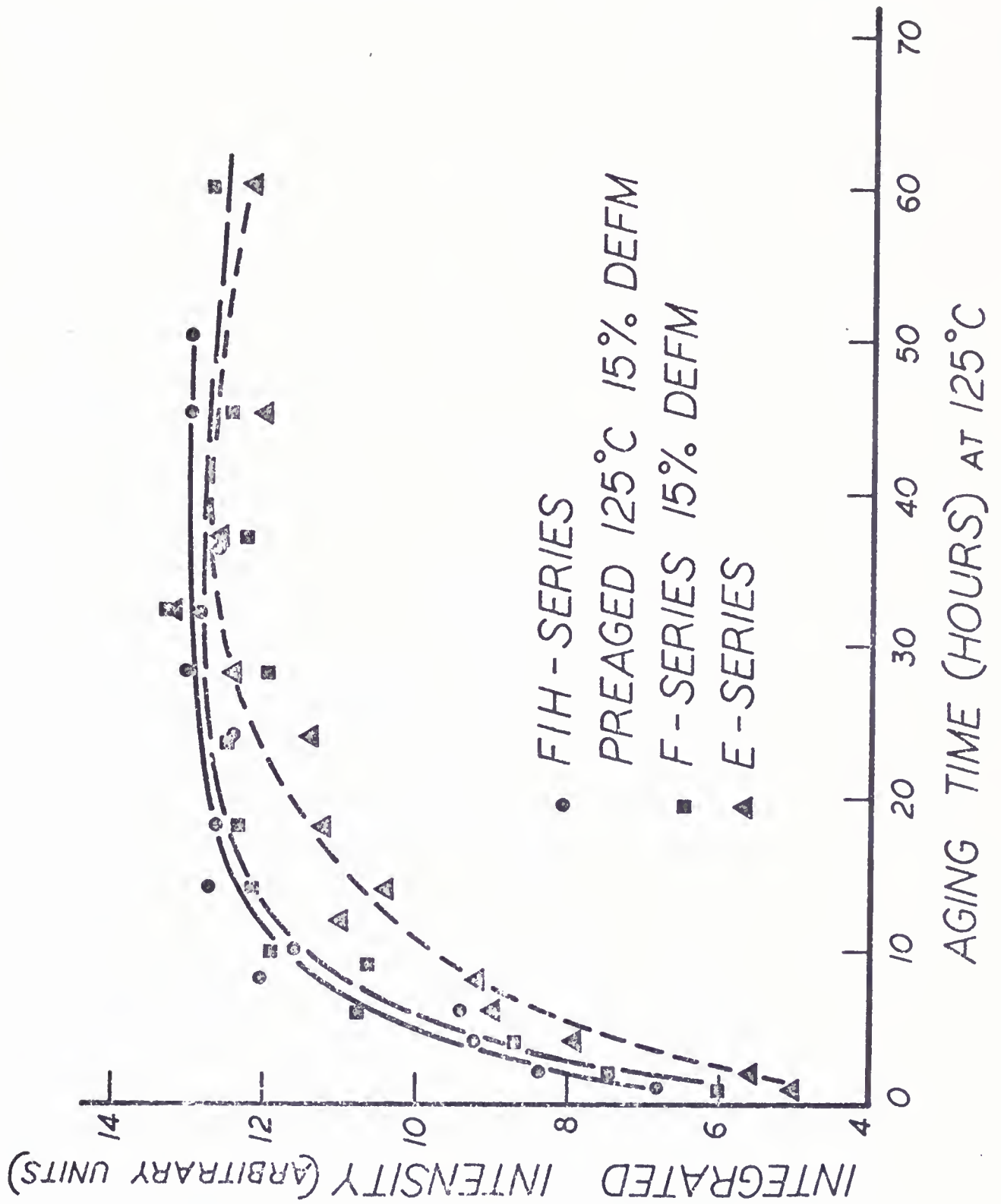


Figure 42. Relative Integrated Intensity for A and B Series

Figure 43. Relative Integrated Intensity for E, F, FlH Series



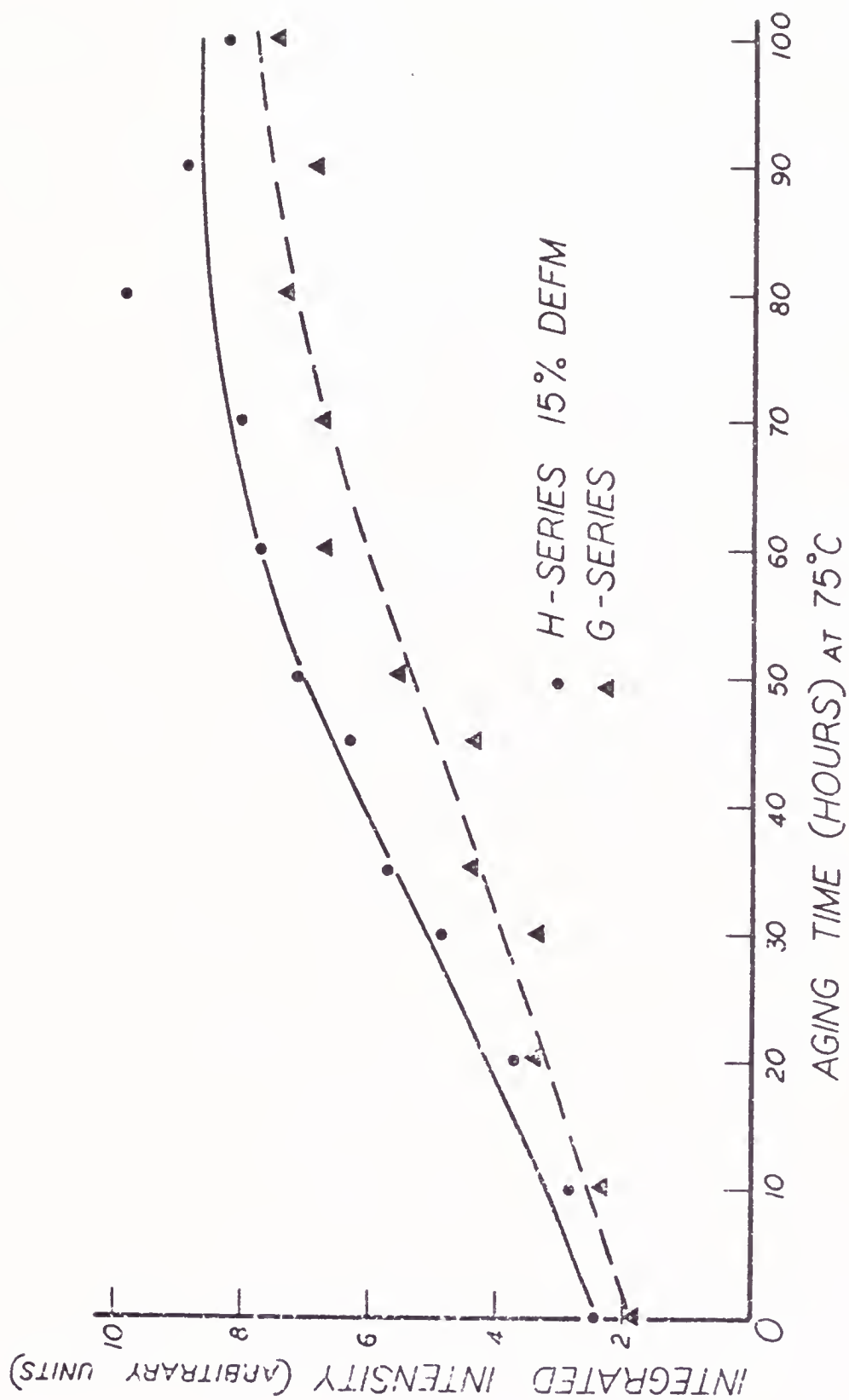
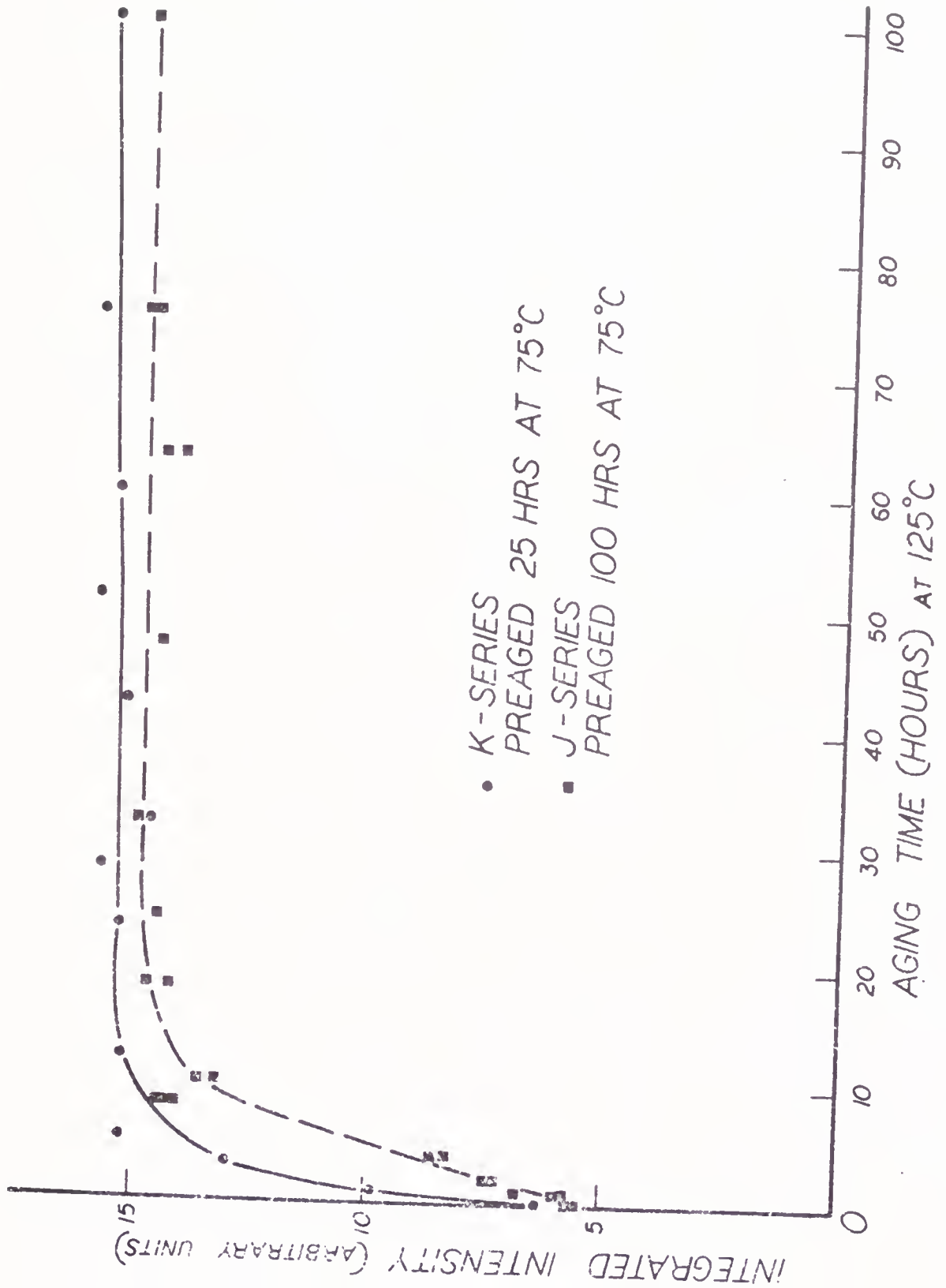


Figure 44. Relative Integrated Intensity for G and H Series

Figure 45. Relative Integrated Intensity for J and K Series





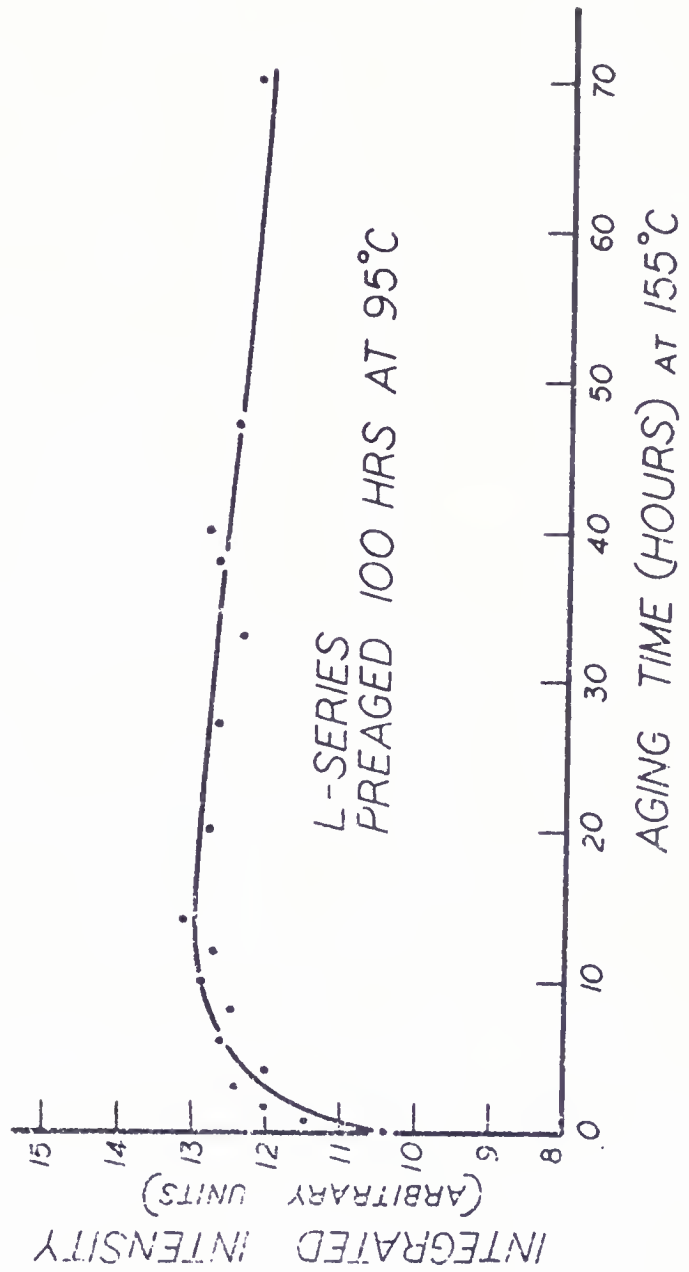


Figure 46. Relative Integrated Intensity of L Series

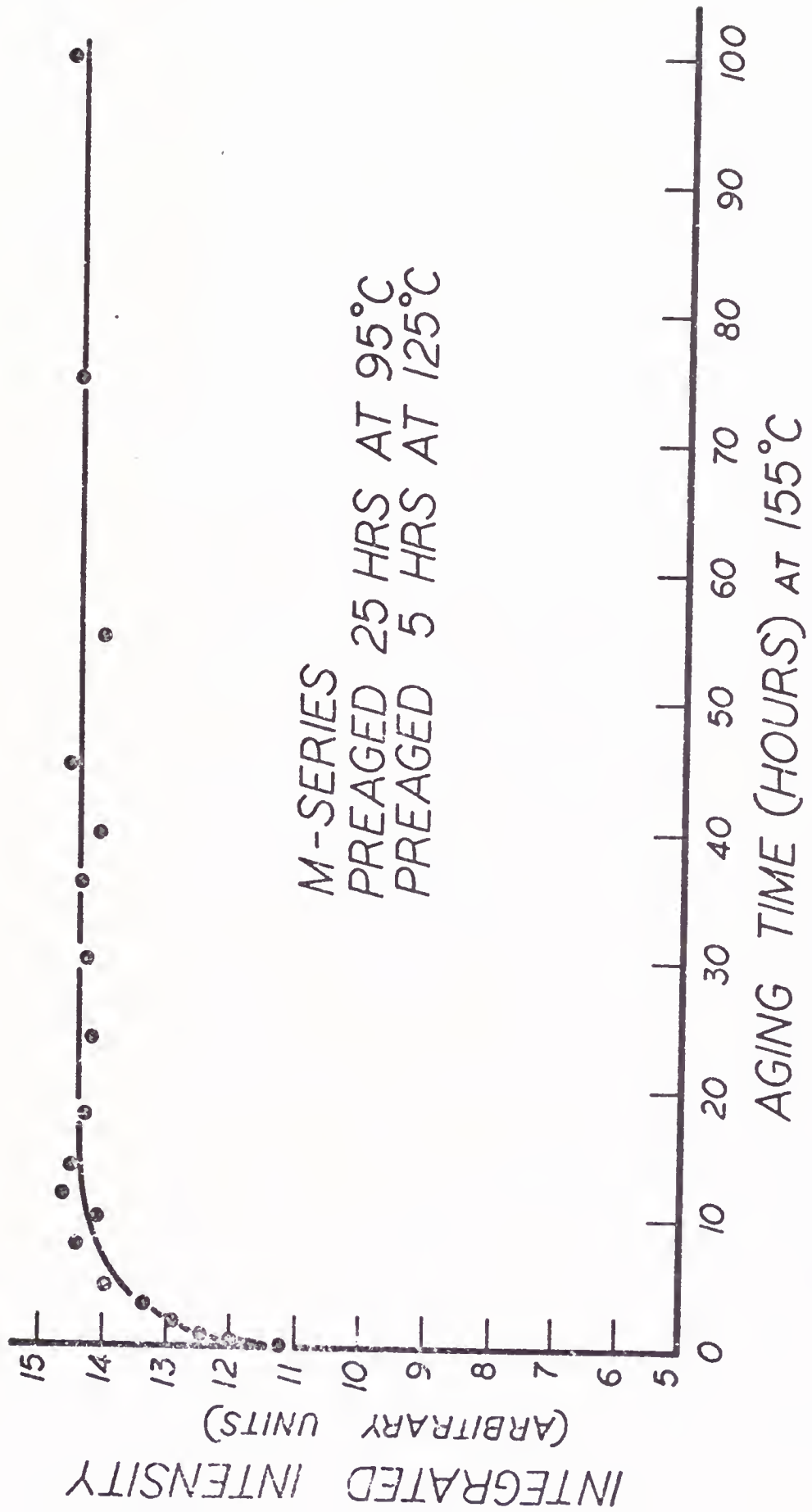


Figure 47. Relative Integrated Intensity for M Series

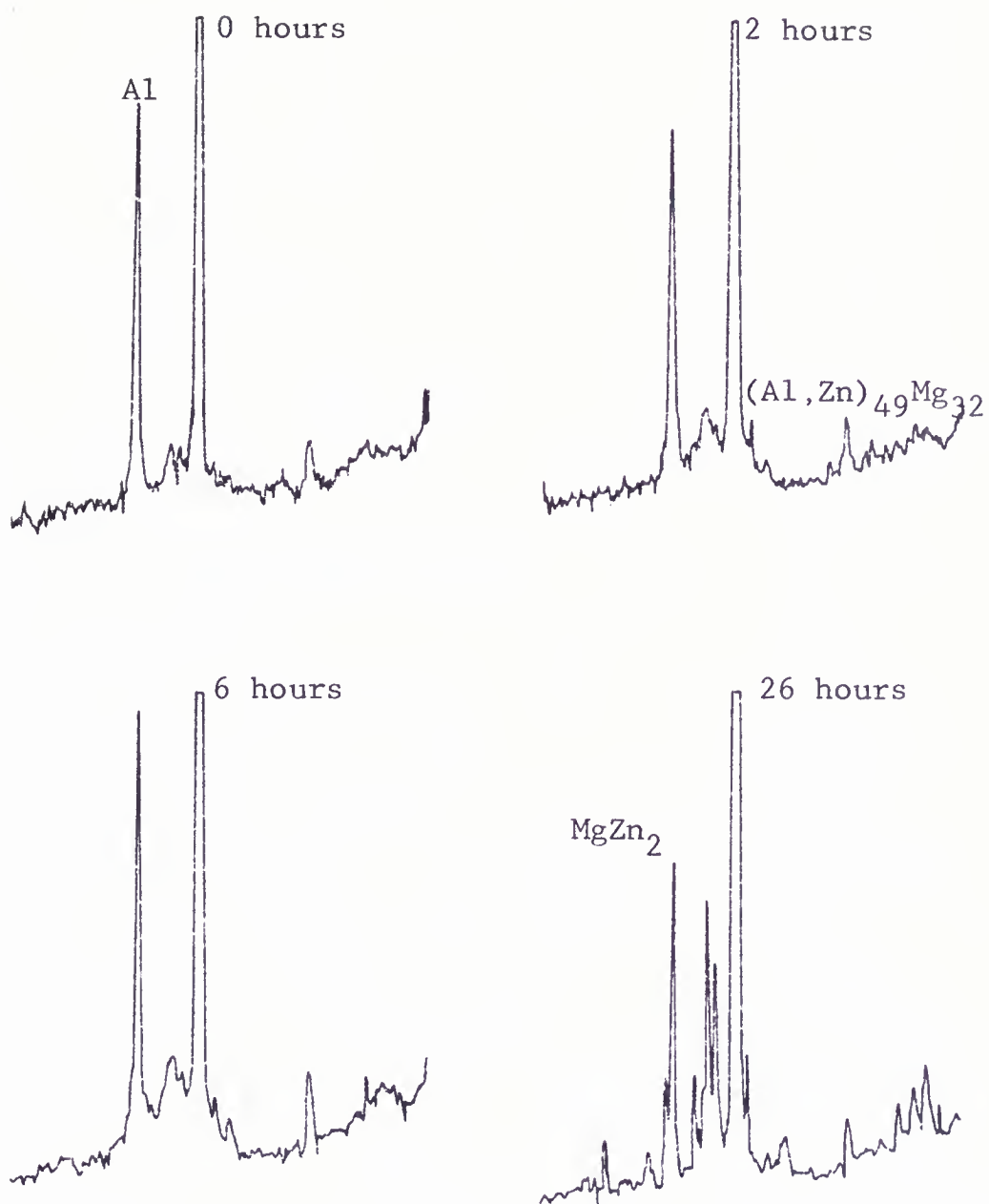


Figure 48. Densitometer Scans of Eseries (125°C Age)  
Guinier-De Wolff Films

Table 4

## Summary of Results of Wide Angle Diffraction

d spacing	Al	MgZn <sub>2</sub>	(Al,Zn) <sub>49</sub> Mg <sub>32</sub>
4.52		X	
4.26		X	
4.01		X	
3.26			
2.44			X
2.39		X	
2.33	X		X
2.22		X	
2.18		X	
2.12		X	
2.01	X	X	X
1.98		X	
1.92		X	
1.76		X	
1.71		X	
1.45		X	
1.43		X	
1.42	X		
1.35		X	
1.33		X	
1.296		X	
1.21	X		
1.16	X		

ues of both yield and ultimate strength occurred approximately parallel for the directly aged series, and consequently, only one is presented. For those series where the changes are not occurring in a similar manner, both values are generally given.

#### Other Mechanical Tests

Initially, microhardness and hardness tests were performed, but it was found that their change closely followed that of the ultimate tensile strength, so their measurement was abandoned in favor of the more physically significant values of the tensile strengths.

Charpy impact tests were also performed on several of the series, but it was found that, except for the very early aging times, this method was not sensitive enough to observe changes in the aging process.

#### Metallography

Optically, no visible difference could be observed between the as-quenched samples and the fully aged samples, as the size of the particles was far below the resolution of optical microscopy.

Transmission electron microscopy was performed on a number of samples, but differences between the samples only became resolvable after long aging times. This was due in part to the very small particle sizes present at

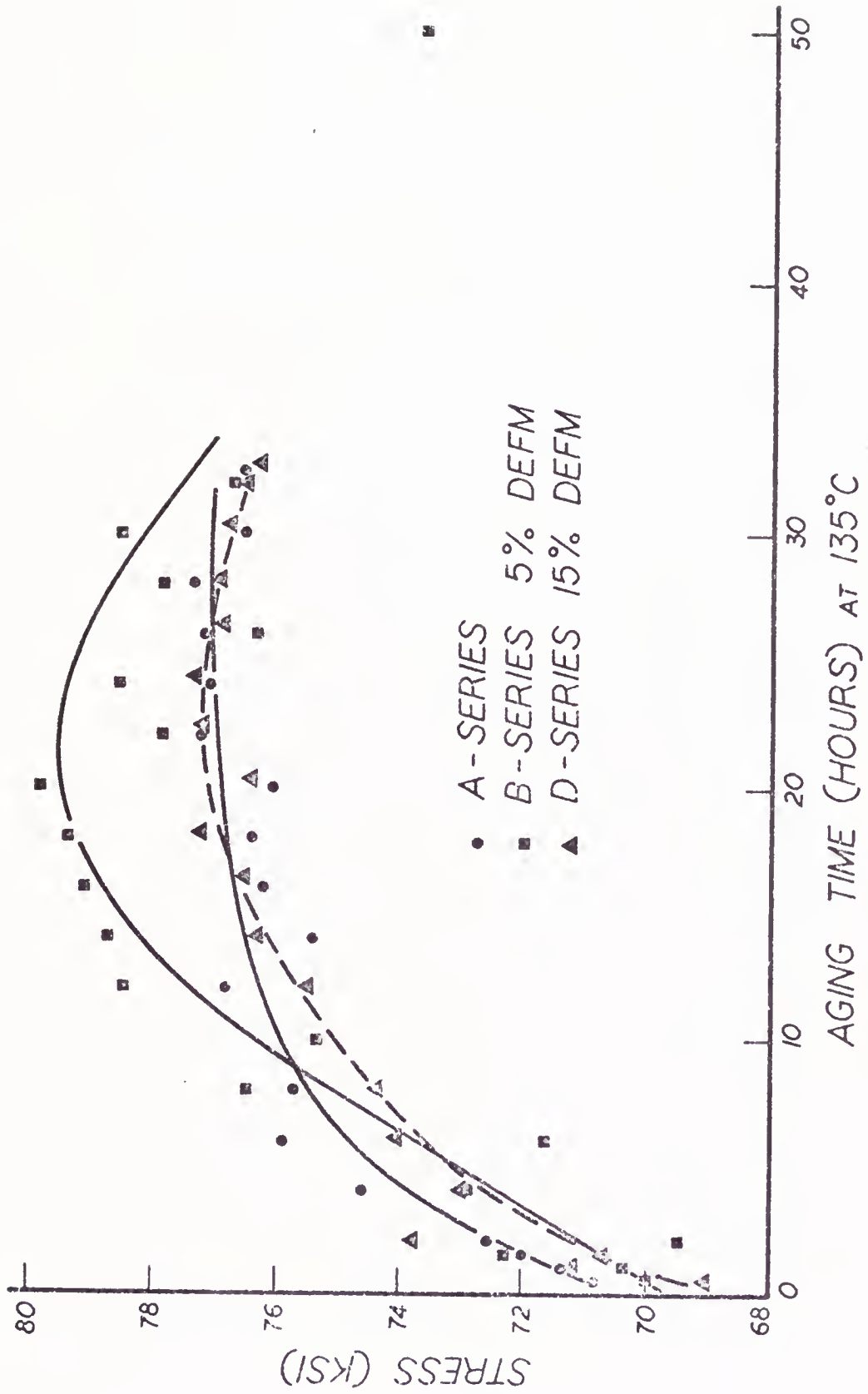


Figure 49. Results of Tensile Tests for A, B, D Series

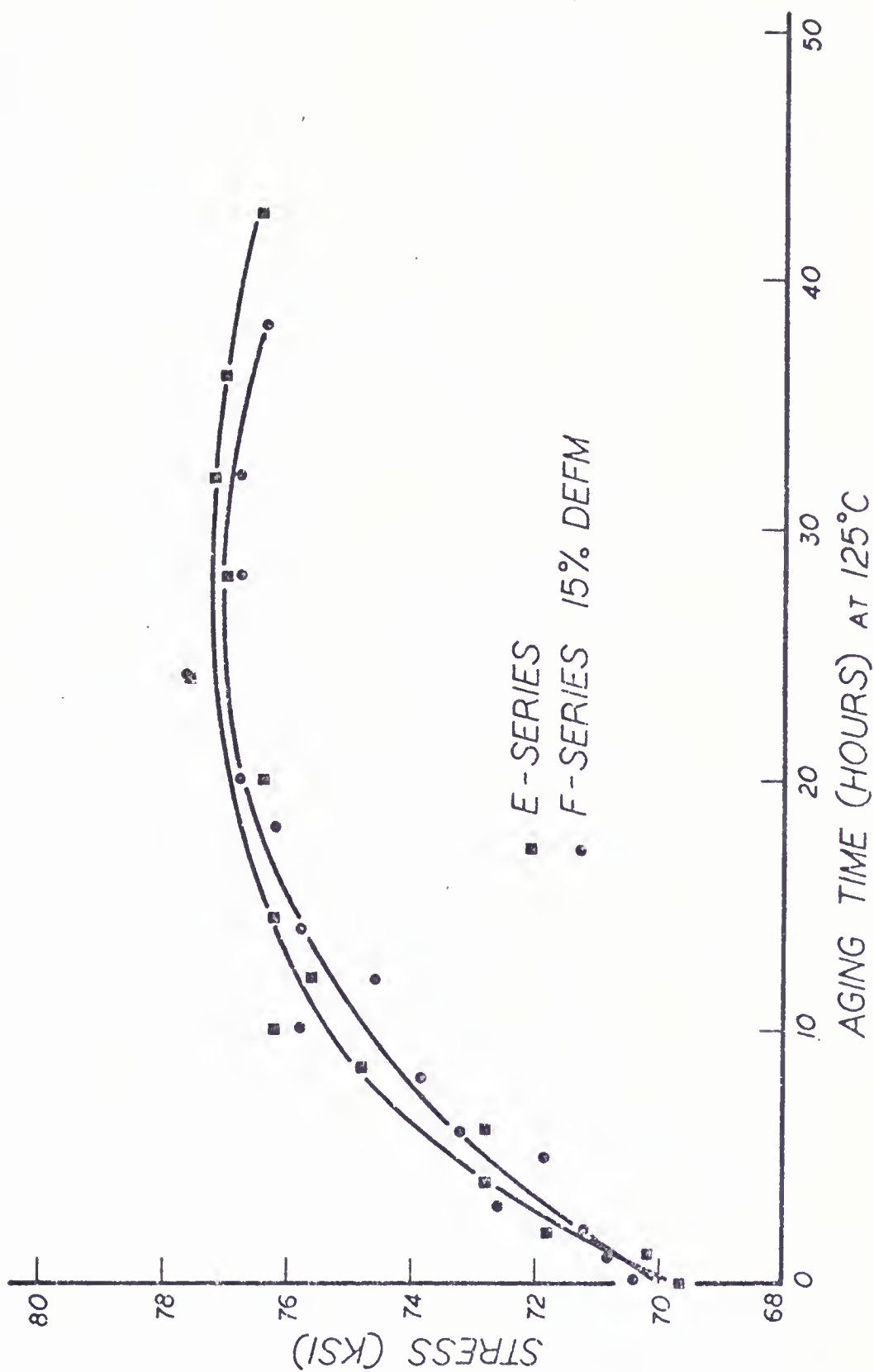


Figure 50. Results of Tensile Tests for E, F Series



Figure 51. Results of Tensile Tests for G, H Series

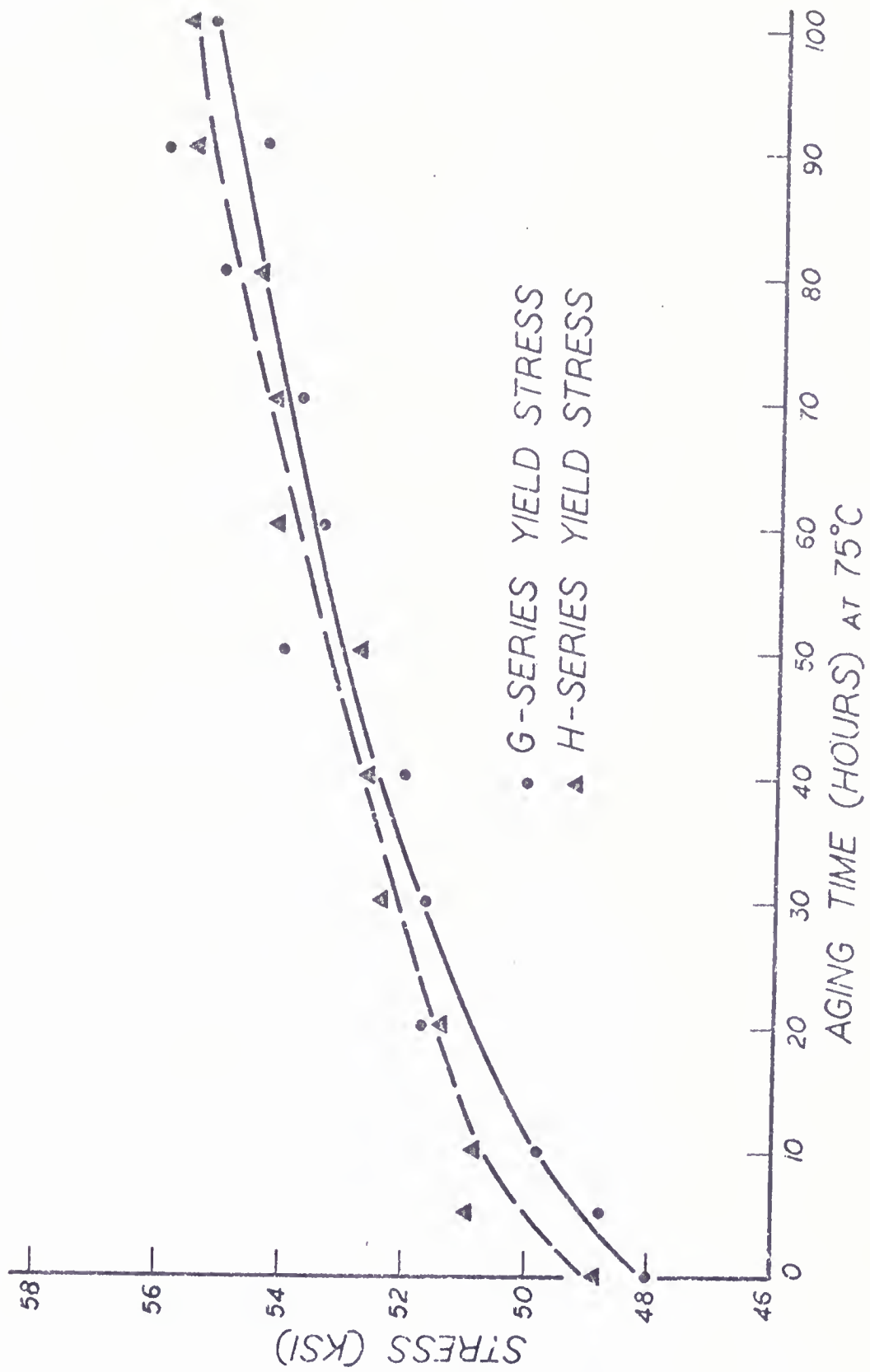
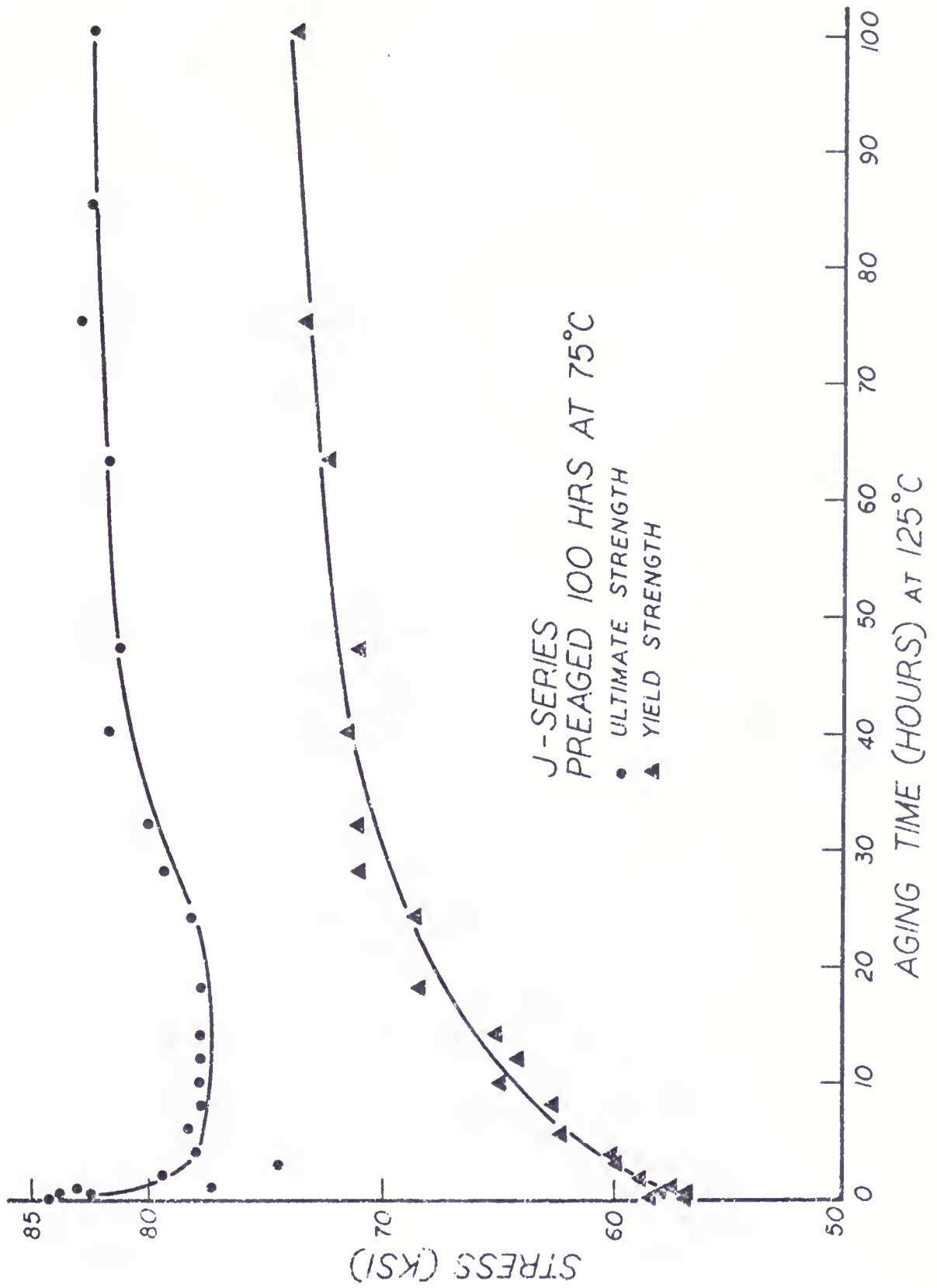


Figure 52. Results of Tensile Tests for J Series



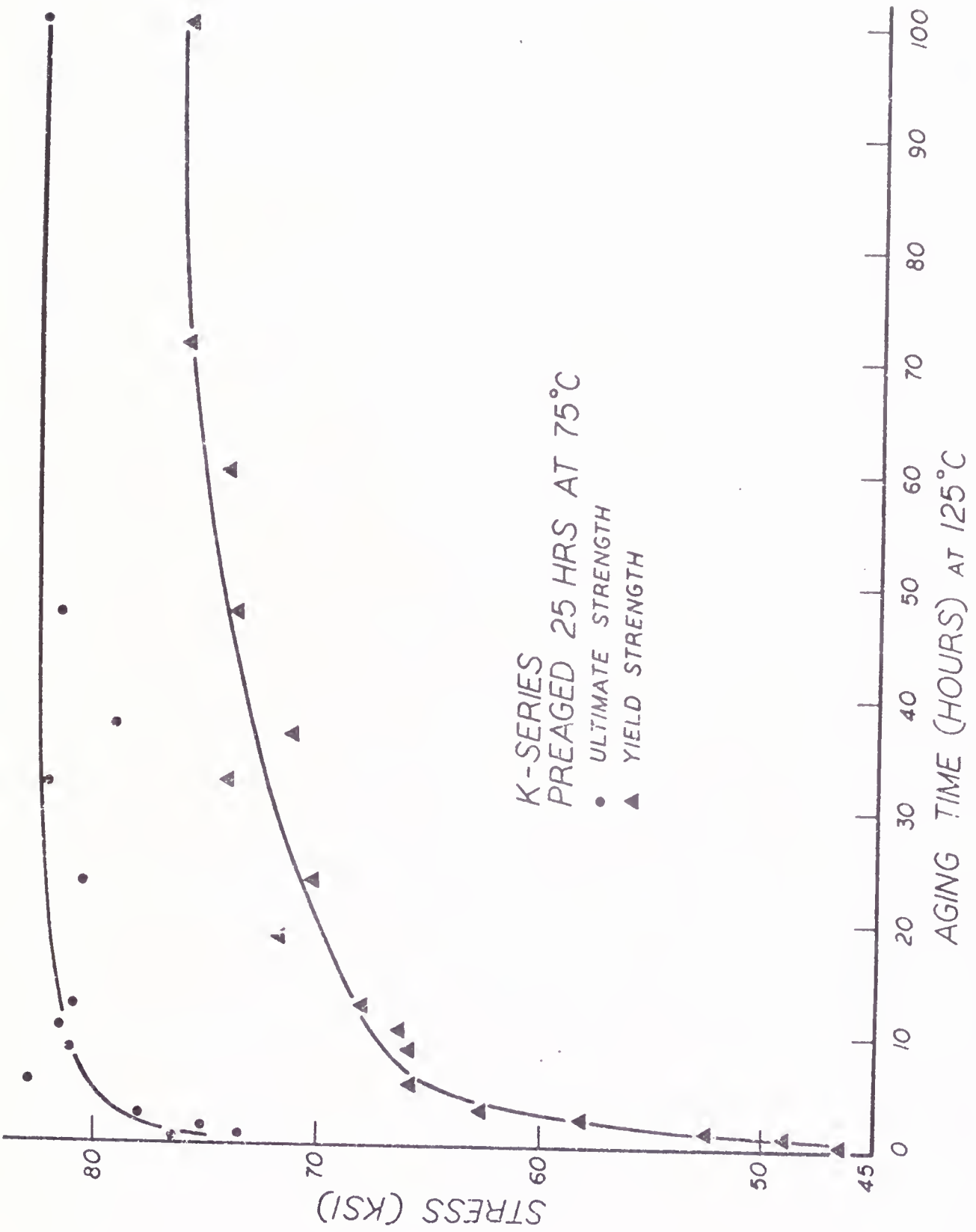


Figure 53. Results of Tensile Tests for K Series

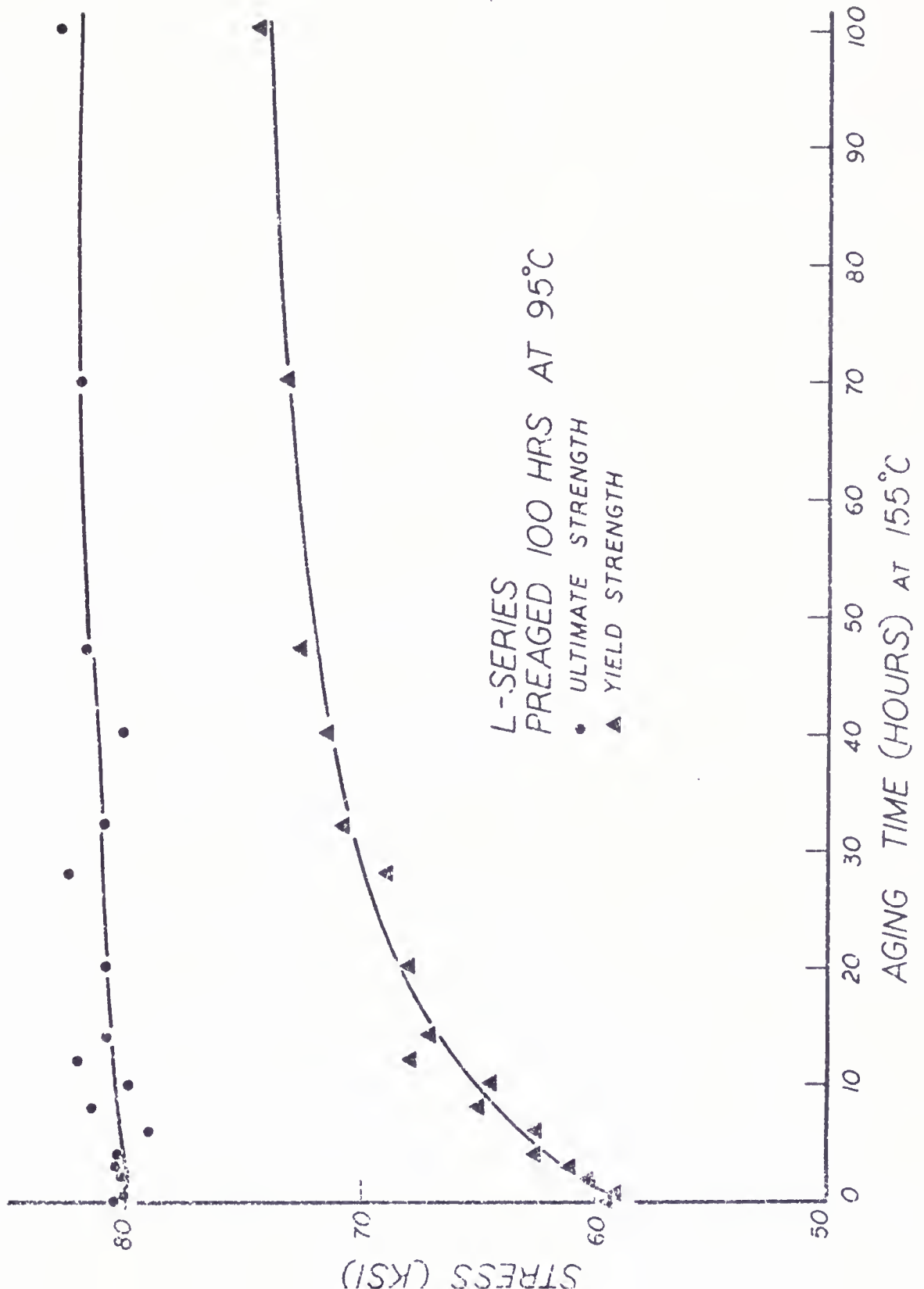


Figure 54. Results of Tensile Tests for L Series

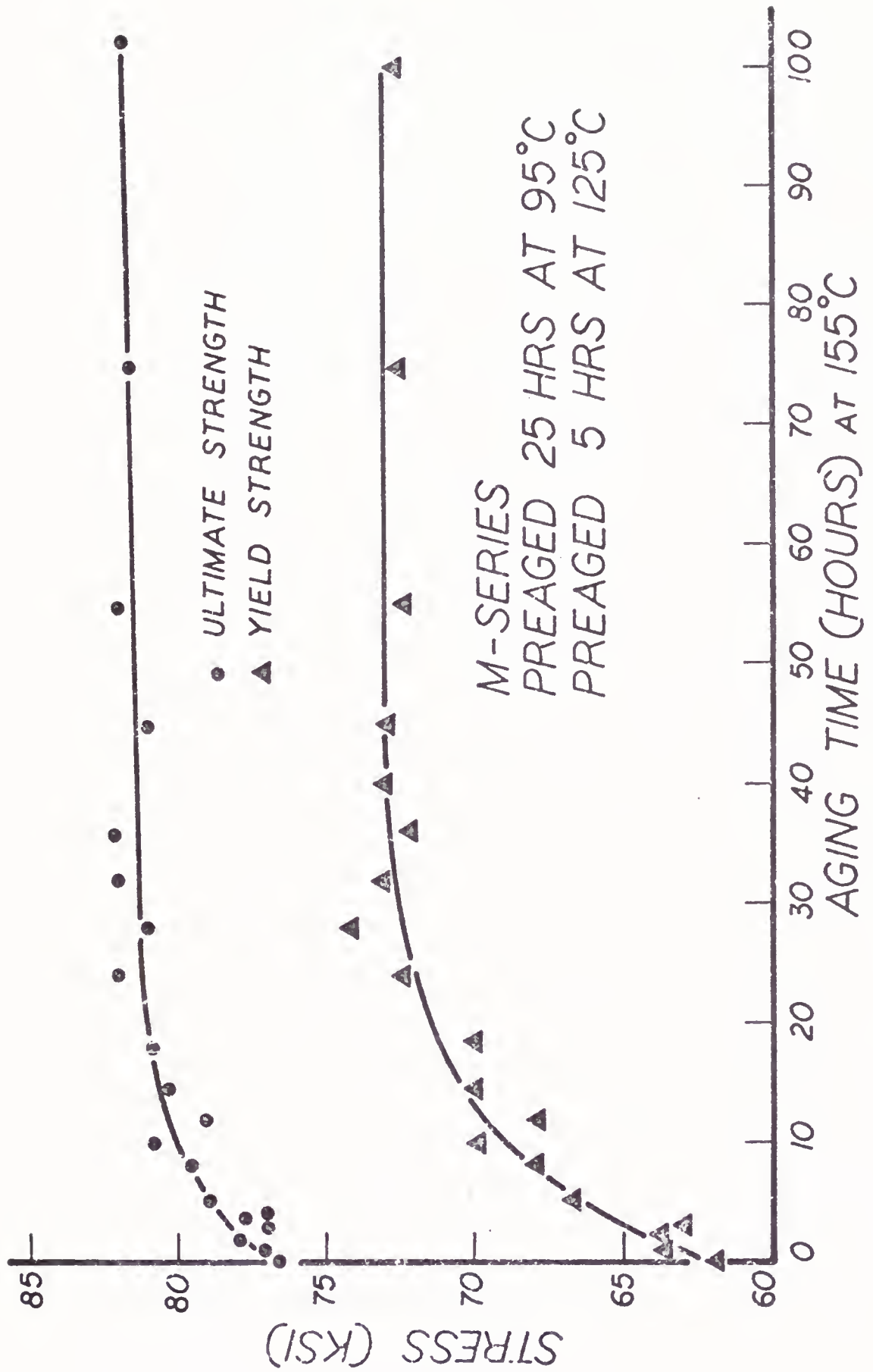


Figure 55. Results of Tensile Tests for M Series

early aging times, the small elastic strain fields associated with Mg-Zn clusters, and the lack of a very sharp interface between the matrix and particles at early aging times.

Metallography did show that the grain size remained approximately constant throughout the aging sequence.



## CHAPTER V

### DISCUSSION OF RESULTS

The discussion of the experimental results will be divided into two sections. The first of these will deal with the evolution of the particle parameters as measured by small angle scattering., and the effects of thermo-mechanical treatments and preage treatments on them. The second section will attempt to relate these particle size parameters to the mechanical properties of the alloys.

#### Small Angle X-Ray Scattering

Small angle scattering is the most appropriate technique for the study of preprecipitation, especially during early aging times, in the commercial Al-Zn-Mg system. These are several reasons for this. The lack of a sharp interface between the Guiner-Preston zones and the matrix has been confirmed at very early aging times by the absence of a -3 slope on a  $\ln I$  versus  $\ln \epsilon$  plot in the wings, or Porod region, of the scattering curve. This lack of interface definition coupled with the lack of resolution, and the extremely large number of particles, make the use of transmission electron microscopy highly

impractical. Assuming the resolution of the transmission electron microscope to be on the order of  $15 \text{ \AA}$  for Guinier-Preston zones in aluminum, and assuming a log normal distribution of spherical particles, an accurate determination of particle size distribution would require a mean particle diameter of approximately  $30 \text{ \AA}$ . The slow aging kinetics of the Al-Mg-Zn system do not yield values in this range until considerable aging has been done.

The high values of the migration activation energy,  $E_m$ , of approximately 1.0 eV is considerably higher than those obtained by several other workers. This value is over twice the value of .43 eV, obtained by Bohm and Gerold<sup>75</sup> for zinc-vacancy complexes in binary aluminum 4.7 to 8.6 atomic % zinc alloys. Bossac and Loffler<sup>32</sup> obtained identical values for zinc-vacancy complexes as Gerold, but extended their analysis into the ternary Al-Zn-Mg system. These authors obtained a value of .74 eV for the migration energy of magnesium-vacancy complexes, and .59 eV for zinc-magnesium complexes. Both Bossac and Loffler<sup>32</sup> and Ceresara and Fiorini<sup>37</sup> obtained an activation migration energy of .67 eV for ternary complexes in ternary aluminum alloys ranging from 2.2-5.0 weight % zinc and 1.05-3.5 weight % magnesium alloys. The even higher value of 1.0 eV obtained in this study would indicate that

the complexes are even more complicated. The increased complexity may be the result of copper being introduced into the zinc-magnesium-vacancy complexes. The large size and difficulty of diffusion of such complexes would require a considerably larger activation migration energy. The particle size distribution's radius of maximum abundance corresponding to the aging times at peak resistance was determined to be on the order of  $8 \text{ \AA}$ . Panseri and Federighi<sup>34</sup> determined the maximum in the resistance to be due to electron reflections from particles of  $9 \text{ \AA}$  radius for aluminum-zinc alloys with small percentages of magnesium.

The early rapid growth of the zones is due, for the most part, to the removal of solute atoms from the solid solution. This growth is not a redistribution process between previously nucleated zones, but is actually an increase in the volume fraction of scattering particles, as evidenced by the corresponding increase in the integrated intensity. By comparison with a binary aluminum-zinc alloy, it was determined that the initial volume fraction of zones in the as-quenched state was approximately 2%. Gerold has shown that the volume fraction measured at any time,  $t_1$ , can be calculated by a ratio of the integrated intensities and the final equilibrium volume fraction as:

$$f_{t=t_1} = \frac{Q_{t=t_1}}{Q_{t=\infty}} f_{t=\infty}$$

where:  $f_{t=t_1}$  is the volume fraction at a given time

$f_{t=\infty}$  is the volume fraction at equilibrium

$Q_{t=\infty}$  is the integrated intensity at equilibrium

$Q_{t=t_1}$  is the integrated intensity at a given time

The use of this direct ratio and the integrated intensity changes observed would indicate a volume fraction of scatterers between 4 and 5% in the equilibrium condition for the Al-Zn-Mg of this study. The high activation migration energy measured in the Al-Zn-Mg alloy of this research is also partially verified by the long aging times necessary to achieve a constant volume fraction of particles. In the direct aged series, the change in the integrated intensity indicates that it takes up to 8 hours at 135°C for the volume fraction to reach equilibrium, and even 100 hours aging at 75° and 95°C does not produce the equilibrium volume fraction, due to the slow kinetics of this system at these temperatures. The preaged samples reach the equilibrium volume fraction faster, but still require approximately 4 hours at the elevated temperature (125°-155°C). Mechanical treatment initially accelerated the rate of change of the integrated intensity, which would indicate that the dislocation motion aided in the removal

of solute atoms from solid solution, and also the motion of very small complex clusters. The equilibrium value of the integrated intensity did not, however, seem to be a function of mechanical treatments (see Figures 42 through 44). The long times to reach the equilibrium volume fraction of scatterers greatly differ from the simple binary aluminum zinc system where this equilibrium is obtained upon quenching or after only a few minutes of aging.

A general statement concerning the effect of mechanical treatment on the kinetics of the particle growth rate will summarize much of the results. Mechanical treatment greatly increases the initial aging rate, but the growth rate is arrested at much shorter aging times. This is confirmed by several different experiments. Fixed angle scattering measurements (see Figure 13) show that the deformed samples initially yield a higher small angle scattering intensity, but level off much sooner, and the undeformed sample actually yields a higher small angle scattering intensity after long aging times. The particle size distributions generated by the small angle scattering curves confirm that the mean particle size grows rapidly during the initial stages of aging in the mechanically treated samples, but after approximately one day of aging at 135°C, growth essentially stops. The undeformed

samples show a slower initial particle size growth, but continue growing for longer times, and actually reach larger sizes. This confirms the work of Ceresara and Fiorini,<sup>37</sup> who concluded from their resistivity measurements, that only the initial kinetics of the aging process are changed, and not the actual aging sequence. They present as the cause for the initial rate increase the formation of divacancies during the deformation process. Divacancies are more mobile than single vacancies, which would account for the increased initial rate. The subsequent decrease of the aging rate can be explained by the increased dislocation density generated by the deformation. The dislocations will act as vacancy sinks and greatly decrease the vacancy concentration. When the excess vacancy concentration is reduced to approximately that of the equilibrium concentration, the aging rate becomes controlled by normal diffusion in the matrix.

Preaging the samples at a low temperature (75° and 95°C) had a marked effect on the kinetics and transformations of the system. Preaging at low temperatures produced a narrower particle size distribution than the directly aged samples. Preaging at a low temperature does not produce as large a particle mortality, i.e., where the smaller particles redissolve in favor of the larger ones,

as does direct aging. This is evidenced by the presence of the characteristic particle interference shoulder (see Figures 14 and 15) in the scattering curves of the preaged samples and not on the direct aged samples. Particle growth during the low temperature preage is mostly due to the removal of solute atoms from solid solution. Growth of particles on direct aging is the result of both the removal of solute atoms from solid solution as well as the growth of larger nucleated clusters at the expense of smaller nucleated zones. The growth of a large number of particles of a very narrow distribution means that these particles will be, for a large part, stable with respect to each other. This existence of a more nearly monodisperse particle distribution at the start of final aging would greatly retard the kinetics of the redistribution process. This theory is confirmed by the growth rates of the low temperature preaged series (see Figures 19 through 20). The initial, somewhat rapid growth rate experienced upon raising to the high temperature age is mainly the result of further solute atom removal from the matrix. This can be seen to be true as the integrated intensity increases during this same time period. After the initial growth period, the growth of the zones takes on a slow, almost constant rate. The distribution of these particles



remains far narrower than that of directly aged series, even for similar mean particle sizes. Shorter preage times, 25 hours as opposed to 100 hours, that produce a minimum critical particle size demonstrate faster growth rates. This is true for two reasons. First, the shorter preaging times result in the annealing out of fewer excess point defects, and second, the distribution will possess a larger number of particles than are below the critical radius that will redissolve in favor of the critically sized particles. The distribution, however, will remain fairly sharp throughout the process.

Bardhan and Starke<sup>27</sup> have shown that a critical particle radius exists in order for the Guinier-Preston zones to act as nucleation sites for the intermediate phase  $\eta'$ . For the directly aged series with wide particle size distributions, this would suggest that only a relatively few particles will reach this critical size, thus nucleating a relative small number of  $\eta'$  particles which will continue to grow and coarsen at the expense of the smaller zones. In the case of a narrow size distribution, many more  $\eta'$  particles will be nucleated as a greater number of zones will reach the critical size at approximately the same time. The consequence of the greater number of critically sized zones that can serve as nu-



cleation sites for  $\eta'$  should be a much finer precipitate structure which would be slow to overage.

Employing calorimetric techniques, Asano and Hirano<sup>20-21</sup> have shown that Guinier-Preston zones dissolve before the formation of  $\eta'$  for short aging times. For longer aging times at lower temperatures, the dissolution of the zones is coincident with the formation of  $\eta'$ . This is in agreement with the results of this study that indicate that the Guinier-Preston zones formed during the low temperature preaging remain stable at the elevated temperature until a critical zone size is attained.

There were three aging sequences observed in this study as evidenced by both the small angle scattering and wide angle diffraction.

Solid Solution  $\rightarrow \eta$

Solid Solution  $\rightarrow \eta' \rightarrow \eta$

Solid Solution  $\rightarrow$  spherical G.P. zones  $\rightarrow \eta' \rightarrow \eta$

The results of the Guinier de Wolff investigation indicate that there exists low percentages of small  $\text{MgZn}_2$  particles in the as-quenched condition. The presence of the quenched-in precipitate was not eliminated even by solution heat treating for 12 hours at  $460^\circ\text{C}$ . For this reason, the precipitate was assumed to nucleate from large clusters on quenching. The presence of diffuse maxima in

the vicinity of the  $\text{MgZn}_2$  lines indicate the presence of some transition phase  $\eta'$  in the quenched material. On high temperature ( $125^\circ\text{C}$ - $135^\circ\text{C}$ ) direct aging, the  $\eta'$  lines shifted throughout the aging, and the  $\eta$  lines sharpened. Direct aging at low temperature produced no appreciable changes in the wide angle diffraction patterns. The pre-aged series produced a slight sharpening of the  $\text{MgZn}_2$  lines initially, then no major changes occurred until aging times of 24 hours or more at high temperature. This difference shows that the nucleation and growth of  $\eta'$  and growth of  $\eta$  occurring in the direct higher temperature age can be largely arrested by preaging at lower temperatures.

The wide angle diffraction also showed no evidence of scatter at the base of the Bragg peaks. The significance of this is that the Guinier-Preston zones are not producing large coherency strains with the matrix. The absence of this size effect is due to the counter balancing effects of magnesium and zinc. Magnesium concentration will enlarge the aluminum lattice, while zinc will decrease the lattice parameter. The absence of the size effect indicates that the clustering is a complex mixture of magnesium with zinc, and probably copper as well. This result corresponds to the findings of Tomita et al.,<sup>17</sup> who

have shown that the size effect, which eventually leads to a zone shape change, effectively vanishes at 1 atomic % magnesium concentrations.

The stress-strain curves for the preaged samples differed greatly from those of the samples aged directly at high temperature. The preaged samples demonstrated the occurrence of Type B serrated flow similar to that found by Reed-Hill<sup>90</sup> for 6061 aluminum. Figure 56 shows the characteristics of a load-time diagram for a specimen demonstrating Type B serrated flow. This phenomenon occurred at room temperature and a strain-rate of .02 inches per inch. This behavior was absent for the high temperature (125°C-135°C) directly aged samples. Under these conditions, the directly aged samples demonstrated a characteristic load-time curve similar to that of pure aluminum displaced to higher load values.

Type B serrated flow has been shown to be due to the nucleation of a Lüders band that remained pinned and did not propagate over the gage length of the specimen. The regions of smooth flow separating the packets of serrated flow are due to the propagation of the Lüders band over a restricted length, or the transverse propagation of a Lüders band.<sup>90</sup> Failure of the specimens usually occurred with little necking during the nucleation of one of the Lüders band, as evidenced by the load drop.

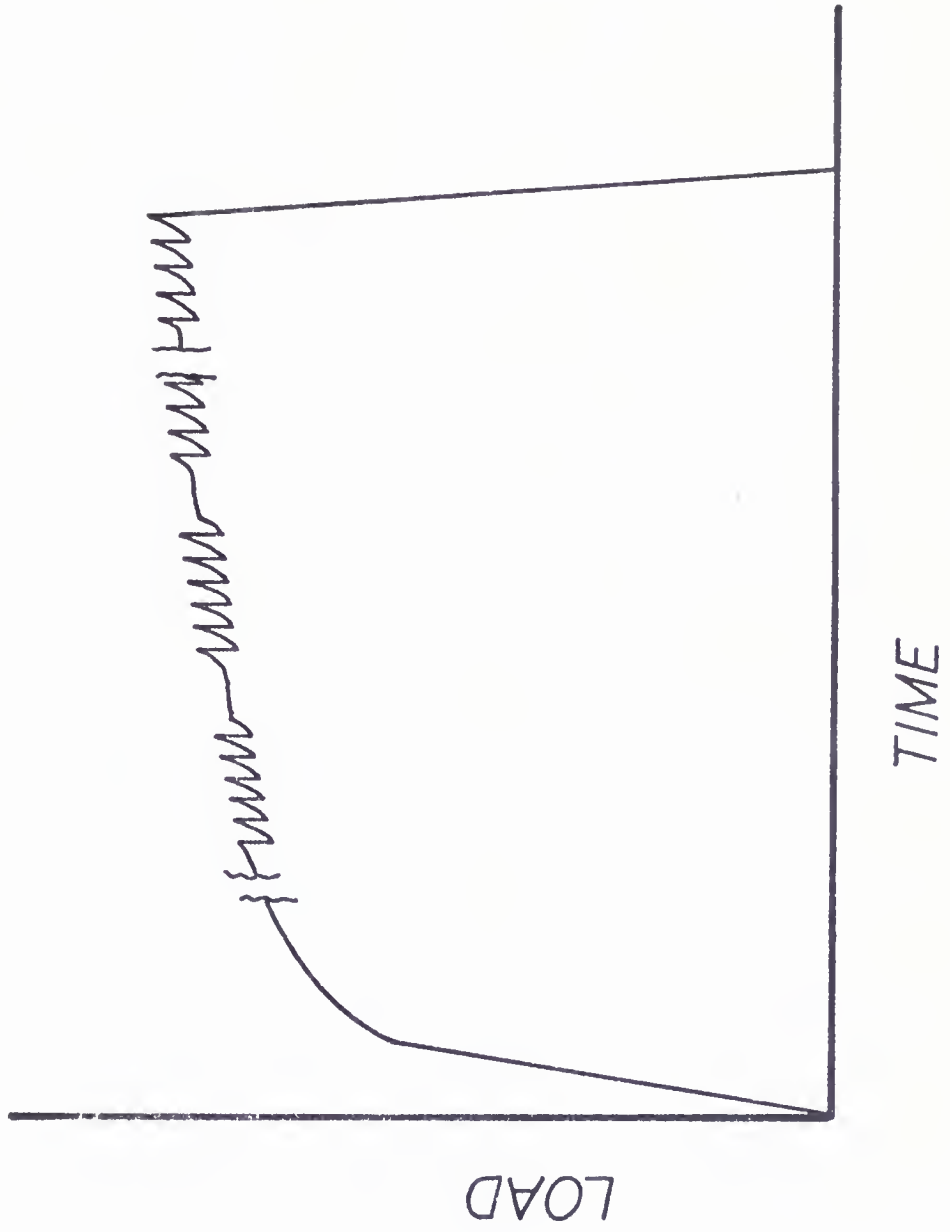


Figure 56. Schematic Representation of Type B Serrated Flow

The ultimate tensile strength of the preaged series remained essentially constant during the final age, while the yield strength increased greatly. Both the yield stress and the ultimate tensile strength increased during aging, approximately in a parallel manner for the directly aged samples. In order to understand the strengthening effect of the Guinier-Preston zones, a brief discussion of a few of the strengthening mechanisms will be presented.

The first proposed mechanism to be discussed will be that of Mott and Nabarro<sup>93</sup> who have proposed that the strengthening effect of the Guinier-Preston zones is due to the mismatch between the zones and the matrix. This effect will result in coherency stress in the region surrounding the zone, and will impede the passage of dislocations. Figure 57 shows the interaction of a dislocation line with the region of coherency strain surrounding a zone. This strengthening mechanism has little applicability to the aluminum-zinc-magnesium system. It has already been shown by the absence of the size effect scattering at the base of the Bragg peaks that no large mismatch exists between the matrix and the zones.

A second strengthening mechanism possible would be that of the creation of new interfacial area during the passing of a dislocation through a zone. It has been pre-



Figure 57. Interaction of a Dislocation Line With the Coherency Strains Surrounding a Guinier-Preston Zone

sented previously that the clustering of magnesium and zinc is thermodynamically favored over either aluminum-zinc or aluminum-magnesium bonds. The minimum interfacial area between the magnesium-zinc clusters with the aluminum matrix would be accomplished by cluster spheres. In order for a dislocation to pass through a zone, it must create new zone-matrix interfacial area as shown in Figure 58. The increase in the number of unfavorable matrix zone bonds can only be accomplished by the expenditure of work which is proportional to the amount of area created. The amount of work necessary to pass a dislocation through the zone would then be

$$W = \gamma_s dA$$

where  $\gamma_s$  is the interfacial energy and  $dA$  is the area created by the dislocation. Harkness<sup>91</sup> has shown that for spherical particles, the work per dislocation per particle is given by:

$$W = \gamma_s r^2 [\cos^{-1}(\frac{r-b}{r}) - r(r-b)] [1 - (\frac{r-b}{r})^2]^{1/2}$$

This theory would predict the strengthening effect to be a complex function of the number of particles, the particle size, and the volume fraction.

A third strengthening mechanism is that proposed by Hirsch and Kelly,<sup>92</sup> stacking fault strengthening. Disloca-

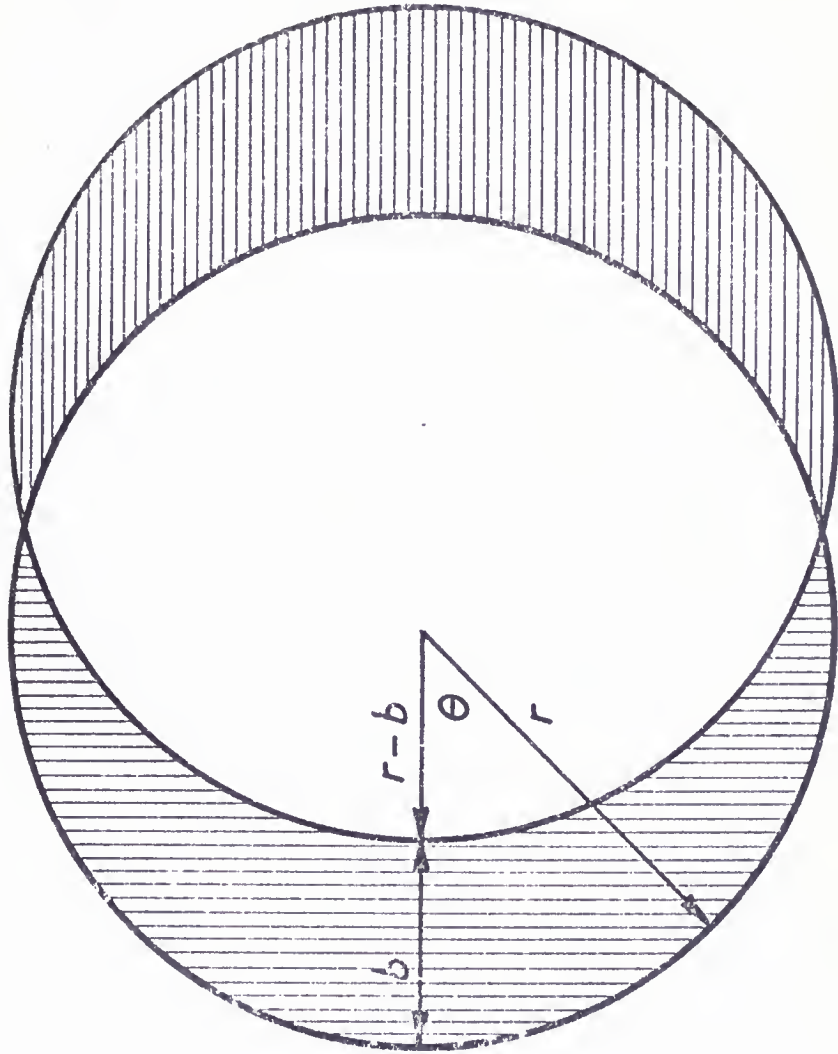


Figure 58. Representation of Area Created by Passing of a Dislocation Through a Guinier-Preston Zone, Along with the Applicable Geometry



tions in close-packed materials can dissociate into partial dislocations, and in doing so, produce a reduction in the total energy associated with the dislocation. When an alloy contains regions of solute clustering, dislocations will be either attracted to the clusters if the stacking fault energy is lower in the clusters, or the dislocations will be repelled if the stacking fault energy is higher than that of the matrix. Either case will raise the yield strength of the alloy. If the stacking fault energy is higher in the cluster, then it will require a greater force to bring the dislocation to the cluster. If the stacking fault energy is lower than the matrix, it will require a greater force to pull the dislocation away from the particle.

Work will also be done by the elastic forces between the partial dislocations when the partial dislocation spacing changes upon going from a region of one stacking fault energy to another. Hirsch and Kelly<sup>92</sup> have shown that the equilibrium spacing between partial dislocations is inversely proportional to the tension between the partials in the stacking fault. They have also shown that the change in energy  $\Delta E$  is given by:

$$\Delta E = K(\alpha) \ln \frac{\gamma_1}{\gamma_2}$$

where  $\gamma_1$  and  $\gamma_2$  are the partial dislocation tensions in each of the areas, and  $K(\alpha)$  is a force constant.

In the case of magnesium-zinc clusters in an aluminum matrix, the dislocations will be attracted to the particles. The structure of the aluminum matrix and the coherent matrix is face-centered cubic. The structure of a stacking fault in a face-centered cubic material is hexagonal. The equilibrium structure of magnesium-zinc in an aluminum matrix is hexagonal. This would indicate that the stacking fault energy within the coherent cubic zones would be lower than that in the matrix, and may even be negative as the stacking fault region will produce a hexagonal array, which is the equilibrium structure of the elements in the clusters and also the equilibrium phase ( $\eta$ ) of the clusters. This means that the dislocations will tend to remain within the zones, and the dislocation line will pass through as many zones as is possible, and that work must be done in order to force the partial dislocations back together to get the dislocation out of the zones.

This phenomenon also serves to explain the increased particle growth rate and enhanced transformation rate in the deformed series. The dislocations sweeping through the matrix will carry solute atoms with them. When defor-

mation stops, the dislocations will be pinned to as many zones as possible. The dislocations now act as diffusion short circuits for the solute atoms that the dislocation motion removed from the matrix, and produce an enhanced initial particle growth.

The fact that the transformation to the intermediate precipitate,  $\eta'$ , occurred more rapidly in deformed specimens is also explained by this theory. With the dislocations being pinned within many of the particles, a hexagonal region, the stacking fault itself, already exists, therefore the transition to the hexagonal intermediate structure is aided by the presence of the dislocations. Hirsch and Kelly<sup>92</sup> calculate that the maximum strengthening effect for the aluminum-silver system would be for zones approximately 30 Å radius. The results of this study indicate that the greatest strengthening effect for the 7075 alloy studied is about 2/3 this value.

The results of this study can explain the results obtained by the mechanical tests of Di Russo et al.<sup>69</sup> Di Russo showed that his T-AHA (solutionized T, preaged A, work hardened H, final age A) yielded greatly improved mechanical properties. The preage treatment of 6 hours at 105°C produces stable Guinier-Preston zones. The deformation after the preage takes advantage of the dislocations

being attached to the zones, thus producing another accelerated aging period. This sequence will produce a stable zone structure, and the deformation produces the accelerated kinetics necessary for commercial feasibility.

Ostermann and Reiman,<sup>86</sup> as well as Staley, Brown and Schmidt,<sup>44</sup> have worked on methods of producing nucleation sites for  $\eta'$ . Ostermann and Reiman present the advantage of mechanical treatments as the increased number of dislocations available for heterogeneous nucleation of  $\eta'$ . Staley et al.<sup>44</sup> have studied the addition of silver to the Al-Zn-Mg system which has been shown to act as nucleation sites for  $\eta'$ . Both of these processes are alternative methods of producing  $\eta'$  nucleation sites. A more homogeneous distribution of  $\eta'$  would be obtained by producing a stable critical size Guinier-Preston zone configuration. As G.P. zones are homogeneously distributed, a more homogeneous distribution as well as a greater number of particles would be produced by this method.

## CONCLUSIONS

The activation migration energy calculated from both resistivity measurements and small angle scattering results was approximately 1.0 eV. This value is higher than that obtained for ternary pure alloys. The explanation presented for this is the formation of more complex clusters in the commercial quaternary alloy, and specifically to the presence of copper.

The aging sequence in the 7075 alloy has been shown to be three-fold:

solid solution  $\rightarrow \eta$

solid solution  $\rightarrow \eta' \rightarrow \eta$

solid solution  $\rightarrow$  spherical G.P. zones  $\rightarrow \eta' \rightarrow \eta$

The phase  $(\text{Al,Zn})_{49}\text{Mg}_{32}$  is also present in the "as-quenched" state.

The results of this study have shown that mechanical treatments do not change the sequence of aging in a commercial 7075 alloy, but does, however, alter the aging kinetics as a result of the fact that dislocations are attracted to clusters, and act as preferred diffusion paths.

Preaging of the 7075 alloy produces a narrow particle

size distribution which remains stable at the higher final aging temperature. The particle size distribution produced by the low temperature preage remains a narrower distribution at the higher temperature of final aging, contrary to the zone size distributions produced by direct high temperature aging. The continued stable growth of the Guinier-Preston zones at high temperature produces a large number of zones that reach a critical size necessary to act as nucleation sites for  $\eta'$ . This critical size corresponds to approximately  $20 \text{ \AA}$  which is also the particle size corresponding to the maximum in tensile strength.

Mechanical treatment performed after a low temperature preage will produce a second period of accelerated aging, but will not greatly affect the stability of the zones produced at the low temperature preage. This is true only if the percent deformation is kept low (i.e.,  $\leq 15\%$ ) as higher deformation will result in high dislocation densities and drastic modifications of the zone structure.

Future work in this area should be directed toward optimization of several procedures found to be beneficial to the strengthening process. One of these factors would be the investigation of the highest possible preage temperature that would produce a narrow stable initial

Guinier-Preston zone distribution. This would enable the use of the shortest preage times necessary to make the procedure commercially feasible. A number of varying degrees of deformation should be applied to this preage treatment, along with several final aging temperatures, in order to optimize the entire process.

Several other properties of interest should also be investigated in conjunction with the optimized zone state. Stress corrosion cracking resistance as a function of the various zonal states should be investigated. The formation of a fine dispersion of the precipitate structure should greatly reduce the susceptibility of the alloy to stress corrosion cracking.

Further work along these lines using research pure alloys may not reproduce the conditions found in commercial alloys, as it has been shown that the kinetics of the commercial system are slower than those of research pure materials. For this reason, future work should be pointed toward the testing of actual commercial alloys.

## APPENDIX



## APPENDIX

Computer Program for Calculation of X-Ray Small  
Angle Scattering Parameters

The following program was written by Gould and Kirklin<sup>63</sup> for the analysis of small angle scattering data, and modified by Healey and Hill<sup>64</sup> to be applicable to the work performed in this study. Table 5 lists the variable names used along with their usual mathematic symbols. Table 6 lists the format of data input cards. This program will calculate the relative integrated intensity, the Guinier radius, the Porod radius, the radius of maximum abundance, and determine the particle size distribution of the particles assuming a log normal distribution.

Table 5

## List of Variable Names Used in SAXS Program

Symbol	Usual Mathematical Symbol	Equation or Description
NN	----	Number of data points
COUNT1(I)	----	Total counts from SAXS of back-ground sample
COUNT2(I)	----	Total counts from SAXS of sample
TIME1(I)	----	Counting time for COUNT1(I)
TIME2(I)	----	Counting time for COUNT2(I)
TITLE	----	Title or sample name
CENTR	----	Centroid
ELEV(I)	m	Elevation in microns
DELEV	----	Step size in microns
ABSF	----	Absorption factor
VOLF	f	Volume fraction
BINT(I)	I(s)	Intensity corrected for back-ground
ANGLE(I)	s	$s = \frac{E}{\lambda}$
ESSQ(I)	$s^2$	Angle squared
AREA	Q	$\int_0^{\infty} s \cdot I(s) ds = \frac{1}{2} s_1^2 I_1 + \sum_{i=2}^n s_i I_i(s) \Delta S_i +$ $\frac{S_o^3 I_o(s)}{sm}$
CKAREA(I)	$s \cdot I(s)$	
CKASYM(I)	$s^3 \cdot I(s)$	Test for Porod region

Table 5 - continued.

Symbol	Usual Mathematical Symbol	Equation or Description
ZZ	----	Start of Guinier region in radians
QQ	----	End of Guinier region in radians
ASYMPT	$s_0^3 \cdot I_0(s)$	$s \lim_{s \rightarrow \infty} (s^3 I(s))$
SLOPE(I)	$\frac{d(\ln I(s))}{d \ln s}$	Porod's law $\lim_{s \rightarrow \infty} \frac{d \ln(I(s))}{d \ln s} = -3$ (for a beam of line cross section)
GUIN(I)	$\frac{5}{4\pi^2} \left( -\frac{d \ln I(s)}{ds} \right)^{\frac{1}{2}}$	The Guinier slope $I(s)_i = n^2 V^2 \exp[-\frac{4\pi^2}{5} a_i^2 s_i^2]$ and $GUIN(I) \equiv a_i$
GUINR	$R_G$	The Guinier radius, from least squares calculation of $a_i$
CONST	$n(n^2 V^2)$	
A(I)	$\left( \frac{\ln X - \ln \mu}{\sqrt{2} \ln \sigma} \right)^2$	$P(x) = \frac{1}{\sqrt{2\pi} X \ln \sigma} \exp \left[ -\left( \frac{\ln X - \ln \mu}{\sqrt{2} \ln \sigma} \right)^2 \right]$
B(I)	$\sqrt{2\pi} X \ln \sigma$	$P(x) = \frac{1}{\sqrt{2\pi} X \ln \sigma} \exp \left[ -\left( \frac{\ln X - \ln \mu}{\sqrt{2} \ln \sigma} \right)^2 \right]$
XRAD(I)	X	$P(x) = \frac{1}{\sqrt{2\pi} X \ln \sigma} \exp \left[ -\left( \frac{\ln X - \ln \mu}{\sqrt{2} \ln \sigma} \right)^2 \right]$
POPUL(I)	P(x)	Population
AUGR	$\mu$	Mean
SIGMA	$\sigma$	Standard deviation

Table 5 - continued.

Symbol	Usual Mathematical Symbol	Equation or Description
HIGHR	----	$\log R' = \log \mu + \log \sigma$
SMALR	----	$\log R' = \log \mu - \log \sigma$
RADMAX	----	Radius of maximum abundance evaluate $x$ @ $\frac{dP(x)}{dx} = 0$
X(I)	$s^2$	$I = \frac{8\pi a^3 f^2 V}{1 + 4\pi^2 s^2 a^2}$
Y(I)	$I^{-1/2}$	$I^{-1/2} = \frac{4\pi^2 s^2 a^{1/2}}{(8\pi f^2 V)^{1/2}} + \frac{1}{(8\pi f^2 V)^{1/2} a^{3/2}}$
SLOAP	M	$\frac{4\pi^2 a^{1/2}}{(8\pi f^2 V)^{1/2}}$
ZERO	B	$\frac{1}{(8\pi f^2 V)^{1/2} a^{3/2}}$
DEBYE	a	$\frac{1}{2\pi} \sqrt{\frac{M}{B}}$
SPHERE	$a_s$	a evaluated @ $\gamma(r) = 0.312$
D(I)	r	$\gamma(r) = \exp\left(-\frac{r}{a}\right)$
CORRL(I)	$\gamma(r)$	$\gamma(r) = \exp\left(-\frac{r}{a}\right)$

Table 6

## Data Input for SAXS Program

Card	Columns	Format	Explanation
1	1-60	15A4	TITLE OR SAMPLE NAME
2	1-4	I4	NN - THE NUMBER OF DATA POINTS (i.e., 90 points = 0090)
3	1-10	5F5.4	ZZ, QQ START AND END OF GUINIER RE- GION IN RADIANS
4	1-50	10F5.0	TOTAL COUNTS FROM BACKGROUND SAMPLE 10 points to a line
5	1-50	10F5.2	TOTAL COLLECTING TIME FOR BACK- GROUND COUNTS 10 points to a line
6	1-50	10F5.0	TOTAL COUNTS FROM SAXS OF SAMPLE 10 points to a line
7	1-50	10F5.2	TOTAL COLLECTION TIME FOR SAMPLE SAXS 10 points to a line
8	1-5	F5.0	EVEL(1) - HEIGHT OF FIRST DATA POINT IN MICRONS
	5-10	F5.0	CENTR - CENTROID IN MICRONS
	11-15	F5.0	DELEV - STEP SIZE IN MICRONS
	16-20	F5.0	ABSF - ABSORPTION FACTOR
	21-25	F5.0	VOLF - VOLUME FRACTION

```

C SMALL ANGLE X-RAY RESULTS FOR NO RADIATION
C SAXS PARAMETERS ARE CALCULATED FROM ELEVATIONS AND COUNTS FOR
C SAMPLE TO REGISTRATION PLANE DISTANCE OF 215 MILLIMETERS. COUNT1
C IS FOR REFERENCE BACKGROUND SCATTERING, COUNT2 IS SAMPLE
C SCATTERING, ABSF IS THE ABSORPTION FACTOR TO CORRECT BACKGROUND. T IS
C TRANSMITTED INTENSITY BY BACKGROUND TRANSMITTED INTENSITY. VOLF IS
C THE VOLUME FRACTION OF PARTICLES.
C
      DIMENSION ELEV(300), COUNT1(300), COUNT2(300), COUNT2(300), BINT(300),
      IANGLE(300), ESSQ(300), CKAREA(300), CKASY1(300), SLOPE(300), GUINT(300
      2), A(300), B(300), XRAD(300), POPUL(300), X(50), Y(50), D(300), CORRLL(300)
      3, TIME1(300), TIME2(300), TIME3(300), GRAPH(1500), TITLE(15), XE(300), H
      4E(300), ES(300)
C
      4 READ(5,108) TITLE
      108 FORMAT(15A4)
      READ(5,109) HN
      109 FORMAT(I4)
      READ(5,217) ZZ,QQ

```

```

217  FORMAT(5F5.4)
      READ(5,855) (COUNT1(I),I=1,NN)
      READ(5,856) (TIME1(I),I=1,NN)
      READ(5,855) (COUNT2(I),I=1,NN)
      READ(5,856) (TIME2(I),I=1,NN)

855  FORMAT(10F5.0)
856  FORMAT(10F5.2)

      READ(5,116) ELEV(1),CENTR,DELEV,ABSF,VOLF

116  FORMAT(5F5.0)

C
C  COMPUTE ALL ELEVATIONS FROM STEP SCANNER PROGRAM
C
      DO 6 I=2,NN
        ELEV(I)=ELEV(I-1)+DELEV
        6  CONTINUE
C
C  CALCULATE SAXS VARIABLES AND TRIAL VALUES OF PARAMETERS
C
      DO 10 I=1,NN

```

```

BINT(I)=COUNT2(I)/TIME2(I)-(COUNT1(I)*ABSF)/TIME1(I)
ANGLE(I)=(ELEV(I)-CENTR)/(.7107*.215E6)
ESSQ(I)=ANGLE(I)**2 *10000.
CKAREA(I)=ANGLE(I)*BINT(I)
10 CKASYM(I)=ANGLE(I)**3*BINT(I)*1000
C
DO 15 I=3,NN
IF(BINT(I-2)-BINT(I))12,12,14
12 GOINT(I)=0
GO TO 15
14 COUNT(I)=SQRT(5.0*ALOG(BINT(I-2)/BINT(I)))/(4.0*3.1416*3.1416*(ANGL
1E(I)**2-ANGLE(I-2)**2))
15 CONTINUE
C
C CALCULATE GUINIER RADIUS BY LEAST SQUARES METHOD
C
FIRI=0
NI=0
SUMIX=0

```



```

SUMY=0
SUMXSQ=0
SUMXY=0
DO 20 I=1,NN
IF (ANGLE(I).LE.ZZ) GO TO 20
IF (MIN(EQ,0) MIN=I
IF (ANGLE(I).GT.QQ) GO TO 20
SUMX=SUMX-7.8957*ESSQ(I)*1.0E-04
SUMY=SUMY+ALOG(BINT(I))
SUMXSQ=SUMXSQ+62.342*ESSQ(I)**2*1.0E-08
SUMXY=SUMXY-7.8957*ESSQ(I)*ALOG(BINT(I))*1.0E-04
N=N+1
20 CONTINUE
GUEHR=SQRT((N*SUMXY-SUMX*SUMY)/(N*SUMXSQ-SUMX**2))
CONST=EXP((SUMY*SUMXSQ-SUMX*SUMXY)/(N*SUMXSQ-SUMX**2))
N=0
SHASYI=0
LAST=NN
DO 25 I=3,NN

```

```

SLOPE(I)=ALOG(BINT(I-2)/BINT(I))/ALOG(ANGLE(I)/ANGLE(I-2))
IF(SLOPE(I).LT.2.55) GO TO 25
IF(SLOPE(I).GT.3.45) GO TO 25
IF(I.GT.LAST) GO TO 25
LAST=I+1
SNASYM=SNASYM+CKASYM(I)
M=M+1
25 CONTINUE
ASYMPT=SNASYM/M*0.001
C
C WRITE SAXS VARIABLES DETERMINED FROM RAW DATA
C
WRITE(6,120) TITLE
120 FORMAT(1H1,15A4)
WRITE(6,125)
125 FORMAT(1H0,5HINDEX,3X,7HGUINIER,2X,9HINTENSITY,2X,12HRADIANS/ANG.,
12X,9HANGLE-SQ.,3X,3HS*1,5X,7HASYMPT.,3X,5HEXPM)
WRITE(6,130)(I,GUIHT(I),BINT(I),ANGLE(I),ESSQ(I),CKAREA(I),CKASYM(
11),SLOPE(I),I=1,M)

```

```

130 FORMAT(1H ,13,4X,F8.3,2X,F8.2,4X,F8.6,5X,F8.4,2X,F7.4,2X,F8.5,2X,F
17.4)
CALL PLOT2(GRAPH,9.04,9.0,5.0,0.0)
CALL PLOT3(1H*,ANGLE(1),BINT(1),NN)
WRITE(6,9)
9 FORMAT(1H1)
CALL FPLOT4(9,9HINTENSITY)
C
WRITE(6,121) TITLE
DO 166 I=1,NN
XE(I)=ALOG(BINT(I))
166 CONTINUE
CALL PLOT2(GRAPH,3.,0.0,1.8,-2.2)
CALL PLOT3(1H*,ESS0(1),XE(1),NN)
WRITE(6,9)
CALL FPLOT4(13,13HLOG INTENSITY)
C
WRITE(6,121) TITLE

```

```

121  FORMAT(1H0,15A4)
C
      ZMIN=(ZZ**2)*10000
      OMAX=(OO**2)*10000
      WRITE(6,87)ZMIN,OMAX
27  FORMAT(5HZMIN=,F10.4,5HOMAX=,F10.4)
C
      JT=80
C
      CALL PLOT2(GRAPH,.6,0.0,1.6,0.0)
      CALL PLOT3(1H*,ESSQ(1),XE(1),JT)
      WRITE(6,9)
      CALL FPLOT4(13,13HLOG INTENSITY)
C
      WRITE(6,121) TITLE
C
      DO 237 I=1,NN
      ES(I)=ALOG(ANGLE(I))
237  CONTINUE

```

```

C
CALL PLOT2(GRAPH,-3.0,-7.0,1.6,-2.4)
CALL PLOT3(1H*,ES(1),XE(1),NN)
WRITE(6,9)
CALL FPLLOT4(13,13HLOG INTENSITY)

C
WRITE(6,121) TITLE

C
C ADJUST INTENSITY TO CORRESPOND TO GUINIER AND POROD APPROXIMATIONS
C COMPUTE AREA AND ASYMPTOPE FROM ADJUSTED INTENSITIES
C CALCULATE POROD RADIUS FROM ADJUSTED AREA AND ASYMPTOPE

C
DO 301=LAST,NN
  BINT(1)=ASYMPT/ANGLE(1)**3
  CKAREA(1)=ANGLE(1)*BINT(1)
30 CKASYM(1)=ANGLE(1)**3*BINT(1)*1000.

DO 351=1,MIN
  BINT(1)=CONST*EXP(-7.8957*(GUINR*ANGLE(1))**2)
  CKAREA(1)=ANGLE(1)*BINT(1)

```

```

35 CKASYM(1)=ANGLE(1)**3*BINT(1)*1000.
   DO 50 I=3,NN
      IF( BINT(1-2)-BINT(1)) 48,48,49
48 GUNT(1)=0
      GO TO 50
49 GUNT(1)=SQRT(5.0*ALOG(BINT(1-2)/BINT(1)))/(4.0*3.1416*3.1416*(ANGL
      1E(1)**2-ANGLE(1-2)**2)))
50 CONTINUE
C
C DETERMINE AREA BY TRIANGULATION TO ORIGIN OF FIRST POINT AND POROD
C APPROXIMATION FROM FINAL POINT. INTERIOR POINTS BY SUMMATION OVER
C ANGLE INCREMENTS
C
      M=0
      SMASYM=0
      DO 45 I=3,NN
         SLOPE(1)=ALOG(BINT(1-2)/BINT(1))/ALOG(ANGLE(1)/ANGLE(1-2))
         IF(SLOPE(1).LT.2.55) GO TO 45
         IF(SLOPE(1).GT.3.45) GO TO 45

```

```
SMASYM=SMASYM+CKASYM(I)
```

```
M=M+1
```

```
45 CONTINUE
```

```
ASYMPT=SMASYM/M*0.001
```

```
C
```

```
LL=NN-2
```

```
MM=NN-1
```

```
AREA=0.5*ANGLE(1)*CKAREA(1)+ASYMPT/ANGLE(NN)
```

```
DO 40 I=1,MM
```

```
40 AREA=AREA+CKAREA(I)*(ANGLE(I+1)-ANGLE(I))
```

```
C
```

```
POROD= 3.0*AREA/(8.0*(1-VOLF))*3.1416*ASYMPT)
```

```
C
```

```
C WRITE ADJUSTED SAXS VARIABLES
```

```
C
```

```
WRITE(6,120) TITLE
```

```
WRITE(6,125)
```

```
WRITE(6,130)(I,GUINT(I),BINT(I),ANGLE(I),ESSQ(I),CKAREA(I),CKASYM(  
11),SLOPE(I),I=1,NN)
```

```

C
C DETERMINE LOG NORMAL MU AND SIGMA FROM GUINIER AND POROD RADII USING
C MOMENT RELATIONSHIPS
C
      AVGR=EXP(ALOG(GUINR))-1.7143*ALOG(GUINR/POROD))
      SIGMA=EXP(SQRT(ALOG(GUINR/POROD))/3.5))
      HIGHR=SIGMA*AVGR
      SMALR=AVGR/SIGMA
      RADMAX=EXP(ALOG(AVGR)-(ALOG(SIGMA))**2)

      WRITE(6,135) CONST
135  FORMAT(1H0,26H THE GUINIER INTERCEPT IS,F10.3)

      WRITE(6,140)AREA,ASYMPT,POROD,GUINR,AVGR,SIGMA,HIGHR,SMALR,RADMAX
140  FORMAT(1H ,2X, 7HAREA IS,F 9.6/ 3X, 9HASYMPT IS,F10.7// 3X,15HPOR
      10D RADIUS IS,F 9.4,1X,9HANGSTROMS/ 3X,16HGUINER RADIUS IS,F 9.4,1
      2X,9HANGSTROMS/ 3X,14HMEAN RADIUS IS,F 8.4,1X,9HANGSTROMS/ 3X, 8H
      3SIGMA IS,F 8.5/ 3X,15HLARGE RADIUS IS,F 9.4,1X,9HANGSTROMS/ 3X,1
      45HSMALL RADIUS IS,F 8.4,1X,9HANGSTROMS/3X,34HTHE RADIUS OF MAXIMUM
      5 ABUNDANCE IS,F9.4,10H ANGSTROMS)

```

C



```

C
C DETERMINE DISTRIBUTION FUNCTION FOR TRIAL RADII BETWEEN 0 AND 50
C ANGSTROMS
      XRAD(1)=1.0
      DO 55 I=1,99
        A(I)=-0.5*(ALOG(XRAD(I))/ AVGR) /ALOG(SIGMA))**2
        B(I)=SQRT(6.2832)*XRAD(I) *ALOG(SIGMA)
        POPUL(I)=(EXP(A(I)))/B(I)*100
        XRAD(I+1)=XRAD(I)+1.0
      55 CONTINUE

C
      WRITE(6,120) TITLE
      WRITE(6,145)
145  FORMAT(1H0,16HRADIUS  PERCENT,6X,16HRADIUS  PERCENT,6X,16HRADIUS
1  PERCENT)
      WRITE(6,150)(XRAD(I),POPUL(I),XRAD(I+33),POPUL(I+33),XRAD(I+66),PO
1PUL(I+66),I=1,33)
150  FORMAT(1H ,F5.1,F9.3,F13.1,F9.3,F13.1,F10.3)
C

```

C

```

WRITE(6,160)
160 FORMAT(1H0, 5X,7HGUINIER,3X,5HPOROD,5X,2H $\mu$ ,5X,7HMAX RAD,3X,5HSIGM
1A,6X,11HSIGMA RANGE)
WRITE(6,165)GUINR,POROD,AVGR,RADMAX,SIGMA,SMALR,HIGH
1R
165 FORMAT(1H0,F11.2,F10.2,F9.2,F10.4,F8.2,3H TO,F7.2)
CALL PLOT2(GRAPH,100.0,0.0,20.0,0.0)
CALL PLOT3(1H*,XRAD(1),POPUL(1),99)
WRITE(6,9)
CALL FPLLOT4(22,22HFREQUENCY DISTRIBUTION)
C
WRITE(6,121)TITLE
C
C PROGRAM TO COMPUTE DEBYE CORRELATION VALUES FROM SAXS DATA AFTER
C E. L. GUNN, J. PHYS, CHEM. 62, 928 (1958)
C INTENSITY=(8*PI*DEBYE-CUBED*ELECTRON-DENSITY-SQ.*VOLUME)/
C (1+(2*PI*ANGLE(1)*DEBYE)-SQ.)-SQ.
C
C DEBYE IS EVALUATED FROM SLOPE AND INTERCEPT OF 1/SQRT(CPS) VS. ANGLE-

```

C SQUARED

TOTX=0

TOTY=0

TOTXSQ=0

TOTXY=0

DO 601=1,NN

X(1)=ANGLE(1)\*\*2

Y(1)=1./SQRT(BINT(1))

TOTX=TOTX+X(1)

TOTY=TOTY+Y(1)

TOTXSQ=TOTXSQ+X(1)\*\*2

TOTXY=TOTXY+X(1)\*Y(1)

60 CONTINUE

SLOAP=(NN\*TOTXY-TOTX\*TOTY)/(NN\*TOTXSQ-TOTX\*\*2)

ZERO =(TOTXSQ\*TOTY-TOTX\*TOTXY)/(NN\*TOTXSQ-TOTX\*\*2)

DEBYE=0.15915\*SQRT(SLOAP/ZERO )

SPHERE=1.165\*DEBYE

C

C FOR SPHERICAL PARTICLES, DEBYE AND BUECHE NOTE THAT AT GAMMA(R)=0.312,

```

C R IS THE CORRELATION RADIUS OF THE SPHERE.
C
C FOR RANDOM DISTRIBUTION OF INHOMOGENIETIES, THE CORRELATION FUNCTION,
C GAMMA=EXP(-R/DEBYE) WHERE R IS THE DISTANCE VARIABLE
C
      D(1)=0.0
      DO 70 I=1,99
        CORRL(I)=EXP(-D(I)/DEBYE)
        D(I+1)=D(I)+1.0
      70 CONTINUE
C
      WRITE(6,120) TITLE
      WRITE(6,170)
170 FORMAT(1H0,25HTRIAL DIAM. CORRELATION,4X,25HTRIAL DIAM. CORREL
      IATION,4X,25HTRIAL DIAM. CORRELATION)
      WRITE(6,175)(D(I),CORRL(I),D(I+33),CORRL(I+33),D(I+66),CORRL(I+66)
      1,I=1,33)
175 FORMAT(1H ,F8.1,F15.5,F13.1,F16.5,F12.1,F17.5)
      WRITE(6,180) SLOAP,ZERO ,DEBYE,SPHERE,AREA

```

```
180 FORMAT(1H0,13HTHE DEBYE SLOPE IS,F8.2,20H ANGSTROMS/SQRT(CPS))/23H
1THE DEBYE INTERCEPT IS,F8.5,14H PER SQRT(CPS))/47HTHE DEBYE INHOMO
2GENEITY CORRELATION DISTANCE IS,F8.4,10H ANGSTROMS//38HTHE DEBYE C
3ORRELATION SPHERE RADIUS IS,F8.4,10H ANGSTROMS//28HTHE INTEGRATED
4INTENSITY IS ,F10.8,13H ANGSTROMS SQ)

GO TO 4

C

100 STOP

END

//GO.SYSIN DD *
```

## BIBLIOGRAPHY

1. A. Guinier, Metaux. Corros. Usure, 18, 1943, 209.
2. C. Panseri and T. Federighi, Acta Met., 12, 1964, 272.
3. V. Gerold, Phys. Stat. Sol., 8, 1965, K5.
4. V. Gerold, Acta Met., 10, 1962, 637.
5. G. J. Carpenter and R. D. Garwood, Metal Sci. Jour., 1, 1967, 202.
6. J. T. Veitz, K. R. Sargant and I. J. Polmear, Jour. Inst. Metals, 92, 1963-64, 327.
7. I. J. Polmear, Jour. Inst. Metals, 86, 1957-58, 113.
8. I. J. Polmear, Nature, 186, 1960, 303.
9. I. J. Polmear and P. Scott-Young, Jour. Inst. Metals, 87, 1958-59, 65.
10. I. J. Polmear, Jour. Australian Inst. Metals, 17, 1972, 1.
11. I. J. Polmear, Jour. Inst. Metals, 87, 1958-59, 24.
12. H. Schmalzried and V. Gerold, Zeit. für Metallk., 49, 1958, 291.
13. V. Gerold and H. Haberkorn, Zeit. für Metallk., 50, 1959, 268.
14. G. W. Lorimer and R. B. Nicholson, Acta Met., 14, 1966, 1009.
15. Mondolfo, Gjosten and Levinson, Jour. of Metals, 206, 1956, 1378.
16. J. D. Embury and R. B. Nicholson, Acta Met., 13, 1965, 403.

17. Y. Tomita, K. Liu, Y. Murakami and M. Morinaga, Trans. Japan Inst. Metals, 15, 1974, 99.
18. R. Graf, Compt. Rend., 242, 1956, 1311.
19. K. Asano and K. Hirano, Trans. Japan Inst. Metals, 9, 1968, 24.
20. K. Hirano and K. Asano, Trans. Japan Inst. Metals, 11, 1970, 225.
21. K. Asano and K. Hirano, Trans. Japan Inst. Metals, 9, 1968, 149.
22. B. A. Parker, Jour. Australian Inst. Metals, 17, 1972, 31.
23. D. S. Thompson, B. S. Subrananya and S. A. Levy, Met. Trans., 2, 1971, 1149.
24. Y. Baba, Trans. Japan Inst. Metals, 11, 1970, 404.
25. K. Dünkeloh, G. Kralik and V. Gerold, Zeit. für Metallk., 65, 1974, 291.
26. S. Chang and J. E. Morral, Acta Met., 23, 1975, 685.
27. P. Bardhan and E. A. Starke, Jour. Mats. Sci., 3, 1968, 57.
28. N. Ryum, Zeit. für Metallk., 66, 1975, 338.
29. P. A. Thackery, Jour. Inst. Metals, 96, 1968, 228.
30. N. Ryum, Zeit. für Metallk., 66, 1975, 344.
31. N. Ryum, Zeit. für Metallk., 66, 1975, 377.
32. H. Bossac and H. Löffler, Phys. Stat. Sol., 27, 1975, K125.
33. A. J. Perry, Acta Met., 14, 1966, 1.
34. C. Panseri and T. Federighi, Acta Met., 11, 1963, 575.

35. T. Federighi, Jour. de Phys. Radium, 23, 1962, 795.
36. S. Ceresara and A. Giarda, Phil. Mag., 296, 1974, 1245.
37. S. Ceresara and P. Fiorini, Mater. Sci. Eng., 10, 1972, 205.
38. L. E. Katz, K. Rao and H. Herman, Trans. Indian Inst. Metals, 19, 1966, 95.
39. G. Jurgens, M. Kempe and H. Loffler, Phys. Stat. Sol., 25, 1974, K73.
40. R. W. Gould and V. Gerold, Acta Met., 12, 1964, 954.
41. A. J. Perry, Jour. Phys. Soc. Japan, 21, 1966, 549.
42. K. Hirano and Y. Takagi, Jour. Phys. Soc. Japan, 10, 3, 1955, 187.
43. K. Hirano, Jour. Phys. Soc. Japan, 10, 1955, 23.
44. J. T. Staley, R. H. Brown and R. Schmit, Met. Trans., 3, 1972, 191.
45. M. Conserva, E. DiRusso and O. Caloni, Met. Trans., 2, 1971, 1227.
46. A. J. Bryant, Jour. Inst. Metals, 94, 1966, 94.
47. L. F. Mondolfo, Met. Reviews, 153, 95.
48. S. D. Harkness and R. W. Gould, Advances in X-Ray Analysis, 12, 1969.
49. S. D. Harkness, R. W. Gould and J. J. Hren, Phil. Mag., 19, 1969, 113.
50. R. W. Gould, Jour. Inst. Metals, 99, 1971, 1.
51. C. A. Grove and G. Judd, Tech. Report No. 4, O.N.R., 1972.
52. G. Judd and C. R. Shastry, Tech. Report No. 1, O.N.R., 1970.



53. C. R. Shastry and G. Judd, Tech. Report No. 3, O.N.R., 1972.
54. A. Guinier, X-Ray Diffraction, San Francisco: W. H. Freeman and Co., 1963.
55. A. Guinier and G. Fornet, Small-Angle Scattering of X-Rays, New York: John Wiley and Sons, Inc., 1955.
56. A. Guinier, Advances in Solid State Physics, 9, 1960, 293.
57. V. Gerold. Small Angle X-Ray Scattering, chapt. H. Baumberger, ed., New York: Gordon and Breach, 1965.
58. R. Baur and V. Gerold, Acta Met., 10, 1962, 637.
59. R. Baru and V. Gerold, Acta Met., 12, 1964, 1448.
60. W. Merz and V. Gerold, Zeit für Metallk., 57, 1966, 607.
61. G. Thomas and J. Nutting, Jour. Inst. Metals, 88, 1959-60, 81.
62. A. T. Little, W. Hume-Rothery and G. V. Raynor, Jour. Inst. Metals, 70, 1944, 491.
63. O. Kratky, G. Porod and L. Kalovec, Zeit. für Elektrochemie, 55, 1951, 53.
64. R. Perret and W. Rulano, Jour. Appl. Crystal., 5, 1972, 116.
65. R. W. Gould and P. W. Kirklin, Computer Program, University of Florida.
66. J. T. Healey and M. S. Hill, Modification of Gould-Kirklin Computer Program, University of Florida.
67. R. E. Hummel, personal communication.
68. G. Böhm and V. Gerold, Scripta Met., 14, 1970, 269.
69. P. R. Cetlin, A. S. Gulec and R. E. Reed-Hill, Met. Trans., 4, 1973, 513.

- 70. N. F. Mott and F. R. Nabarro, Proc. Phys. Soc., 52, 1940, 86.
- 71. S. D. Harkness and J. J. Hren, Met. Trans., 1, 1970, 43.
- 72. P. B. Hirsch and A. Kelly, Phil. Mag., 12, 1965, 881.
- 73. E. DiRusso, M. Conserva, F. Gatto and H. Markus, Met. Trans., 4, 1973, 1133.
- 74. F. G. Ostermann and W. H. Reimann, A.S.T.M. STP 467, 1970, 169.

## ADDITIONAL REFERENCES

- G. W. Lorimer, Fizika, 2, suppl. 2, 1970.
- K. Osamuar, Y. Kirsoka and Y. Murakami, Phil. Mag., 28, 4, 1973, 809.
- J. G. Morris, Mater. Sci. Eng., 9, 1972, 361.
- E. DiRusso, M. Conserva, M. Buratti and F. Gatto, Mater. Sci. Eng., 14, 1974, 23.
- T. Federighi and G. Thomas, Phil. Mag., 7, 1962, 127.
- Y. Tomita, K. Liu, Y. Murakami and M. Morinaga, Trans. Japan Inst. of Metals, 15, 1974, 98.
- M. Koiwa, Phil. Mag., 30, 1974, 877.
- A. Buch, Zeit. fur Werk., 5, 1974, 194.
- P. Doig and J. W. Edington, Phil. Mag., 29, 1, 1974, 217.
- M. E. Fine, Met. Trans., 6A, 1975, 625.
- M. Morinaga, K. Liu, Y. Tomita and Y. Murakami, Trans. Japan Inst. of Metals, 15, 1974, 62.
- M. Morinaga, M. Murakami, O. Kawano and Y. Murakami, Phil. Mag., 24, 1971, 527.
- P. K. Poulouse, J. E. Morral and A. J. McEvily, Met. Trans., 5, 1974, 1393.
- M. Murakami, O. Kawano and Y. Murakami, Trans. A.I.M.E., 245, 1969, 815.
- M. Ohta and F. Hashimoto, Jour. Phys. Soc. Japan, 19, 1964, 130.
- M. Bernole and R. Graf, Mem. Sci. Rev. Met., 69, 1972, 123.

K. J. Nes and N. Ryum, Acta Met., 23, 1975, 979.

A. Guinier, Physics Today, 22, 11, 25.

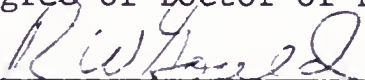
F. Ostermann, Met. Trans., 2, 1971, 2987.

## BIOGRAPHICAL SKETCH

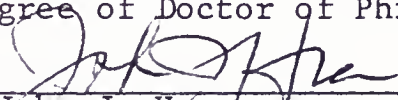
John Thomas Healey was born on March 9, 1950, in Hasbrouck Heights, New Jersey. He attended Hasbrouck Heights High School, and graduated in June, 1968. He attended Newark College of Engineering, now New Jersey Institute of Technology, from 1968 to 1972 and received the degree of Bachelor of Science in Engineering Science. In 1972, he moved to Gainesville, Florida, and has been pursuing the degree of Doctor of Philosophy at the University of Florida, since that time. He has been employed during this period as a research assistant in the Department of Materials Science and Engineering.

John Thomas Healey is a member of Tau Kappa Epsilon, Tau Beta Pi and Alpha Sigma Mu.

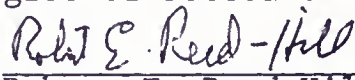
I certify that I have read this study and that in my opinion it conforms to acceptable standards of scholarly presentation and is fully adequate, in scope and quality, as a dissertation for the degree of Doctor of Philosophy.

  
Robert W. Gould, Chairman  
Professor of Materials Science

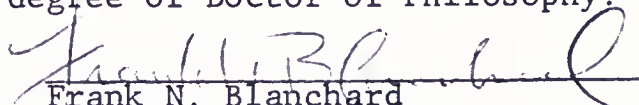
I certify that I have read this study and that in my opinion it conforms to acceptable standards of scholarly presentation and is fully adequate, in scope and quality, as a dissertation for the degree of Doctor of Philosophy.

  
John J. Hren  
Professor of Materials Science

I certify that I have read this study and that in my opinion it conforms to acceptable standards of scholarly presentation and is fully adequate, in scope and quality, as a dissertation for the degree of Doctor of Philosophy.

  
Robert E. Reed-Hill  
Professor of Materials Science

I certify that I have read this study and that in my opinion it conforms to acceptable standards of scholarly presentation and is fully adequate, in scope and quality, as a dissertation for the degree of Doctor of Philosophy.

  
Frank N. Blanchard  
Associate Professor of Geology

This dissertation was submitted to the Graduate Faculty of the College of Engineering and to the Graduate Council, and was accepted as partial fulfillment of the requirements for the degree of Doctor of Philosophy.

Wayne H. Chen  
Dean, College of Engineering

Dean, Graduate School

4599 See main 38 (114)

RU 2. 76 6.17.1.